

A Theoretical Study on the Surfaces of Zinc Oxide

David Perfecto Mora Fonz

A dissertation submitted in partial fulfillment
of the requirements for the degree of
Doctor of Philosophy
of
University College London.

Department of Chemistry
University College London

May 2016

I, David Perfecto Mora Fonz, confirm that the work presented in this thesis is my own. Where information has been derived from other sources, I confirm that this has been indicated in the work.

Abstract

Zinc oxide is an important wide bandgap *n*-type semiconductor with uses ranging from electronics to catalysis. The chemical and physical properties related to its surfaces are of fundamental interest and also key to the material's design.

In this Thesis, computational methods have been used to model the surfaces of ZnO. We report a detailed theoretical study on the four main low-index wurtzite ZnO surfaces. For nonpolar surfaces, we focus on the stability, atomic structure and electronic properties of both clean and defective surfaces. Our calculations explain why steps are common on the $(10\bar{1}0)$ surface, as seen in experiment. We calculate the ionisation potential which is in good agreement with experiment. The electronic band edges of the nonpolar surfaces are seen to behave differently, with a local rise of the VBM and CBM for $(10\bar{1}0)$ and $(11\bar{2}0)$, respectively.

For ZnO polar surfaces, our results can explain why experimental findings reported have been varied and even contradictory at times. The calculated surface energies indicate on average a slightly higher stability of the $(000\bar{1})$ surface compared to the (0001) surface. Structurally, triangular and hexagonal patterns are seen among the stable structures but a high level of disorder is predicted.

We also report new interatomic potentials (IP) for the Cu/ZnO system. Our IP can work as a fast and reliable method to filter low energy Cu/ZnO structures. Global optimisation calculations show a preference for planar Cu clusters over the $(10\bar{1}0)$ surface, with a strong interaction between the Cu and Zn species.

Finally, we study the surface atomic configurations for the $\text{MoO}_3/\text{Fe}_2\text{O}_3$ catalytic system. The lowest energy structure was used in the fitting of EXAFS parameters. Overall, our Thesis shows the great utility of theoretical calculations in the explanation of experimental findings in surface science.

Acknowledgements

Here, there are some words for the people that have supported me throughout this four-year journey, making it easier, special and unforgettable.

First and foremost, I would like to thank my supervisor Richard Catlow for giving me the opportunity of being part of his amazing research team. His guidance, inspiration and support have played a vital role in this stage of my scientific career.

I would also thank Alexey Sokol and Scott Woodley. Alexey, my deepest gratitude for sharing your knowledge and for all those hours discussing with me the theoretical insights of zinc oxide. Scott, thanks for your support and modifications to KLMC.

I would like to acknowledge David Scanlon for sharing his VASP skills; Matt Farrow and Tomas Lazauskas for fixing all my software issues. Thanks also to John Buckeridge, Stephen Shevlin and my colleagues at 349 and 351 KLB offices, in special to Alex and Dougal for proofreading this dissertation.

This journey would have been impossible without my family: Mamá, Papá, Miguel, Lupita and Arturo. You have always been there for me, you are my strength and you follow me everywhere I go. I love you all.

Special thanks to Jorina for her love, patience and faithful support. She has been key during the realisation of this Thesis. I also thank my dear friends in London, who made my time more enjoyable. Thanks also to all my friends in Mexico who recharge my batteries every Christmas holiday.

Finally, thanks to all the institutions that supported me during my PhD: Consejo Nacional de Ciencia y Tecnología (CONACYT), Secretaría de Educación Pública (SEP), Universidad Juárez Autónoma de Tabasco (UJAT) and University College London (UCL).

Contents

1	Introduction	20
1.1	Objectives	21
1.2	General Aspects of Zinc Oxide	22
1.3	Thesis Outline	23
2	Theoretical Methods	25
2.1	Introduction	25
2.2	Crystalline Materials	26
2.2.1	Periodic Boundary Conditions	27
2.2.2	Reciprocal Space	28
2.3	Interatomic Potential Methods	29
2.3.1	Introduction	29
2.3.2	The Calculation of the Energy	29
2.3.3	Two-Body Potentials	30
2.3.4	Shell Model	32
2.3.5	Many-body Potentials	32
2.3.6	Fitting Potentials	34
2.4	Quantum-Mechanical Methods	34
2.4.1	Introduction	34
2.4.2	Hartree-Fock Method	35
2.4.3	Density Functional Theory	37
2.5	Surface Calculations	42
2.6	Implementation	45

2.6.1	General Utility Lattice Program (GULP)	45
2.6.2	Vienna Ab-initio Simulation Package (VASP)	46
2.6.3	Knowledge Led Master Code (KLMC)	46
2.7	High Performance Computing (HPC)	47
3	Bulk and Non-polar Surfaces of ZnO	48
3.1	Introduction	48
3.2	Calculation Settings	49
3.2.1	ZnO Bulk (DFT-based)	49
3.2.2	Surface Models of ZnO (DFT-based)	50
3.3	ZnO Bulk	50
3.4	Non-polar Surfaces of ZnO	53
3.4.1	Crystal Growth	53
3.4.2	Surface Structure	54
3.4.3	Stability of the Clean Non-polar Surfaces of ZnO	58
3.4.4	Steps and Vacancies at the (10 $\bar{1}$ 0) ZnO Surface	61
3.5	Electronic Properties of Non-polar Surfaces	70
3.5.1	Ionisation Potential and Band Alignment	71
3.6	Summary and Conclusions	78
4	Polar Surfaces of ZnO	80
4.1	Introduction	80
4.2	Stabilisation Mechanisms of Polar Surfaces of ZnO	82
4.2.1	Surface “Metallization”	83
4.2.2	Adsorption of Adatoms.	83
4.2.3	Vacancies.	84
4.2.4	Faceting	85
4.3	Methods and Computational Details	86
4.3.1	Strategy	86
4.3.2	Polar ZnO Surface Models	88
4.3.3	Surface Energy Calculation	91

4.4	The Dipole Effect on the Atomic Structure of ZnO Polar Surfaces . . .	92
4.5	Surface Energies	93
4.6	Atomic Structure	94
4.7	Summary and Conclusions	102
5	The Cu/ZnO System	104
5.1	Introduction	104
5.1.1	Small Cu Clusters	105
5.1.2	Cu Growth on Nonpolar Surfaces of ZnO	106
5.2	Methodology	107
5.3	Fitting of Interatomic Potentials	112
5.4	Further Optimisation	116
5.5	Global Optimisation	118
5.6	Summary and Conclusion	124
5.7	Future Work	125
6	The MoO₃/Fe₂O₃ System	126
6.1	Introduction	126
6.2	Methods and Computational Details	127
6.2.1	Bulk Fe ₂ O ₃	127
6.2.2	Surface Models	128
6.2.3	MoO ₃ Adsorption	129
6.3	Fe ₂ O ₃ Bulk	131
6.4	Surface Structure	132
6.5	MoO ₃ Adsorption	133
6.6	Further Refinement	136
6.7	Summary and Conclusions	139
7	Summary and Conclusions	141
	Bibliography	147

List of Figures

1.1	Wurtzite and zinblende structures of zinc oxide. Red and grey circles represent oxygen and zinc.	23
2.1	Periodic boundary conditions in two dimensions. A unit cell is shown on the left-hand side of the picture. The periodic images on the right (presented with lighter colours) were generated by PBC. The arrows over the circles represent displacements of the atoms.	27
2.2	Typical shape of a two-body potential as a function of the inter-atomic distances r_{ij} . The subfigure at the top is a representation of the shell model interactions. The indices “C” and “S” are used to represent the cores and shells, respectively. The charged points, core and shell, experience Coulombic forces. The short-range interactions only act on the shell of an ion. The spring potential models the core-shell interactions.	33
2.3	Simplified algorithmic flowchart illustrating the SCF method.	36
2.4	Representation of (a) the periodic slab model and (b) the two region model	44
2.5	The three types of Tasker’s surfaces. (a) Type 1, same number of anions and cations on each plane, nonpolar surface. (b) Type 2, charged planes but no net dipole moment normal to the surface. (c) Type 3, alternating layers of cations and anions which lead to charged planes and a dipole moment perpendicular to surface	45

- 3.1 ZnO wurtzite structure. The lattice vectors: a and c , and the internal parameter u are shown. The ions in darker colours represent the primitive unit cell, which is shown on the right-hand side. Red is reserved for O and grey for Zn. 51
- 3.2 Schematic representation of the relaxed and unrelaxed $(10\bar{1}0)$ ZnO surface. Black lines show the bulk position structure. The stick representation is the relaxed $(10\bar{1}0)$ structure. Only atoms in the first double layer were represented on the top view; darker colours, in (b), were used to represent ions in the first layer. Layers 1, 2, 3 and 4 are represented as L1, L2, L3 and L4, respectively. 57
- 3.3 Schematic representation of the relaxed and unrelaxed $(11\bar{2}0)$ ZnO surface. Black lines show the bulk position structure. The ball-and-stick representation is the relaxed $(11\bar{2}0)$ structure. Darker colours were used to represent ions in the first topmost layer. Δ values represent the distance between the selected ions along the specified direction. 60
- 3.4 Top view of the lowest five (1-5) and highest (z) energy $(10\bar{1}0)$ ZnO structures with 75% first layer occupancy. Energy cost per vacancy is represented below each structure. Red, grey and blue balls represent oxygen, zinc and vacancies, respectively. Darker balls are first layer atoms. The black box represents the 4×4 supercell. 67

- 3.5 Schematic representation of the relaxed and unrelaxed $(10\bar{1}0)$ ZnO surface showing a step along the (a,b) $[010]$ direction and along the (c,d) $[010]$ direction. (a) Side view along the $[001]$ direction of the $(10\bar{1}0)$ ZnO surface, (b) top view along the hexagonal axis of the $(10\bar{1}0)$ ZnO surface, (c) side view along the $[010]$ direction of the $(10\bar{1}0)$ ZnO surface and (d) top view along the hexagonal axis of the $(10\bar{1}0)$ ZnO surface. Black lines show the bulk position structure. Ball and stick representation is the relaxed structure. Only atoms that are in the green region were shown in the top view; darker colours, in (b) and (d), were used to represent uppermost ions. 68
- 3.6 Energy of step formation on the $(10\bar{1}0)$ ZnO surface, where n is the size of the supercell along the $[010]$ or $[001]$ direction. The dashed line is a linear fit for the step along the $[010]$ direction. 69
- 3.7 ZnO band alignment based on the ionisation potential. The horizontal lines represent the experimental reported values: 7.82 eV for I^b [1] and 3.44 eV for the bulk band gap [2, 3]; for the $(10\bar{1}0)$ and $(11\bar{2}0)$ a I^s value of 8.00 eV [4, 5] and 7.82 eV [1], respectively. “(D)” [6] has the same meaning as in Table 3.6. The positioning of the CBM bands for the relaxed $(10\bar{1}0)$ and $(11\bar{2}0)$ surfaces was made by adding the band gap calculated for each relaxed surface presented on Table 3.6 to the VBM value. 75
- 3.8 ZnO band bending of the CBM and VBM. Bulk values for CBM and VBM were taken from experiment. E_{vac} , $-eV_{CBM}$, $-eV_{VBM}$, E_F , χ and Φ represent the vacuum, band bending at the CBM, band bending at the VBM, the Fermi level, the electron affinity and the work function, respectively. Each diamond/square represents a layer. Values were taken from Figure 3.9. 76

- 3.9 (a) Representation of the total density of states for wurtzite ZnO structure using PBEsol0 functional, for comparison see Figure 2 in Ref. 7. Surface band bending across the ZnO surfaces: (b,c) (10 $\bar{1}$ 0) and (d,e) (11 $\bar{2}$ 0). Surface structures from (b,d) PBE0 and (c,e) PBEsol0 functionals were taken to produce the surface band bending. Layer 1 and 8 are labelled as “Surface” and “Bulk” layers, respectively. The vertical red line represents the top of the valance band. The VB and CB were amplified by a factor of 3 and 25 to make the changes more visible. 77
- 4.1 ZnO polar surface. The internal parameter u and the fractional distance k are shown. Red colour is reserved for O and grey for Zn. 87
- 4.2 Lowest dipole possible using entire ionic transfer from a range of 1 to 400 supercell size. Inset: only points that reduce the dipole while increasing the cell size shown. 89
- 4.3 ZnO polar surface. A dipole-corrected one-sided model of the Zn-terminated polar surface of ZnO. A two-region setup is used in our calculations with region one, R1, allowed to relax, and region two, R2, held fixed. The residual surface dipole is compensated by the opposite and equal in magnitude dipole due to two planes of point charges: placed outside of the surface slab at a large distance. In this paper, red colour is reserved for O and grey for Zn. 90
- 4.4 Energetic rankings for five optimised structures using both with and without compensating point charges. Twelve different stoichiometries were tested between the two ZnO polar surfaces. Data points on the blue line represent atomic structures that did not change energetic rankings. Data points out of the blue line show structures that changed energetic rankings, meaning a difference between *weak dipole* and *dipole = 0* approaches (more description of these methods is given in Section 4.4). 93

- 4.5 Surface energies of the polar surfaces as a function of the stoichiometry. For each data point the relation $|m_{Zn} - m_O|/25 \approx 0.24$ was conserved. 94
- 4.6 Lowest energy structures for the zinc terminated surface. Numbers in each sub-figure represent the number of zincs at the top surface (m_{Zn}); for each stoichiometry there are 6 oxygens more than zincs. The grey colour is reserved for the second layer atoms, dark grey and light grey represent oxygen and zinc, respectively. Red and blue were used for top oxygen and zinc atoms, respectively. 98
- 4.7 Lowest energy structures for the oxygen terminated surface. Numbers in each sub-figure represent the number of oxygens at the top surface (m_O), for each stoichiometry there are 6 zincs more than oxygens. The grey colour is reserved for the second layer atoms, dark grey and light grey represent oxygen and zinc, respectively. Red and blue were used for top oxygen and zinc atoms, respectively. 99
- 4.8 Number of significant unique surface reconstructions as a function of the stoichiometry for different temperatures. The horizontal grey lines represent 1,2,3,4 and 5 unique structures, respectively. The nomenclature of the stoichiometries are used as in Figures 4.5, 4.6 and 4.7 101
- 4.9 GM and second lowest energy structures for selected stoichiometries. Nomenclature represents the surface termination and the stoichiometry. 101
- 5.1 Global minima Cu_n clusters ($3 \leq n \leq 8$) as calculated with the Gupta interatomic potentials [8]. 106
- 5.2 Top and side views of the Cu_4 -ZnO structural model employed in fitting parameters of interatomic potentials to DFT data. The $(10\bar{1}0)$ (black) and the $(11\bar{2}0)$ (blue) (2×2) supercell are shown. In the side views, different blue shades were used to represent the heights of the SP calculations. Blue circles are reserved for copper atoms. . 110

- 5.3 Top and side views of the $\text{Cu}_8\text{-ZnO}$ structural model employed in fitting parameters of interatomic potentials to DFT data. The $(10\bar{1}0)$, in black, the $(11\bar{2}0)$, in blue, (4×4) supercell and the GM Cu_8 cluster are shown. In the side views, different blue shades were used to represent the heights of the SP calculations. Blue circles represent copper atoms. 111
- 5.4 Graphical representation of the global optimisation process used within KLMC. (a) Shows the 5 *double-layer* (4×3) ZnO surface with 3 atomic layers of a (4×4) supercell of the (110) Cu surface on top of it. This picture shows 41 Cu lattice positions from which 8 will be occupied. (b) A structure example created by KLMC after the swapping process with 8 Cu occupied lattice positions. 112
- 5.5 Potential fitting curves. Blue and green lines show the adsorption energy observables using DFT and IP, respectively. From 5 Å to 9 Å all the curves remain flat to the naked eye. 115
- 5.6 Top and side views of the initial and optimised Cu_8/ZnO structures. The black lines represent the (4×4) supercell. All ions were allowed to relax in the figures at the center, whereas in the figures on the right the ZnO atoms were held fixed. 117
- 5.7 Top and side views of two different initial Cu_8/ZnO structures. The black lines represent the (4×3) supercell. Both structures optimised in the same final structure shown at the bottom of the Figure. 117
- 5.8 Top and side views of the five lowest energy structures from global optimisation. On the left, the structures predicted by our new Cu/ZnO set of potentials. On the right, the structures refined by DFT. Energies are with respect to the lowest energy structure on the respective energy landscapes. The (4×3) supercell is shown in the first structure. 122

- 5.9 Top and side views of the global minima found of Cu_n clusters ($1 \leq n \leq 8$) deposited on the (4×3) $(10\bar{1}0)$ surface from global optimisation. The formation energy (using Cu_{metal} as a source of Cu) per Cu atom is displayed. 123
- 6.1 Hexagonal unit and primitive cells of $\alpha\text{-Fe}_2\text{O}_3$. Both lattice parameters and interplane distances Fe-Fe(A) and Fe-Fe(B) are shown. The anti-ferromagnetic arrangement is indicated with green arrows. Red and brown spheres represent oxygen and iron ions, respectively. 129
- 6.2 Top and side view of the $\alpha\text{-Fe}_2\text{O}_3(0001)$ surface. Different initial adsorption sites (from A to E) for the MoO_3 molecule are shown; the rhomboids represent the surface unit cell. The drawn plane marks the position of the semi-transparent oxygen ions showed in the left picture. 130
- 6.3 Relaxed structures for the different adsorption sites. Energies based on (1×1) surface calculations. The relaxed structure for the adsorption site D is not shown since it adopts either structure A or B. Red, brown, and violet spheres denote oxygen, iron, and molybdenum, respectively. The rhombohedron represents the surface unit cell. Energies are in kJ/mol. 135
- 6.4 Side view of the polyhedral representation of the lowest energy MoO_3 adsorbed on a thirteen- Fe_2O_3 -(0001)-layer surface. 135
- 6.5 Side and top views of the two lowest energy $\text{MoO}_3/\text{Fe}_2\text{O}_3$ structures. Structures before and after hydroxylation are shown. White spheres represent hydrogen. The rhombohedron represents the surface unit cell. 137
- 6.6 Side and top views of the two modifications to the lowest energy site A structure: (i) an extra MoO_3 on top of the Fe(2b) (see Figure 6.2) and (ii) exchange Mo and topmost Fe positions. The rhombohedron represents the surface unit cell. 139

List of Tables

3.1	Bulk Properties of the Wurtzite Structure of Zinc Oxide	52
3.2	Formation and Cohesive Energies.	53
3.3	Atomic Relaxations of the First Two Layers of the Non-Polar (10 $\bar{1}$ 0) Surface.	56
3.4	Atomic Relaxations of the First Two Layers of the Non-Polar (11 $\bar{2}$ 0) Surface.	59
3.5	Surface Energy, E_{surf} (J/m^2), of the Non-Polar ZnO Surfaces with the Different Functionals and in Comparison with Previous Calcula- tions.	62
3.6	ZnO Ionisation Potential. Where I is the Ionisation Potential, “b” Refers to the Bulk, “s” to the Surface and “D” to the New Method Used (Taking into Account Surface Polarisation Effects) [6]. Ener- gies are in eV.	75
4.1	Atomic Relaxations of the First Two Layers Along the c Axis of the Polar (0001) and (000 $\bar{1}$) Surfaces. All Relaxations are given in Å. .	100
5.1	Parameters of the Interatomic Potentials Used for Zinc Oxide. . . .	109
5.2	Parameters of the Interatomic Potentials Used for Copper.	110
5.3	Interatomic Potentials Parameters for the Cu-ZnO System. A Ra- dial Cut-off of 12 Å was Used for All Potentials. The Forms of the Potentials Described Below Are: $E(\text{Buckingham}) =$ $A \exp(-R/\rho) - C/R^6$, $E(\text{Morse}) = D_e((1 - \exp(-a(R - r_0)))^2 -$ 1), Where R Represents the Distance Between the Ions in Question. .	111

6.1	Experimental and Theoretical Structural Parameters for the Hematite Bulk Structure. Distances Are Given in Å.	131
6.2	Relative Interlayer Distances on α -Fe ₂ O ₃ (0001) Surface. All the Values Below Are Given as a Percentage with Respect to Bulk Interlayer Fe-O (0.568 Å) and Fe-Fe (0.858 Å) Distances Along the <i>c</i> Axis. For the Nomenclature Used, See Figure 6.1.	133
6.3	Mo-O, Mo-Fe Distances (Å) and Adsorption Energies of the Relaxed MoO ₃ /Fe ₂ O ₃ Structures. The Coordination Number is Shown in Parenthesis. DFT + <i>U</i> and EXAFS Experimental Data Are Displayed.	134
6.4	Mo-O, Mo-Fe Distances (Å) of the Relaxed Hydroxylated MoO ₃ /Fe ₂ O ₃ Structures. Coordination Number Is Shown in Parenthesis. For Comparison with Experiments See Table 6.3.	137
6.5	Mo-O, Mo-Fe Distances (Å) of the Relaxed MoO ₃ /Fe ₂ O ₃ and 2MoO ₃ /Fe ₂ O ₃ Structures. Coordination Number Is Shown in Parenthesis. For Comparison with Experiments See Table 6.3. . . .	138

Acronyms and Abbreviations

ARPES	Angle-resolved photoemission spectroscopy
B3LYP	Becke, three-parameter, Lee-Yang-Parr
BFGS	Broyden-Fletcher-Goldfarb-Shanno
BO	Born-Oppenheimer
CBM	Conduction band minimum
DFT	Density Functional Theory
DOS	Density of states
EAM	Embedded atom model
EXAFS	Extended X-ray absorption fine structure
GA	Genetic algorithm
GGA	Generalized gradient approximation
GIXD	Grazing incidence X-ray diffraction
GM	Global minimum
GULP	General Utility Lattice Package
HAS	Helium atom scattering

HF	Hartree-Fock
HPC	High Performance Computing
HRTEM	High-resolution transmission electron microscopy
IP	Interatomic potentials
KLMC	Knowledge Led Master Controller
LDA	Local-density approximation
LED	Light-emitting diode
LEED	Low-energy electron diffraction
LEIS	Low-energy ion scattering
LJ	Lennard-Jones
MC	Monte Carlo
ML	Monolayer
MM	Molecular mechanics
PAW	Projector augmented wave
PBC	Periodic boundary conditions
PBE	Perdew-Burke-Ernzerhof
QM	Quantum mechanics
QM/MM	Quantum and molecular mechanics
RT	Room temperature
SCF	Self-consistent field
STM	Scanning tunnelling microscope

TB	Tight-binding
TCO	Transparent conducting oxide
UHV	Ultra-high vacuum
UPS	Ultraviolet photoelectron spectroscopy
VASP	Vienna Ab-initio Simulation Package
VBM	Valence band maximum
XANES	X-ray absorption near edge structure
XC	Exchange-correlation
XPS	X-ray photoelectron spectroscopy

Chapter 1

Introduction

Since affordable fossil fuels and mineral resources are on the decline and stricter air pollution laws are being enforced, researchers have focused their efforts on searching for alternative ways to produce energy. One of the main alternatives is the use of hydrogen as a fuel. However, many transportation and storage problems still remain unsolved. Rather than as a fuel, another approach is to use hydrogen as an energy carrier, which is reacted with CO_2 to form methanol [9–11]. This process, however, requires a catalyst to reduce its activation energy. To date, the most widely used catalyst is Cu supported on $\text{ZnO}:\text{Al}_2\text{O}_3$, where the properties of the metal oxide surface play a crucial role. Yet the behaviour of ZnO surfaces and their interaction with Cu particles are still under discussion in the scientific community. Methanol is of great interest to the chemical industry, with an estimated production of 65 million tonnes per year in 2013 [12]. Consequently, there is a clear industrial need for improving and understanding the methanol synthesis process. If this can be done cheaply, it will have a major impact on industrial processes and on the science of clean energy fuels.

The understanding of metal oxide surfaces is of primary technological and scientific importance. In the last forty years, the interest in metal oxide surfaces has increased dramatically. They play a vital role in fields such as catalysis, passivation of metal surfaces, and gas sensing for pollution monitoring and control. Electronically, these systems cover the entire range in materials design from metallic to insulator behaviours [13]. In this respect, zinc oxide, an important metal oxide,

has been shown to have particularly interesting physical and chemical properties. This metal oxide belongs to the II-VI semiconductor group with a wide-bandgap n -type nature. Its uses and applications range from electronics to catalysis [14–17]. As mentioned earlier, ZnO is one of the main components in the catalyst used for methanol synthesis, and it is at its surfaces where Cu atoms are present (creating the active sites). Moreover, ZnO films with nonpolar faces have shown high emission efficiency for blue or ultraviolet LEDs [18–21]. Hence, the chemical and physical properties related to the surface structures of ZnO are of fundamental interest and are also key in the material's design. We therefore report an extensive study on the four main low-index surfaces of ZnO: $(10\bar{1}0)$, $(11\bar{2}0)$, (0001) and $(000\bar{1})$. We studied the atomic structure, stability and electronic properties of the clean surfaces, as well as both morphological features (at the nonpolar surfaces) and atomic reconstructions (at the polar surfaces). We also report new Cu/ZnO interatomic potentials, which were created to study the Cu growth on ZnO surfaces. Our analysis leads to a clear and coherent understanding of the behaviour of the four key surfaces of this widely used commercial material.

1.1 Objectives

There are two main goals in the study of a material's surface: the first is to determine where the atoms are found and the second is to analyse the electronic properties of these atomic structures. In this Thesis, the focus is on the study of metal oxide surfaces, with the main emphasis on zinc oxide, although one section is dedicated to iron oxide, which is discussed in Chapter 6. Throughout this work, exclusively theoretical methods based on interatomic potential and *ab initio* approaches are presented and discussed. These methods are widely used in the study of metal oxides and have been shown to be excellent tools in the characterisation of such materials.

The main aim of this work is to explain experimental findings in relation to zinc oxide and iron oxide surfaces, considering both structural and electronic properties. More specifically, the objectives are: (i) to study the atomic and electronic proper-

ties of ZnO bulk and its main low-index nonpolar $(10\bar{1}0)$ and $(11\bar{2}0)$ surfaces; (ii) to explain the nature of the highly stepped ZnO nonpolar surfaces; (iii) to explain the stability of the polar (0001) and $(000\bar{1})$ ZnO surfaces and link the presented results with experimental findings; (iv) to fit Cu/ZnO interatomic potentials to DFT calculations (which will be used in future work in the study of Cu/ZnO system); and (v) to help with the fit of experimental EXAFS data of $\text{MoO}_3/\text{Fe}_2\text{O}_3$ catalyst using DFT calculations.

1.2 General Aspects of Zinc Oxide

In this section, we list a number of general aspects of ZnO, which will serve as a brief introduction to the material's characteristics. Zinc oxide is an oxide compound which crystallizes into two main structures: hexagonal wurtzite and cubic zincblende, with the former universally observed over a wide range of temperature and pressure, including ambient conditions. Our study will therefore focus on the wurtzite structure. This structure has all its atoms in a tetrahedral coordination (Figure 1.1), i.e. every atom in the structure has four nearest neighbours of the opposite type positioned like the vertices of a tetrahedron. It is considered an AA' stack of one atom thick planes [22], forming hexagonal patterns. Its space group is $P6_3mc$ in Hermann-Mauguin notation, or No. 186 in the International Union of Crystallography classification. The wurtzite structure can be viewed as a "hexagonal lattice" with four atoms in the unit cell. The lattice constants are $a = b = 3.2417 \text{ \AA}$, and $c = 5.1876 \text{ \AA}$. The relative distance (along the c axis) between a pair of Zn and O atoms is controlled by the internal parameter $u = 0.3819$.¹ The atomic structure of the wurtzite phase has no inversion symmetry, which is the main reasons for its piezoelectric and pyroelectric properties. The wurtzite structure has four principal low-index surfaces, two side faces nonpolar, $(10\bar{1}0)$ and $(11\bar{2}0)$ and two opposite polar, (0001) -Zn and $(000\bar{1})$ -O. The two nonpolar surfaces are composed of equal numbers of cations and anions in each layer, whereas the polar surfaces have atomic monolayers of cations and anions distributed along the c -axis.

¹Experimental data are taken from the literature for the lowest available temperature: wurtzite structure from neutron crystal diffractometry at 20 K [23].

The zincblende structure also has a tetrahedral coordination and shares diamond's cubic structure, but with alternating zinc and oxygen atoms along the three different axes (Figure 1.1). The space group for this structure is $F\bar{4}3m$ (Hermann-Mauguin notation), or No. 216 (International Union of Crystallography classification).

Electronically, zinc oxide is an ionic *n*-type semiconductor with a band gap of 3.37 eV at room temperature. It has a wide range of applications including ceramics, catalysis, electronics, pharmaceuticals (as an antiseptic) and, as a pigment, sensors, among others.

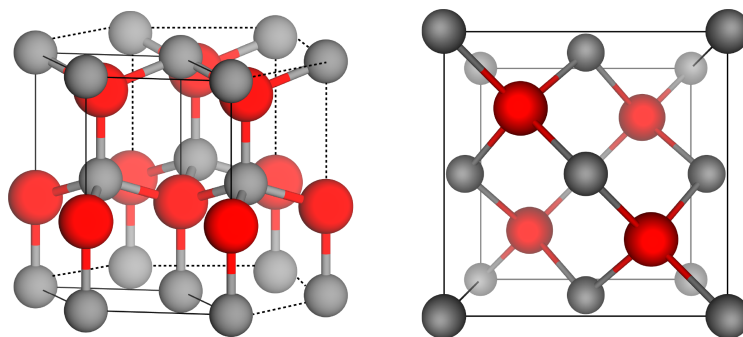


Figure 1.1 Wurtzite and zincblende structures of zinc oxide. Red and grey circles represent oxygen and zinc.

1.3 Thesis Outline

In this Thesis, the main focus is on the structural and electronic properties of zinc oxide surfaces, coupling the computational and experimental results of others, whenever they are available, with our own theoretical calculations. The following information is presented and discussed: Chapter 2 provides the fundamental background of the theory and computational methodology used in the work presented in this Thesis. However, a more detailed description of specific methods used is also provided in every chapter that follows. In Chapter 3, findings regarding the structural and electronic properties of the bulk and nonpolar surfaces of ZnO by means of IP and DFT methods are presented. In Chapter 4, the origin of the stability of ZnO polar surfaces through the employment of highly accurate interatomic potentials is illustrated. In Chapter 5, the fitting of Cu/ZnO IP to DFT structures and energies

is described. As a showcase for the new Cu-ZnO IP, global optimisation calculations of eight Cu atoms deposited on the $(10\bar{1}0)$ surface are included. In Chapter 6, DFT calculations in search of the most stable atomic structure of MoO_3 supported (0001) Fe_2O_3 catalyst are reported. Calculations presented in Chapter 6 aim to help the fit of Extended X-ray Absorption Fine Structure (EXAFS) parameters by suggesting stable $\text{MoO}_3/\text{Fe}_2\text{O}_3$ atomic structures. Finally, Chapter 7 summarises and concludes the work realised throughout this Thesis.

Chapter 2

Theoretical Methods

2.1 Introduction

Modelling materials using computational techniques has become a well established way of doing chemistry and physics, which is becoming more popular and is now widely accepted among the scientific community. Computational chemistry techniques are used to calculate accurately structural parameters and electronic properties of a material and are complementary with experiment. These methods are employed successfully for a wide range of fields including solid-state chemistry, catalysis, condensed matter physics, material science, among others, where they help with decoding the experimental data as well as suggesting and designing new experiments. Computational chemistry techniques also offer a fast and safe methodology in the design and discovery of new materials.

Interatomic potential (IP) and quantum mechanical (QM) methods are two of the most widely used approaches in modelling materials. Generally, the first goal of these methods is to find the lowest energy structure of a given material. The difference between QM and IP methods relies on the properties they were designed to model. While IP methods provide a fast description of bulk properties, lattice and surface energies, and defect analysis, QM methods give information about bonds, electronic structure, and reactivity. From this point of view, QM methods are a level of theory higher and computationally more demanding than IP, although the latter may be more appropriate for a number of problems. Selecting the appropriate

level of theory can be one of the more difficult tasks in computational chemistry [24]; IP are suitable for systems containing up to several thousand atoms where the role of the electronic properties are diminished and they are often used for a pre-screening of the QM models. On the other hand, QM models are used to model up to a few hundred atoms, due to the computational effort required, where an explicit knowledge of electronic structure is needed.

Both IP and QM techniques have been applied in the study of metal oxide surfaces. They have been used in the investigation of defects and surface structures because of the difficulties involved in experimental structure determination [13]. In the case of ZnO and Fe₂O₃ surfaces, they have provided a deeper insight into the atomic structure and electronic properties of such materials because of the limitations of experimental studies.

In this Chapter, we will discuss the methods and theory underpinning the work presented in this Thesis. Firstly, we give a brief description of a crystalline material, periodic boundary conditions and the reciprocal space. Secondly, we review the theory behind the IP and QM methods and the approximations linked to them. We then continue with a summary of the global and local optimisation techniques, and additionally, we describe the defect calculations and surface modelling methods. Finally, details on the software packages used in this Thesis are given.

2.2 Crystalline Materials

An ideal crystal is a solid material where its atomic structure can be represented by an infinite repetition of an individual atom or a group of atoms, called the basis. This group of atoms is attached to an infinite array of discrete points called Bravais lattice. The Bravais lattice defines the lattice type. The mathematical expression of the position vector of all Bravais lattice points, for a given point, can be written as:

$$\mathbf{R} = n_1\mathbf{a}_1 + n_2\mathbf{a}_2 + n_3\mathbf{a}_3, \quad (2.1)$$

where \mathbf{a}_i are the vectors of the unit cell and n_i are integers. This vector \mathbf{R} has the property that for any integer value, the lattice looks exactly the same.

In the case of wurtzite ZnO and α -Fe₂O₃, the crystal structures that are the focus in this Thesis, the Bravais lattices are hexagonal and rhombohedral, respectively. The crystal lattice is defined by a combination of the Bravais lattice and the basis. In order to build-up a crystal, all the information needed is the parallelepiped formed by the smallest unit of volume which contains the position of the atoms and symmetry; this parallelepiped is the unit cell.

2.2.1 Periodic Boundary Conditions

Periodic boundary conditions (PBC) are used to simulate an infinite system by using a small part of it (e.g. a unit cell). Figure 2.1 is a two dimensions representation of the periodic boundary conditions applied to a unit cell. The unit cell has been duplicated in x and y directions creating exact images with the same characteristics as the original one. If an atom is taken outside of the original unit cell through the right wall, its image simultaneously will enter the original unit cell through the left wall from the periodic image as shown in Figure 2.1. In the calculation of properties of solids, PBC are needed to represent a system with an infinite number of atoms/electrons.

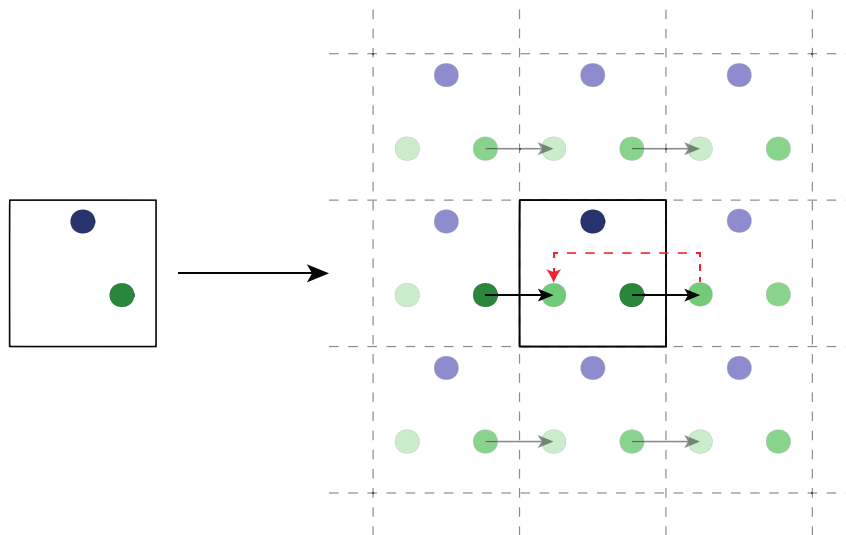


Figure 2.1 Periodic boundary conditions in two dimensions. A unit cell is shown on the left-hand side of the picture. The periodic images on the right (presented with lighter colours) were generated by PBC. The arrows over the circles represent displacements of the atoms.

2.2.2 Reciprocal Space

In the study of solids, an alternative representation of the Bravais lattice is a reciprocal lattice. The reciprocal lattice can describe some phenomena in an easier way and it is essential in the study of periodic systems. It is extensively employed in the analysis of X-ray diffraction, electronic bands, phonon dispersion, and long range interactions (e.g. Coulombic interactions). In this Thesis, the reciprocal space was used within computational codes to calculate properties of ZnO and Fe₂O₃.

In the case of a cubic system, the reciprocal lattice can be defined by three reciprocal vectors: \mathbf{b}_1 , \mathbf{b}_2 , \mathbf{b}_3 , as follows:

$$\mathbf{b}_1 = 2\pi \frac{\mathbf{a}_2 \times \mathbf{a}_3}{\mathbf{a}_1 \cdot (\mathbf{a}_2 \times \mathbf{a}_3)}; \quad \mathbf{b}_2 = 2\pi \frac{\mathbf{a}_3 \times \mathbf{a}_1}{\mathbf{a}_1 \cdot (\mathbf{a}_2 \times \mathbf{a}_3)}; \quad \mathbf{b}_3 = 2\pi \frac{\mathbf{a}_1 \times \mathbf{a}_2}{\mathbf{a}_1 \cdot (\mathbf{a}_2 \times \mathbf{a}_3)}. \quad (2.2)$$

The vectors \mathbf{a}_1 , \mathbf{a}_2 , \mathbf{a}_3 describe the lattice in real space. Each vector presented in (2.2) satisfies the orthogonality condition $\mathbf{b}_i \cdot \mathbf{a}_j = 2\pi \delta_{ij}$. As an analogy of Equation (2.1), the vector that represents all reciprocal lattice points can be written as:

$$\mathbf{K} = n_1 \mathbf{b}_1 + n_2 \mathbf{b}_2 + n_3 \mathbf{b}_3. \quad (2.3)$$

As the unit cell in real space described by the Bravais vectors, the first Brillouin zone is a uniquely defined unit cell in reciprocal space. The dimensions of this cell are given by the vector \mathbf{K} . Any point in the reciprocal space can be represented by a vector \mathbf{k} , often called wave vector due to its units of inverse length. The importance of the Brillouin zone is that it depicts all of the Bloch states/waves without redundancy. The Bloch theorem states that the solutions of the Schrödinger equation in a periodic system may be written as:

$$\psi_{\mathbf{k}}(\mathbf{r}) = u_{\mathbf{k}}(\mathbf{r}) e^{i\mathbf{k} \cdot \mathbf{r}}, \quad (2.4)$$

where $\psi_{\mathbf{k}}(\mathbf{r})$ is a Bloch wave, \mathbf{k} is the wave vector, $u_{\mathbf{k}}(\mathbf{r})$ is function with the periodicity of the crystal such as $u_{\mathbf{k}}(\mathbf{r}) = u_{\mathbf{k}}(\mathbf{r} + \mathbf{R})$.

2.3 Interatomic Potential Methods

2.3.1 Introduction

Interatomic potential, also known as atomistic or force field, techniques are an efficient approach to determine the atomic structure of material. Force field methods use a parameterised interaction potential between ions as a function of the nuclear coordinates. This parameterisation may be based on experiments and/or on a higher level of theory (e.g. those derived from quantum mechanics). Since interatomic potential methods neglect both the solution of the electronic Schrödinger equation and the quantum aspects of the nuclear motion, they are incapable of calculating the electronic properties of a material. However, in spite of the lack of the electronic description of the material, interatomic potential methods have been shown to accurately reproduce the crystal surface structures and properties [25–29]. Owing to its simplicity, atomistic methods can provide the atomic structure of a system containing thousands of atoms in a relatively short amount of computational time. The General Utility Lattice Package (GULP) [30, 31] was used in this Thesis for all the atomistic calculations presented.

2.3.2 The Calculation of the Energy

The calculation of the energy of a system is essential in modelling materials and is the first step for the majority simulation techniques [31]. Thus, the stability of a material is determined by its energy: lower energy indicates greater stability. In theory, the internal energy of a solid is a function of the positions and momenta of all electrons and nuclei, which it is indeed a very complicated problem. In order to simplify this calculation, interatomic potential methods incorporate the effect of the electrons into a single atomic centre. Thereby, the energy of a system can be decomposed into an expansion in terms of interactions between different subsets of the total number of atoms, N [31]:

$$U = \sum_{i=1}^N U_i + \frac{1}{2!} \sum_{i=1}^N \sum_{j=1}^N U_{ij} + \frac{1}{3!} \sum_{i=1}^N \sum_{j=1}^N \sum_{k=1}^N U_{ijk} + \dots, \quad (2.5)$$

where the first term U_i represents the self energies of the atoms, the second U_{ij} the two-body interactions, the third U_{ijk} the three-body interactions, etc. For the majority of the systems, we find that as the order increases so its contribution to the energy decreases. Therefore, to simplify the problem, a common approach is to neglect the contributions of higher orders. In this Thesis, only the first two terms were used: the first is due to the atomic polarisation as a result of external potential fields whereas the second represents the pairwise interactions between atoms such as Coulomb interactions.

2.3.3 Two-Body Potentials

The electrostatic interaction is a two-body potential, a result of the force acting on a charged atom due to the presence of another charged atom. This interaction is described by the Coulomb potential and can represent up to 90% of the total energy [31]. This potential is represented by Coulomb's law:

$$U_{ij}^{Coulomb} = \frac{q_i q_j}{4\pi\epsilon_0 r_{ij}}, \quad (2.6)$$

where q is the charge of the ion, ϵ_0 is the vacuum permittivity, and r_{ij} is the distance between the two ions. Its form is very simple but its evaluation in periodic systems needs care [31], as the energy decreases at a rate of $\frac{1}{r}$; however, the number of ions contributing to the total energy increases at a rate equal to the surface area of a sphere, which is $4\pi r^2$. Thus, the Coulomb energy does not converge with respect to the distance r . To compute this term, the most widely used solution is the Ewald summation [32], which uses a partial transformation into reciprocal space.

Besides the Coulomb potential, the Lennard-Jones (LJ) [33], the Buckingham [34] and the Morse potentials were employed to model the short range interactions. These are the standard short-range potentials used for modelling many ionic materials; they are purely two-body, i.e. a function of the interatomic distance r between ions.

The Lennard-Jones potentials have the following analytical form:

$$U_{ij}^{Lennard-Jones} = \frac{B}{r_{ij}^{12}} - \frac{C}{r_{ij}^6}, \quad (2.7)$$

where B and C are the parameters to fit either to experiment and/or accurate *ab initio* calculations. Here the first term on the right is the repulsive term and is due to the overlap of the electronic wave functions, also known as Pauli repulsion. The second term on the right, the r_{ij}^6 term, is the attractive long-range term; this is the dispersion (van der Waals) force which results from the instantaneous induced dipoles on the atoms. Because of the shape of the potential, there is a distance r_{ij} where the energy reaches a minimum value, which corresponds to the equilibrium bond distance. For smaller values than the equilibrium bond distance, the atoms experience a repulsion and for larger values attraction.

An improvement to the Pauli repulsion term of the LJ potential was given by R. A. Buckingham [34]:

$$U_{ij}^{Buckingham} = Ae^{\left(\frac{-r}{\rho}\right)} - \frac{C}{r_{ij}^6}. \quad (2.8)$$

Here, the last term on the right is the same dispersive term used in the LJ potential (Equation (2.7)). The modification of the repulsive term from $\frac{1}{r^{12}}$ to an exponential decay is supported by the radial fall off of electron density which is also found to be exponential.

The Buckingham potential has a problem for short interatomic distances, as $r \rightarrow 0 \Rightarrow U_{ij}^{Buckingham} \rightarrow -\infty$, which can be problematic where the distance between the atoms is much smaller than a typical bond length which is, however, usually unrealistic; nevertheless, this problem can be avoided by using sensible cut-offs and/or adding the LJ repulsive term.

Another short-range potential widely used is the Morse potential, which is appropriate when the interacting atoms are covalently bonded. In this work, this potential is very useful in the modelling of the Cu/ZnO system. This potential can be

represented as:

$$U_{ij}^{Morse} = D_e((1 - \exp(a(r_{ij} - r_0)))^2 - 1.0), \quad (2.9)$$

where D_e is associated with the binding energy, r_0 is the equilibrium bond distance and a controls the thickness of the potential well.

The LJ, Buckingham and Morse potentials are short-range, where the energy decays to zero rapidly as r is increased; the shape of a typical short-range curve is displayed in Figure 2.2. Thus, a sensible radial cut-off can be applied to these potentials to reduce the computational cost without affecting the accuracy of the calculations.

2.3.4 Shell Model

Polarisation effects are very important in a material such as ZnO, so the shell model was employed [35]. In this model atoms are considered as a charged core (nuclei and the inner electrons) connected by a harmonic spring to a massless charged shell (the outer valence electrons). Figure 2.2 shows a schematic representation of this model. The short-range potentials only act between shells. This term is known as the spring potential, which can be written as:

$$U^{spring} = \frac{k_2 r^2}{2} + \frac{k_4 r^4}{24}, \quad (2.10)$$

where r is the distance between the centre of mass of the core and shell, and k_2 and k_4 are spring constants. Note that this potential only acts between core and shell of the same atom, whereas the Coulombic forces are present between the core and shell point charges of an ion and both the core and shell of other ions but not between core and shell of the same ion.

2.3.5 Many-body Potentials

In some cases the simple two-body potentials like the ones described above are insufficient and many-body potentials may be needed at the expense of a higher computational cost. The following are common forms of many-body potentials:

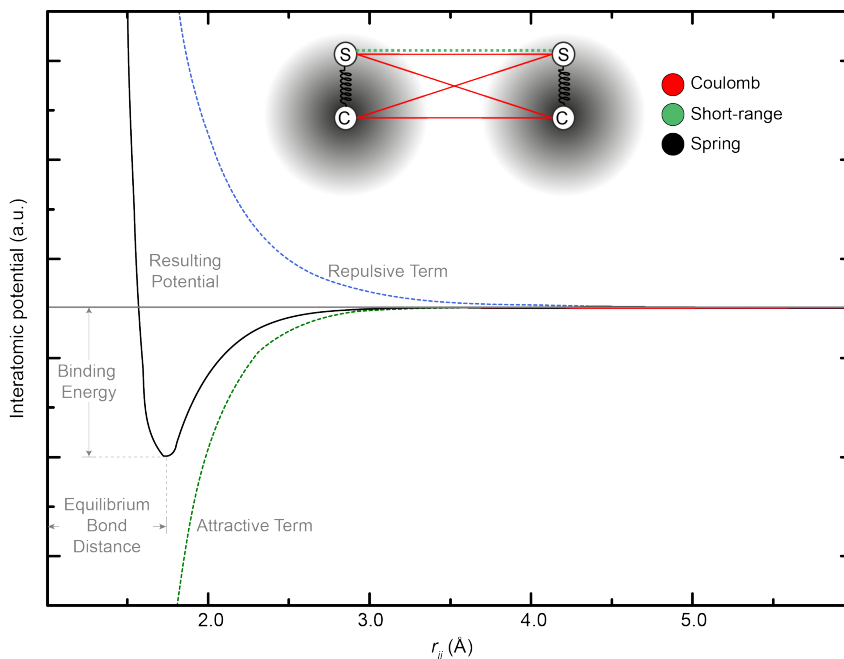


Figure 2.2 Typical shape of a two-body potential as a function of the interatomic distances r_{ij} . The subfigure at the top is a representation of the shell model interactions. The indices “C” and “S” are used to represent the cores and shells, respectively. The charged points, core and shell, experience Coulombic forces. The short-range interactions only act on the shell of an ion. The spring potential models the core-shell interactions.

The Embedded Atom Model

The embedded atom model (EAM) is an approach that has been used successfully in the description of metallic materials [31]. One of the advantages of the EAM is that it does not need reparameterisation once the potential is fitted. This potential is an attempt to model the energy as a function of the electron density of a system, as in *ab initio* methods. However, in order to simplify the problem and make the calculations cheaper, it expresses the energy as a function of the density at the nucleus of an atom, summed over all particles [31]:

$$U^{EAM} = - \sum_{i=1}^N f(\rho_i). \quad (2.11)$$

In this Thesis, the embedded atom model was used to represent the Cu-Cu interactions as it has been shown to model successfully those interactions [8]. There are different variations of the functional and the density which can be consulted in Ref.

31. In this work, the shape of the density functional was represented by the power law:

$$f(\rho) = A\rho^{\frac{1}{n}}, \quad (2.12)$$

and the representation of how the density varies with distance as:

$$\rho_{ij} = A \exp\left(-\beta \left(\frac{r_{ij} - r_0}{r_0}\right)\right). \quad (2.13)$$

2.3.6 Fitting Potentials

A set of new potentials for the Cu/ZnO system were developed. Fitting potentials may be turned out to be a very difficult task, as it is an iterative process where the potentials are fitted to a set of observables. The observables can be obtained from either experimental data or *ab initio* calculations. If fitted from *ab initio* calculations, the observables are usually a set of energies or derivatives of the energy that correspond to a unique structure.

The objective of fitting potentials is to minimise the sum of squares, representing the quantity of the value that evaluates the quality of the fitting. The analytical form of the sum of squares can be defined as follows:

$$F = \sum_{all\ observables} w(f_{calc} - f_{obs})^2, \quad (2.14)$$

where f_{calc} and f_{obs} are the calculated and observable data and w is a weighting factor given to each observable. The w factor is introduced as an indication of the reliability of the data points. Furthermore, w can be weighted more for the points that are close to the equilibrium bond length to gain a better representation of this part of the curve.

2.4 Quantum-Mechanical Methods

2.4.1 Introduction

Interatomic potential methods cannot be used for describing many of the electronic properties of a material. To model electrons, quantum mechanics must be used

[36, 37]. Subatomic particles exhibit both wave and particle properties and are distributed through space as waves. The behaviour of a particle can be described by its wavefunction (ψ) which is determined by solving the Schrödinger equation. For a time-independent system and one dimension system, the Schrödinger equation is of the form:

$$-\frac{\hbar^2}{2m} \frac{d^2\psi(x)}{dx^2} + V(x)\psi(x) = \hat{H}\psi(x) = E\psi(x), \quad (2.15)$$

where m is the mass of the particle, $V(x)$ its potential energy at point x , \hbar is a modification of Planck's constant ($\frac{h}{2\pi}$), \hat{H} is the Hamiltonian operator and E is the total energy due to the sum of the kinetic and potential energies. Solving this equation allow us to obtain the energy of a system. However, the Schrödinger equation can only be solved exactly for the hydrogen atom and the H_2^+ molecule. Hence, the goal of the quantum mechanical methods is to get as close as possible to the exact solution of Schrödinger equation. To do this, there are two well known methods: Hartree-Fock (HF) and Density Functional Theory (DFT).

2.4.2 Hartree-Fock Method

All *ab initio* methods use approximations to solve the Schrödinger equation of a system. There is a set of approximations which is commonly used in all *ab initio* approaches. The first approximation taken into account is the Born–Oppenheimer. The Born–Oppenheimer (BO) approximation establishes that the wavefunction of a system can be broken into two separate terms: the first to describe the atomic nuclei and the second to express the electronic motion. The nuclear motion is neglected as a consequence of its higher mass. Therefore, the electronic wavefunction depends on the position of the nuclei but not upon their velocities. The second approximation made is that the potential of the Hamiltonian is time independent, as expressed in equation (2.15). Lastly, relativistic effects are not taken into account, i.e. the solution of the Schrödinger equation for systems containing heavy atoms is inaccurate.

The Hartree-Fock theory is one of the cornerstones of the electronic structure theory. HF attempts to solve Schrödinger equation for an electron in the potential of

the nucleus and all other electrons. In this method, the motion of one electron with respect to all other electrons is not neglected but expressed in an average manner. HF expresses each electron by an orbital and the total wavefunction is given by the product of these orbitals. Electrons are particles (fermions) with a spin quantum number of $\frac{1}{2}$, for which their wavefunctions are antisymmetric. To solve this, the solution of the many-electron wavefunction is approximated to a Slater determinant.

There is an implicit problem in the HF method: the position of the particles are needed to obtain the Hamiltonian, and the Hamiltonian is needed for particle positions. However, both are unknown. This problem is solved iteratively by the self-consistent field (SCF) method. Figure 2.3 describes a greatly simplified algorithmic flowchart of this process: (i) an initial guess set of atomic coordinates is given, (ii) the charge density is calculated, (iii) the potential is calculated, (iv) the Schrödinger equation is solved, (v) the new charge density is calculated. If the charge density is the same as before or if the difference between the new and the old charge densities falls below some threshold criterion, the self-consistency has been achieved. Otherwise, the process must be repeated.

The HF method gives reasonable values for total energies of atoms and molecules and a good description of exchange effects. On the other hand, it overestimates excitation energies and fails to reproduce metallic states.

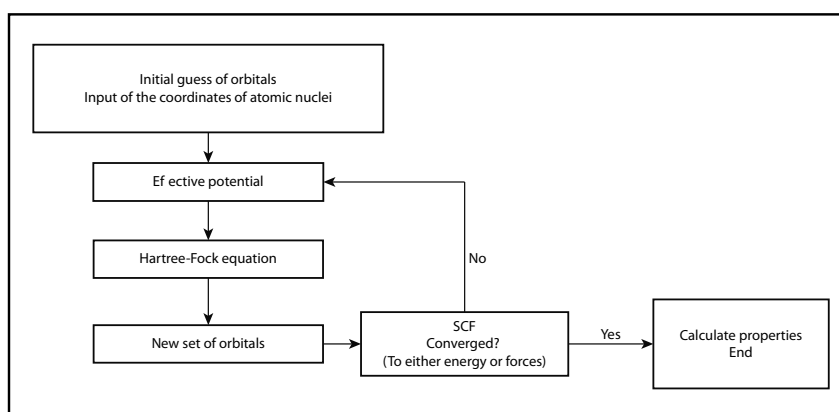


Figure 2.3 Simplified algorithmic flowchart illustrating the SCF method.

2.4.3 Density Functional Theory

Density Functional Theory is a method used to calculate the electronic structure of many-body systems. DFT is based on Hohenberg-Kohn theorems, which have the following consequences: i) there is a universal functional $F[\rho(\mathbf{r})]$ that allows the calculation of the energy from its electronic density, which can be written as:

$$E[\rho(\mathbf{r})] = \int V(\mathbf{r})\rho(\mathbf{r})dr + F[\rho(\mathbf{r})], \quad (2.16)$$

where

$$\int V(\mathbf{r})\rho(\mathbf{r})dr = V_{ne}[\rho(\mathbf{r})]. \quad (2.17)$$

Nonetheless, the form of the $F[\rho(\mathbf{r})]$ functional is unknown and (ii) all properties of the system are not calculated through the many-electron wavefunction but calculated from the electron density (ρ) and the total energy is obtained from it. Walter Kohn and Lu Jeu Sham (Kohn-Sham) [38] proposed a replacement of the real system by a fictitious one of non-interacting electrons, which generates the same density as any given system of interacting electrons. If the total energy is given by:

$$E[\rho(\mathbf{r})] = T_{ni}[\rho(\mathbf{r})] + V_{ne}[\rho(\mathbf{r})] + V_{ee}[\rho(\mathbf{r})] + E_{xc}[\rho(\mathbf{r})], \quad (2.18)$$

then T_{ni} is the non-interacting kinetic energy, V_{ne} is the nuclei-electron (Coulombic) potential energy, V_{ee} the electron-electron potential energy, and E_{xc} is the exchange-correlation (XC) energy which contains the difference between the exact and non-interacting kinetic energies. From all the terms expressed in equation (2.18), E_{xc} is the only one we do not know how to obtain exactly. However, the E_{xc} contribution may be small, hence a sensible approximation of E_{xc} would lead to a very good approximation to the functional F . The density for non-interacting electrons is given by:

$$\rho(\mathbf{r}) = \sum_{i=1}^n |\psi_i|^2, \quad (2.19)$$

As the potential is a function of the charge density $\rho(\mathbf{r})$, the KS equations must be solved with the SCF method, as in HF. One of the inaccuracies in DFT is in the

expression of the Coulomb energy. The expression of the Coulomb energy includes the interactions of each electron with all other electrons, but it also includes itself (in HF the self-interaction is cancelled by exchange). This electron self-interaction is spurious and will be described below. In DFT, the solution of the Schrödinger equation would be exact if we knew the exact form of the $E_{xc}[\rho(\mathbf{r})]$. DFT relies on the use of functionals which are approximate forms for the exchange-correlation energy; a description of the two most used approximations for the XC energy is given below.

2.4.3.1 Approximations for the Exchange-Correlation Energy

As is clear from the above discussion, the biggest error in DFT calculations comes from the approximation of the exchange-correlation energy. Hence, a huge effort of the research community is put into the search for more accurate approximations. To date, there are two commonly used approximations to the exchange-correlation energy: the local-density approximation (LDA) and the generalised gradient approximation (GGA). LDA depends purely on the electronic density at each point in space and treats the system as *locally homogenous*. For a spin-unpolarized system, the XC energy has the analytical form:

$$E_{xc}^{LDA}[\rho(\mathbf{r})] = \int d^3\mathbf{r} \rho(\mathbf{r}) \epsilon_{xc}^{LDA}(\rho(\mathbf{r})), \quad (2.20)$$

where $\epsilon_{xc}(\rho)$ is the XC energy per particle of a uniform electron gas of density ρ . The LDA approach is generally accurate for predicting structural properties; however, it is less suitable for charge-transfer systems and there are inherent errors in this approach such as:

- The electronic densities that are more homogeneous than the exact one are favoured.
- The functional tends to underestimate atomic ground state and ionisation energies.
- LDA overestimates binding and cohesive energies of solids.

- Van der Waals interactions are not reproduced.
- In general, LDA is not as good for small molecules as it is for larger size systems.

The second approximation to the XC energy is the general gradient approximation. The GGA is considered to be an improvement over LDA, because GGA methods take the variation of the electron density over space into account. This expression can be written as:

$$E_{xc}^{GGA} = E_{xc}[\rho(\mathbf{r}), \nabla\rho(\mathbf{r})],$$

or

$$E_{xc}^{GGA} = \int d^3\mathbf{r} \rho(\mathbf{r}) \epsilon_{xc}^{LDA}(\rho(\mathbf{r})) F(\rho(\mathbf{r}), \nabla\rho(\mathbf{r})).$$

Nowadays, there are many different functionals available to deal with the gradient of the electron density, commonly used ones are:

- Perdew-Burke-Ernzerhof (PBE) [39] functional. In this functional all parameters are fundamental constants. No fitting parameters are used in this functional.
- PBEsol [40] is a revised Perdew-Burke-Ernzerhof GGA that improves equilibrium properties of densely-packed solids and their surfaces.

The GGA functional provides very good results for molecular geometries, binding energies, and ground-state energies and there is a small improvement in the band gap of semiconductors and insulators over LDA (although standard DFT is not strictly suitable to calculate band gaps). However, lattice constants for noble metals are overestimated. Even with the consideration of the gradient of the electron density, the electron self-interaction remains, causing inaccuracies in the calculation of the total energy.

2.4.3.2 Approaches to Solve the Self-Interaction Problem

As noted, the self-interaction problem is the false interaction of an electron with itself. In HF methods, this term is explicitly cancelled out. In DFT, the electron

self-interaction would be cancelled if we knew the exact DFT exchange-correlation functional. As a consequence of this problem, DFT favours delocalised solutions where electrons do not interact greatly with themselves which is a problem for the description of strongly localised d or f states in transition metals, and band gaps are considerably underestimated for ionic and semi-ionic compounds. In an attempt to solve this problem, two approaches have been developed with notably improved results: hybrid functionals and DFT + U methods. In the former, the exchange correlation energy is composed of a portion of exact exchange energy from Hartree-Fock theory and a portion of DFT functional. In the DFT + U method, localized d and f electrons are separated from the delocalized s and p . The localized electrons are treated with the Hubbard model [41] based correction, whereas the localized ones with normal LDA/GGA functionals. This approach requires a Coulombic “ U ” parameter which is fitted to reproduce experimental data, e.g. band gaps.

Basis Set

Most calculations express the molecular orbitals using a basis set, which is a set of functions which are combined to create molecular orbitals. These functions can be atomic orbitals centred on atoms (localized basis sets) or plane waves. The former is mostly used for isolated atoms and molecules whereas plane waves are typically used for periodic systems. In this Thesis, plane wave basis sets were chosen in our periodic calculations. In plane-wave basis sets the wavefunction of one electron can be written as:

$$\psi_{\mathbf{k}}(\mathbf{r}) = \sum_{\mathbf{G}} c_{\mathbf{k}+\mathbf{G}} \exp[i(\mathbf{k} + \mathbf{G}) \cdot \mathbf{r}], \quad (2.21)$$

where \mathbf{k} and \mathbf{G} are reciprocal lattice vectors, and $c_{\mathbf{k}+\mathbf{G}}$ are coefficients for the plane waves. Equation (2.21) is a sum of plane waves, which have the property that any wavefunction with index \mathbf{k} is identical to one with $\mathbf{k} + \mathbf{G}$ index. Consequently, it is only needed to find the solution for \mathbf{k} values in one unit cell in the reciprocal space, as suggested previously in page 28.

2.4.3.3 Energy Cut-off and the k -mesh

The size of the basis set is very important; a larger basis means a calculation more accurate and more expensive. In fact, to recreate exactly the real wavefunction, an infinite number of basis functions would be needed. As this is intractable, the number of wavefunctions needs to be controlled by imposing a cut-off on the kinetic energy: the cut-off energy is chosen by defining the maximum kinetic energy of the electrons in the system, and determines the size of the basis set. Generally, a cut-off of a few hundred electronvolts is chosen for the first calculation, then the cut-off is increased until reaching the desired convergence, typically 1 meV in the total energy.

Another important parameter to choose is the representation of the first Brillouin zone. This representation is given by a number of points in the Brillouin zone, known as the \mathbf{k} -point mesh. In principle, there should be a set of orbitals for every possible value of \mathbf{k} ; in reality, we need to choose a finite number of \mathbf{k} -points which are distributed evenly throughout the Brillouin zone according to a Monkhorst-Pack scheme [42]. The Monkhorst-Pack scheme consists of choosing a set of \mathbf{k} -points ($M_x \times M_y \times M_z$), where the subscript indicates the direction of the wave vector for sampling the Brillouin zone. As with the cut-off energy, the greater number of \mathbf{k} -points, the finer, more accurate and more expensive the calculation will be. The set of \mathbf{k} -points required for describing a system depends on the system under study. Usually tests are performed, where the number of \mathbf{k} -points is increased until the desired convergence is reached.

2.4.3.4 Pseudopotentials

The core and valence electrons behaviour is completely different. Valence electrons affect the chemical and electronic properties. Whereas, the core electrons are well localised and tightly bound to their nuclei and their properties do not change significantly with the chemical environment of the atom. To simplify further the problem of modelling a material, pseudopotentials are used. Pseudopotentials treat core and valence electrons differently: core electrons are incorporated into a nuclear potential (or pseudopotential) and valence electrons are described by a softer effective

ionic potential. Some of the advantages given by the use of a fictitious potential are given in the following list:

- Core electrons are removed from the calculation so only valence wavefunctions need to be calculated.
- A lower cut-off energy can be used to represent orbitals. Core electrons have very high kinetic energy and there is no need to use plane waves for these electrons.
- They can be optimised. Pseudopotentials are not defined for a particular element; the shape of the potential can be modified in such a way to use as low required cut-off energy as possible.
- There is the possibility to include relativistic effects. Relativistic effects affect core electrons; pseudopotentials can be created to deal with this problem.

Among the most used pseudopotentials are: the norm-conserving pseudopotentials [43], the Vanderbilt ultrasoft pseudopotentials (USPP) [44], and the projector-augmented wave (PAW) [45]. The basis set for norm-conserving potentials can be very large for some elements, whereas for USSP the number of plane waves per atom is reduced. PAW potentials are similar to USSP; the difference is that the core electron is frozen and only valence electrons are relaxed, allowing efficient DFT calculations.

2.5 Surface Calculations

In chemistry, surfaces are very important since they control the interaction of the material with other compounds. The surface properties determine the shape of a crystal, moreover, catalysis and reactions processes occur principally on the surface of a material. Surface models are usually created by cleaving a crystal.

In computational chemistry, calculations are performed to obtain both surface atomic structure and surface properties usually in a straightforward way. On the other hand, obtaining those same properties from experiment involves many difficulties, which makes computational methods very attractive as they can give us an

explanation of a specific property or help us to build an understanding of its atomic structure.

One of the most important properties of a surface is its surface energy, as this property determines its stability. Given a bulk energy containing the same number of atoms as the slab, U_{bulk} , and a relaxed energy of the cleaved system, U_{slab} , then the surface energy $U_{surface}$ is defined by:

$$U_{surface} = \frac{U_{slab} - U_{bulk}}{A}, \quad (2.22)$$

where A is the total surface area exposed of the cleaved system. Usually, when a crystal is cleaved it creates two surfaces i.e. one of each side on the slab, so the A includes both areas. For any stable material, the surface energy must be positive. When a crystal is cleaved the periodicity is broken in the direction normal to the surface. This cleaved surface is unstable due to the lower coordination number of the surface atoms and the atoms will relax in order to stabilise the surface.

There are two widely used methods in the modelling of surfaces, which are illustrated in Figure 2.4. The first is the two region model (or one-sided surface). This method shows periodicity in two directions parallel to the surface and the slab is split it into two regions. Region one is next to the vacuum and contains the surface atoms which are allowed to relax, whereas region two is held fixed representing the bulk crystal. The number of atomic layers in regions one and two have to be sufficiently large to represent the surface and bulk properties, respectively. The second method is the periodic slab model. In a periodic slab model (or two-sided surface), both terminations of the slab are allowed to relax. The introduction of a vacuum slab perpendicular to the surface is needed to avoid interactions between surfaces. Here, two major considerations need to be taken into account to calculate an accurate value for the surface energy: the vacuum gap needs to be large enough to minimise any interaction between slabs, and the slabs need to be thick enough so that its centre resembles the bulk. Usually, the atomic layer at the centre of the slab is fixed to restrict any translations parallel to the surface. This method is used in codes that only work with three-dimensional boundary conditions, such as those

based on plane waves.

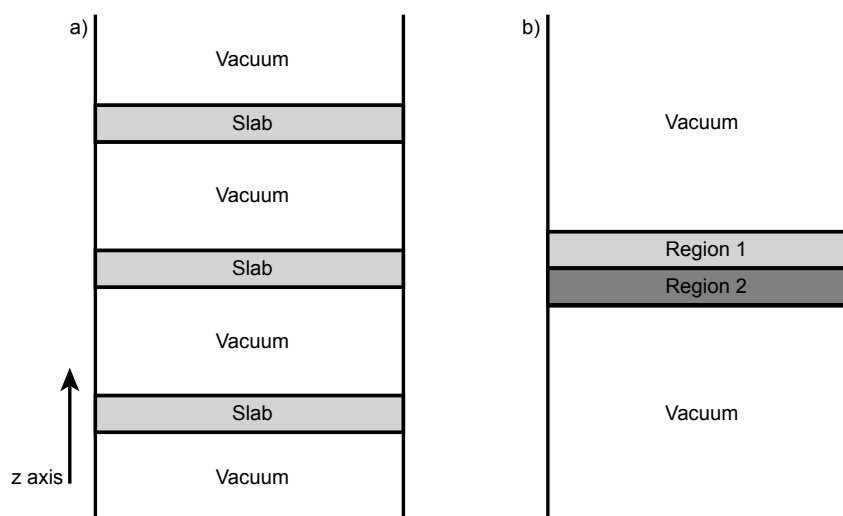


Figure 2.4 Representation of (a) the periodic slab model and (b) the two region model

According to Tasker [46], any surface of an ionic material can be classified into three different categories. This classification was made according to the charge distribution of the atomic layers within a repeat unit and the dipole moment produced by this distribution, as illustrated in Figure 2.5. Type 1 surfaces have atomic planes composed of equal numbers of anions and cations; the dipole is zero. In type 2, surfaces consist of charged planes but there is no net dipole perpendicular to the surface in the repeat unit because of the symmetrical stacking sequence. Lastly, type 3 surfaces exhibit a dipole moment perpendicular to the surface. According to electrostatic principles, types 1 and 2 should have modest surface energies and, therefore, should be stable after relaxation of the surface ions. On the other hand, type 3 surfaces need major atomic or electronic reconstructions on the surface in order to minimise for the dipole formed. Theoretically, when a dipole moment exists in each repeat unit perpendicular to the surface, the electrostatic energy density diverges with slab thickness and the surface energy tends to infinity.

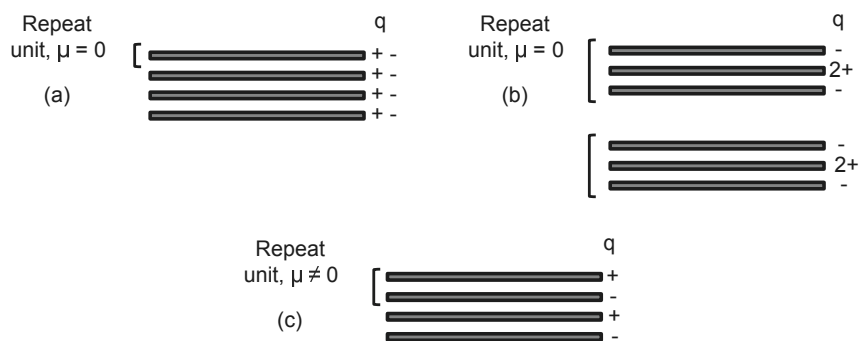


Figure 2.5 The three types of Tasker's surfaces. (a) Type 1, same number of anions and cations on each plane, nonpolar surface. (b) Type 2, charged planes but no net dipole moment normal to the surface. (c) Type 3, alternating layers of cations and anions which lead to charged planes and a dipole moment perpendicular to surface

2.6 Implementation

In this Thesis, we use interatomic potential and density functional methods to study bulk and surface properties of metal oxides. In this, section we will focus on aspects of IP and DFT of greatest relevance to this Thesis and their implementation for the systems discussed here. In this Thesis, the General Utility Lattice Program [30, 31] and periodic DFT code VASP [47, 48] were employed for interatomic potential and *ab initio* calculations, respectively. More details will be included in the following chapters.

2.6.1 General Utility Lattice Program (GULP)

The General Utility Lattice Program [30, 31] is an interatomic potential based program, ideal for modelling ionic solids. It is capable of dealing with solids, clusters, defects, surfaces, interfaces and polymers. All interatomic potential calculations presented in this Thesis were performed with the GULP code, which requires only a single input file. The GULP input file has all the necessary information to perform an atomistic calculation, and is usually distributed as follows: (i) the first line include the keywords of the calculation, for example, opti (optimise), conv (constant volume), conp (constant pressure), single (single point calculation), phonon, defect, among others. (ii) next, the dimensions of the cell are given: lattice parameter lengths and the angles between them, followed by (iii) the position of the atoms, which can be in either fractional or Cartesian coordinates. (iv) The charge of each

element is specified along with the interatomic potentials and cut-offs for each short range interaction. Finally, the output is given in one single text output file.

2.6.2 Vienna Ab-initio Simulation Package (VASP)

VASP uses DFT with a plane wave basis set to describe the valence electrons states [47, 48]. Interactions between the cores and the valence electrons are described using the projector-augmented wave (PAW) [45, 49] method. Exchange and correlation energy is treated with two different generalized gradient approximations (GGA): Perdew-Burke-Ernzerhof (PBE) [39] and PBE functional revised specifically for solids: PBEsol [40]. PBE0 and PBEsol0 hybrid exchange-correlation (xc) functionals are used with a 25% of the exact exchange from Hartree-Fock (HF). VASP calculations need four input files: POSCAR, INCAR, POTCAR and KPOINTS. The POSCAR file contains the lattice parameters and atomic coordinates of each atom. All the setup parameters are specified in the INCAR such as force tolerances, plane wave cutoff, functional and optimisation technique. The POTCAR file lists the potentials used. Lastly, the KPOINTS file contains the k -mesh used.

2.6.3 Knowledge Led Master Code (KLMC)

The Knowledge Led Master Code code is used in this Thesis in an attempt to obtain the global minimum (GM) of the atomic reconstructions at the ZnO polar surfaces. This task required the creation of more than 500,000 input files. The only feasible way of doing this was by using our in-house code KLMC [50, 51]. KLMC automates many repetitive or complex tasks, traditionally performed by the user, using a range of third party codes (in this case, GULP). Some of these tasks include the creation and modification of input files and the extraction of information from output files.

Within KLMC, we use the “solid solutions” routine as a global optimisation technique. In this routine, KLMC creates a grid based on the initial ion bulk positions given in the input. It then automates the substitution of atoms among the different predefined lattice sites. KLMC also reports the frequency of each unique

surface structure found; this frequency is used in post analysis of the patterns discovered. More details of the use of this routine will be given in Chapter 4.

2.7 High Performance Computing (HPC)

The work in this Thesis was underpinned with the facilities of the high-performance computing services. Most of the calculations required a large number of processing cores, for which we employ high-performance computing services which use large numbers of processing cores in a tightly-coupled, parallel fashion. The UK's national high-performance computing services HECToR and ARCHER were used during the realisation of the work presented here. To date, ARCHER is the latest UK national supercomputing service [52]. The ARCHER supercomputer is a Cray XC30 funded by EPSRC, NERC, EPCC and Cray Inc. ARCHER is about three times faster than its predecessor, HECToR, and is hosted by the University of Edinburgh. For a set of smaller calculations, the compute clusters Legion and Iridis were used. Legion is a centrally funded computing facility aimed at supporting all types of research at UCL [53] and Iridis is available to the University's entire research community based at the University of Southampton [54].

Chapter 3

Bulk and Non-polar Surfaces of ZnO

3.1 Introduction

In this Chapter, we will focus on the structure and electronic properties of the bulk and nonpolar surfaces of zinc oxide. The chemical and physical properties related to the surface structures of ZnO are of fundamental interest and are also key to the material's applications. Accurate characterisation of surface structure and properties is therefore essential. In the bulk, the wurtzite structure (zincite, see Figure 3.1) is the most stable polymorph of ZnO over a wide range of temperature and pressure [16]. This structure has four principal low-index surfaces: two side faces that are non-polar, $(10\bar{1}0)$ and $(11\bar{2}0)$; and two opposite polar, (0001) -Zn and $(000\bar{1})$ -O. These surfaces are composed of equal numbers of cations and anions in each layer. ZnO films with nonpolar surfaces have attracted attention due to their novel properties, which show higher emission efficiency for blue or ultra-violet LEDs [18–21].

Despite all the computational and experimental efforts, there are two major issues to address in gaining an understanding of the ZnO surface properties. First, the character of the atomic relaxation at clean surfaces compared to bulk and second, the electronic structure of such surfaces. We therefore report a detailed theoretical study of the two main nonpolar wurtzite ZnO surfaces: $(10\bar{1}0)$ and $(11\bar{2}0)$, including the atomic structure of the clean surfaces, stability of both morphological features and vacancies, the effect of specific surfaces feature (steps, dimer vacancies and grooves) on the ionisation potential and surface band bending. Calculations were

performed using a combination of different approaches: interatomic potentials and density functional theory. Our analysis leads to clear and coherent models for these two key surfaces of this widely studied material.

3.2 Calculation Settings

The periodic DFT code VASP (Vienna Ab initio Simulation Package) [47, 48] (introduced in Chapter 2) was employed in this study. As noted in Section 2.6.2, VASP uses a plane wave basis set to describe the valence electronic states. Exchange and correlation energy was treated with two different generalized gradient approximations (GGA): Perdew-Burke-Ernzerhof (PBE) [39] and PBE functional revised specifically for solids: PBEsol [40]. PBE0 and PBEsol0 hybrid exchange-correlation (xc) functionals were used with 25% of the exact exchange from Hartree-Fock (HF). Interactions between the cores (Zn:[Ar] and O:[He]) and the valence electrons were described using the projector-augmented wave (PAW) [45, 49] method.

In the study of defective surfaces, we have also used a complementary atomistic approach. The interatomic potential (IP) code GULP (General Utility Lattice Program) [30, 31] was used to study morphological features, including steps, dimer vacancies and grooves, at the $(10\bar{1}0)$ ZnO surface. We used the Born, shell model potentials for ZnO developed by Whitmore, Sokol and Catlow [55], which show excellent agreement with a range of experimental data (see Table 1 in Ref. 55). Moreover, DFT theory was used to verify the structure and stability of these defective ZnO surfaces. The detailed description of the defective ZnO surface models derived from both the DFT and IP techniques is given in the following section.

3.2.1 ZnO Bulk (DFT-based)

For the structural optimizations, we checked convergence of the total energy with respect to k -mesh sampling and plane wave energy cut-off; the total energy was converged to 1 meV. For GGA functionals, good convergence was achieved with a cut-off of 700 eV and a k -mesh of $11 \times 11 \times 9$ was used for both bulk relaxations and density of states (DOS). The iterative relaxation of the ions was not stopped

until the forces on the ions were all less than $0.01 \text{ eV}\text{\AA}^{-1}$. For hybrid functionals, the total energy criteria was kept as in the GGA functionals. A cut-off of 500 eV and a k -mesh of $9 \times 9 \times 7$ was found to be sufficient to converge for bulk relaxations and DOS. The structures were deemed to converge when the force on every ion was less than $0.01 \text{ eV}\text{\AA}^{-1}$.

3.2.2 Surface Models of ZnO (DFT-based)

For the clean ZnO surfaces, cell parameters and atoms in the middle layer were kept fixed, whereas the other ions were allowed to relax. The surface energy (E_{surf}) was converged to 1 mJ/m^2 with respect to the thickness of the slab and k -mesh sampling. Convergence was fully achieved for a cell with 15 *double* layers (60 atoms) and 15 layers (60 atoms) for the $(10\bar{1}0)$ and $(11\bar{2}0)$ surfaces, respectively. The slabs were separated by a vacuum gap of 15 \AA . A k -point sampling of $7 \times 7 \times 1$ was found to be sufficient. The cut-off energy was kept as in the bulk.

3.3 ZnO Bulk

Zinc oxide crystallizes in two main structures: hexagonal wurtzite and cubic zincblende. The former is the most stable over a wide range of temperature and pressure, including ambient conditions. In this Thesis, all the calculations are performed on the ZnO wurtzite structure, of which the atomic structure is shown in Figure 3.1. The wurtzite structure has all his atoms in a tetrahedral coordination.

From the lowest available temperature, neutron single crystal diffractometry at 20 K [23], the lattice parameters a and c are calculated to be 3.2417 \AA and 5.1876 \AA and the internal parameter u was determined as 0.3819, all showing good agreement with experimental data (Table 3.1). It is seen that PBEsol and PBEsol0 functionals show a better agreement for the lattice parameters a and c . For the internal lattice parameter u , the best agreement was found with the hybrid functionals (0.26% variation). Higher cut-off energies (900 eV) do not improve the results.

With respect to its electronic structure, a direct band gap of 3.44 eV has been measured for ZnO [2, 3]. As discussed earlier and illustrated in Table 3.1, GGA functionals seriously underestimate the band gap energy. On the other hand, hy-

brid functionals show a significant improvement: band gap energies for both PBE0 (3.142 eV) and PBEsol0 (3.128 eV) are within 10% difference with experimental data. The experimental width of the oxygen 2p band and the energy difference between the Zn 3d and O 2p bands are also better represented by hybrid functionals.

Table 3.2 displays the formation energy for zinc oxide and the cohesive energies with respect to Zn_{metal} and O_2 . Again, the hybrid functionals give better results than GGA for these properties. The PBEsol0 shows the best agreement in these two cases: the deviation of the formation energy for ZnO and the cohesive energy of Zn_{metal} is *ca.* 11% and *ca.* 5% when compared to experimental data, respectively. With respect to the bond energy of O_2 , the experimental value is -5.12 eV. In this case, for the PBE0 functional is -5.188 eV ($\sim 1.3\%$ of difference) and for the PBEsol0 functional is -5.584 eV ($\sim 9\%$). As for the formation and cohesive energies, the GGA functionals failed to reproduce the bond energy of oxygen.

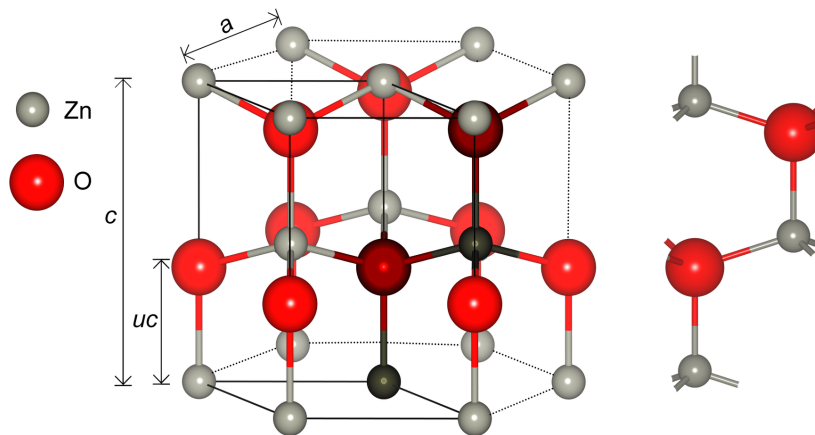


Figure 3.1 ZnO wurtzite structure. The lattice vectors: a and c , and the internal parameter u are shown. The ions in darker colours represent the primitive unit cell, which is shown on the right-hand side. Red is reserved for O and grey for Zn.

Table 3.1 Bulk Properties of the Wurtzite Structure of Zinc Oxide

	References		This Work					
	Shell Model [22]	Experiment ^a	GULP	VASP				
			IP	PBE	PBEsol	PBE0	PBEsol0	PBEsol0 @ 900 eV
ZnO (Wurtzite)								
<i>a</i> (Å)	3.2498	3.2417	3.2518	3.2886	3.2394	3.2579	3.2240	3.2240
<i>c</i> (Å)	5.2029	5.1876	5.1969	5.2994	5.2179	5.2321	5.1771	5.1771
<i>u</i>	0.38025	0.3819	0.3806	0.3797	0.3797	0.3809	0.3808	0.3808
Band-gap (eV)		3.44		0.7340	0.7	3.1420	3.1280	3.1280
W (eV) ^b				3.7880	3.9280	4.4340	4.5350	4.5420
E(d-p) (eV) ^c				3.9880	4.0150	5.0750	5.0680	5.0680

^aExperimental values taken from the lowest available temperature, neutron single crystal diffractometry at 20 K [23].

^bWidth of the oxygen 2p band.

^cEnergy difference between Zn 3d and O 2p bands.

Table 3.2 Formation and Cohesive Energies.^a

Functional	Formation Energy (ΔH_f)		Cohesive/Bond Energy (ΔH_f)			
	ZnO		Zn _{metal}		O ₂	
	eV	kJ/mol	eV	kJ/mol	eV	kJ/mol
PBE	-2.892	-279.118	-1.101	-106.263	-6.591	-636.020
PBEsol	-2.990	-288.577	-1.576	-152.058	-6.986	-674.167
PBE0	-3.167	-305.594	-1.151	-111.077	-5.188	-500.688
PBEsol0	-3.282	-316.741	-1.472	-142.089	-5.584	-538.896
Exp.[56]	-3.700	-357.050	-1.400	-135.100	-5.120	-494.080

^a The values reported in this table correspond to a cut-off energy of 700 eV. Experimental enthalpies of formation were used as comparison.

3.4 Non-polar Surfaces of ZnO

In this section, we report a detailed theoretical study on the structure and electronic properties of the two main nonpolar wurtzite ZnO surfaces, the (10 $\bar{1}$ 0) and the (11 $\bar{2}$ 0). The topics studied are as follows: a brief introduction to the crystal growth, the atomic structure and stability of the clean surfaces and morphological features (steps and grooves), and the effect of such surfaces on the ionisation potential and surface band bending.

3.4.1 Crystal Growth

Experiments have reported that the ZnO nonpolar surfaces have a high density of defect sites (vacancies), steps and more complex morphological features [57, 58]. These findings are supported by atomistic calculations [55] that reported an energetically inexpensive creation of vacancies, steps and non-flat ZnO surfaces. Therefore, it is expected that, under strain, ZnO surfaces show a certain degree of roughness.

Experimentally, cleaving crystals is one of the most widely used methods to create a surface. Despite the efforts to manufacture high quality large single crystals with well defined crystalline surfaces, ZnO-cleaved crystals suffer from strain and external forces that may affect the crystallinity and flatness of the surfaces; as a result, experimental techniques concerning the production of crystalline zinc ox-

ide surfaces have developed new methods. Epitaxial growth procedures have been shown to produce highly crystalline surfaces [19, 20, 59–64] and are now widely used in surface studies. One of the complications of this technique is that ZnO crystals usually grow along the polar hexagonal direction leaving polar surfaces exposed at the top and bottom of the film. These structures can diminish the emission efficiency of the nonpolar surfaces, therefore, choosing an appropriate substrate (such as Al_2O_3) [19, 60, 62–65] that helps the growth of ZnO crystals along the nonpolar directions is necessary to expose surfaces of interest. However, one very common problem is the lattice mismatch between the substrate and the epitaxial film. With a large mismatch, a very large strain energy may build up in the epilayer, thus, creating a series of different defects. These defects show detrimental effects on the optical and electronic properties of ZnO films; however, crystalline growth of zinc oxide nonpolar epitaxial films has been successfully accomplished recently [18–20, 59, 60, 62–66].

3.4.2 Surface Structure

Clean $(10\bar{1}0)$ ZnO Surface

Structurally (see Figure 3.2), the $(10\bar{1}0)$ ZnO surface has been studied very extensively using theoretical and experimental approaches; however, the surface termination remains controversial. While, computational reports have calculated an uppermost zinc relaxation towards the bulk of between 0.15 and 0.57 Å [55, 67–75], experiments estimate a range from 0.06 to 0.45 Å [58, 76–78]. Among the different surface structures proposed are: (a) terraces showing no strong atomic relaxation [58, 79]; (b) terrace structures with strong inward oxygen relaxation leaving the cation lying at the surface [58, 80]; (c) terraces with pronounced Zn relaxations towards the bulk, which also results in a shortening of the corresponding topmost Zn-O bonds [55, 67–69, 71–78, 81]; and (d) highly defective surfaces with vacancies and steps [55, 58, 82]. As mentioned earlier, steps and terraces are very common features of the $(10\bar{1}0)$ surface. Experimental work [58, 82] has shown the presence of steps and partial occupation (attributed to the presence of vacancies) of the first two surface atomic layers, with “occupancies” of 0.77 ± 0.02 and 0.90 ± 0.04 (the

value from 0 to 1 giving the probability of site occupation), in the first and second layers respectively. These defective features have been supported by calculations where it has been reported that the energy cost for creating these steps and broadening the terraces was low [55].

Table 3.3 shows ours and previously calculated as measured atomic displacements of the first two layers of the $(10\bar{1}0)$ surface. Atomic movements in deeper layers are negligible. In general, the same pattern was observed for the GGA and hybrid functionals. In the first layer, Zn atoms show strong relaxation inwards and a displacement parallel to the surface (y direction); O ions remain almost in bulk positions, with just small relaxations away from the surface. From the second layer, both ions relax towards the surface: the O relaxation is very small, whereas that of Zn is more substantial. These results show a good agreement with the low-energy electron scattering (LEED) measurements of Duke et al. [77], which predicted a movement of the top-layer Zn towards the bulk of $-0.45 \pm 0.1 \text{ \AA}$ and similarly a displacement of the uppermost oxygen by $0.1 \pm 0.2 \text{ \AA}$ towards the surface; moreover, high-resolution transmission electron microscopy (HRTEM) images by Ding and Wang [78] showed the same structure. Angle-resolved photoemission spectroscopy (ARPES) studies of Göpel [76] also showed this strong Zn relaxation by -0.40 \AA . There is also good agreement when our results are compared with previous theoretical studies [55, 68, 71, 72, 75]: and there is a general consensus that topmost zinc ions relax inwards by or by greater than -0.21 \AA and with a parallel displacement (y direction) of *ca* 0.16 \AA , towards the O; second-layer zinc atoms relax by (or greater than) 0.132 \AA away from the bulk. We also noted small relaxations of first and second layer oxygen atoms away from the surface.

Clean $(11\bar{2}0)$ ZnO Surface

The $(11\bar{2}0)$ surface has been so far characterised in much less detail, with pertinent structural results regarding this surface being controversial. Experimental LEED analyses [83] on annealed $(11\bar{2}0)$ surfaces show that the surface structure is bulk-terminated within the accuracy of the measurements [13]. In agreement with the previous LEED analysis, early *ab initio* studies by Wander et al. [84] and the tight -

Table 3.3 Atomic Relaxations of the First Two Layers of the Non-Polar (10 $\bar{1}$ 0) Surface.
a

	Zn _{1z}	O _{1z}	Zn _{2z}	O _{2z}	Zn _{1y}	Zn ₁ -O ₁	ω (deg) ^b
PBE	-0.324	0.015	0.141	0.011	0.168	1.870	10.42
PBESol	-0.335	0.031	0.141	0.001	0.169	1.848	11.39
PBE0	-0.290	0.004	0.132	0.016	0.154	1.852	9.11
PBESol0	-0.217	0.086	0.205	0.081	0.176	1.837	9.30
LEED[77]	-0.45 ± 0.1	0.05 ± 0.1			0.1 ± 0.2	2.010 ^c	11.5 ± 5
ARPES[76]	-0.400						
GIXD[58] ^e	-0.06 ± 0.02	-0.12 ± 0.06	0.000	0.000	-0.05	1.90 ± 0.06	-1.8 ± 2.3
TB[79]	almost bulk-like						
TB[74]	-0.570		-0.055				17.2 ^c
IP[80]	-0.220	-0.260	0.080	0.100	0.090	1.76	
IP[55]	-0.250	0.036	0.165	0.007	0.156		
HF[70]							2.31
HF-corr[70]							2.48
HF[67]	-0.147	0.000	-0.103	0.000	0.000	2.007	1.52
B3LYP[67]	-0.171	0.000	-0.094	0.000	0.000	2.006	2.74
LDA[81]	-0.320	-0.200	-0.020	-0.010			3.60
LDA[69]	-0.500	-0.130	-0.09	-0.090			11.70
LDA[72]	-0.360	-0.040			0.180		10.70
PBE[72]	-0.360	-0.040			0.180		10.10
LDA[68]	-0.330	-0.050			0.1716 ^d	1.830	8.80 ^d
B3LYP[73]	-0.255	-0.083	0.086	-0.003	0.000	1.905	5.20
B3LYP[71]	-0.210	0.002	0.135	0.042	0.116	1.861	6.55
PW91[75]	-0.210	0.100					9.56

^a The nomenclature used in this table is shown in Figure 3.2. Subindexes represent the layer and the direction of the relaxation. All relaxations and distances are given in Å.

^b Zn-O angle.

^c Taken from Wander et al. [73].

^d Calculated from distances.

^e Grazing incident X-ray diffraction.

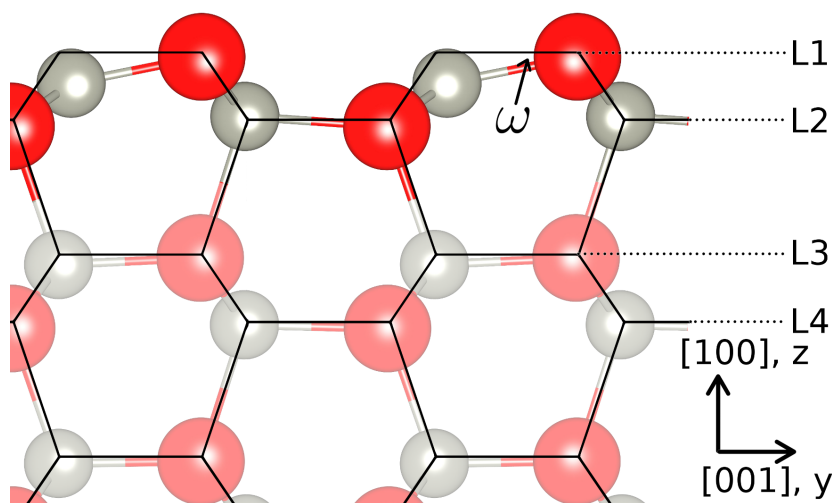
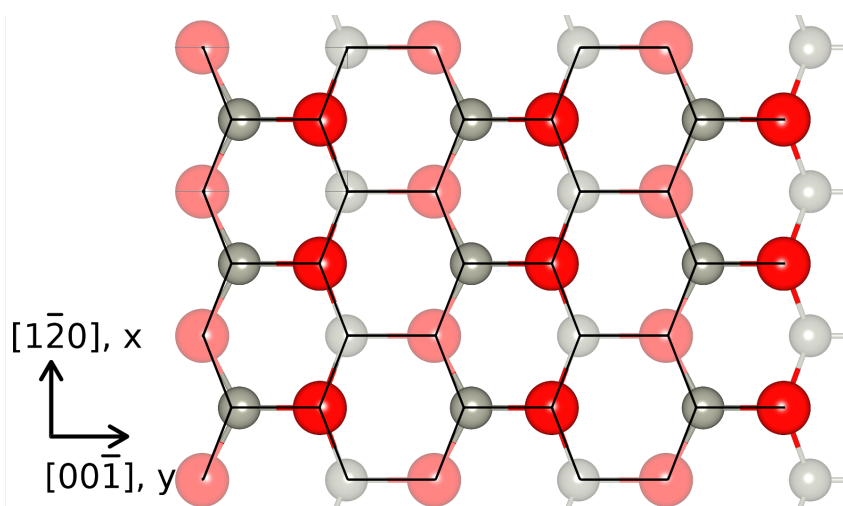
(a) Side view of the $(10\bar{1}0)$ ZnO surface.(b) View along the hexagonal axis of the $(10\bar{1}0)$ ZnO surface.

Figure 3.2 Schematic representation of the relaxed and unrelaxed $(10\bar{1}0)$ ZnO surface. Black lines show the bulk position structure. The stick representation is the relaxed $(10\bar{1}0)$ structure. Only atoms in the first double layer were represented on the top view; darker colours, in (b), were used to represent ions in the first layer. Layers 1, 2, 3 and 4 are represented as L1, L2, L3 and L4, respectively.

binding (TB) model calculations by Ivanov and Pollmann [85] show that the atoms on the $(11\bar{2}0)$ surface remain close to a bulk-terminated position. However, in the former computational study only three degrees of freedom per surface layer were relaxed, which, as noted by Meyer and Marx [72], is only a first approximation. On the other hand, the density functional theory study by Meyer and Marx [72] found that the atomic relaxation on the $(10\bar{1}0)$ and the $(11\bar{2}0)$ surfaces is rather

similar. Finally, as with the $(10\bar{1}0)$ surface, scanning tunneling microscope images by Dulub et al. [57] display a high density of small terraces running along the $\langle 0001 \rangle$ direction and long grooves (*ca.* 250 Å wide and 50 Å deep) along the $\langle 1\bar{1}00 \rangle$ directions. LEED and low-energy ion scattering (LEIS) analysis concluded that the $(11\bar{2}0)$ is the roughest of all the four main low-index ZnO surfaces. To date, despite all the efforts, the $(11\bar{2}0)$ surface remains significantly undercharacterised.

In general, as with the $(10\bar{1}0)$ surface, our calculations show similar behaviour between GGA and hybrid functionals: GGA show larger displacements when compared to hybrid functionals (Table 3.4). We calculated larger inwards Zn relaxations in the $(10\bar{1}0)$ surface; however, movements parallel to the surface are larger (along the x and y axis) for the $(11\bar{2}0)$ surface. The distortion observed for surface ions in this study is in agreement with the roughness seen in LEED and LEIS analysis [57].

The $(11\bar{2}0)$ surface was calculated to be an anion terminated surface where oxygen ions remain, as in $(10\bar{1}0)$, almost in their bulk positions; uppermost zinc shows strong relaxations along all three crystallographic directions. As with the $(10\bar{1}0)$ surface, ions in deeper layers remain almost in bulk positions. Table 3.4 gives ours and earlier calculated atomic displacement of the first two layers of the $(11\bar{2}0)$ along the three cartesian directions. Our relaxations are in good agreement with previous theoretical work produced using interatomic potential methods by Nyberg et al. [80], and with the *ab initio* studies of Meyer and Marx [72] and Marana et al. [71]. As in the $(10\bar{1}0)$ surface, topmost Zn moves towards the bulk (by -0.190 to -0.229 Å). In this surface, zinc also shows considerable displacement along both directions parallel to the surface. In the y direction, towards the oxygen atom, relaxations are from -0.199 to -0.233 Å; and in x from -0.095 to -0.124 Å. Additionally, Zn-O distances were calculated to allow comparison with the extensive study on ZnO surfaces made by Meyer and Marx [72]. The atomic structure of the $(11\bar{2}0)$ surface is displayed in Figure 3.3.

3.4.3 Stability of the Clean Non-polar Surfaces of ZnO

Table 3.5 shows the calculated surface energy for the nonpolar $(10\bar{1}0)$ and $(11\bar{2}0)$ surfaces. In agreement with previous theoretical work, it was found that the $(10\bar{1}0)$

Table 3.4 Atomic Relaxations of the First Two Layers of the Non-Polar (11 $\bar{2}$ 0) Surface.^a

	PBE	PBEsol	PBE0	PBEsol0	B3LYP [71]	PW91 [75]	TB [74]	IP [80]	LDA [72]	PBE [72]
Zn _{1x}	-0.121	-0.124	-0.095	-0.103	0.085					
Zn _{1y}	-0.228	-0.233	-0.199	-0.201	-0.156			-0.14		
Zn _{1z}	-0.223	-0.229	-0.217	-0.190	-0.093	-0.14	-0.540	-0.15		
Zn _{2x}	0.023	0.023	0.028	0.022	-0.017					
Zn _{2y}	-0.035	-0.036	-0.030	-0.031	-0.025					
Zn _{2z}	0.075	0.073	0.048	0.074	0.117	0.095				
O _{1x}	0.038	0.031	0.053	0.041	-0.041					
O _{1y}	0.036	0.048	0.022	0.030	0.010			-0.17		
O _{1z}	0.029	0.040	-0.007	0.028	0.064	0.10		-0.17		
O _{2x}	0.025	0.025	0.032	0.026	-0.020					
O _{2y}	0.021	0.023	0.016	0.019	0.018					
O _{2z}	0.022	0.019	0.005	0.030	0.075					
Zn ₁ -O ₁	1.901	1.878	1.882	1.866	1.877					
Zn ₁ -O _{1'}	1.887	1.865	1.869	1.855	1.893					
Zn ₂ -O ₂	1.991	1.962	1.971	1.952	1.986					
Zn ₂ -O _{2'}	2.010	1.979	1.989	1.969	1.974					
Zn ₁ -O ₂	1.971	1.937	1.948	1.930	1.954					
Δ_{1z}	0.253	0.269	0.210	0.218			0.540		0.243	0.240
Δ_{2z}	-0.053	-0.054	-0.044	-0.044			0.095		-0.051	-0.049
Bulk					0.0					
Δ_{1y}	3.458	3.405	3.388	3.350			3.388		3.359	3.448
Δ_{2y}	3.301	3.251	3.244	3.209					3.217	3.292
Bulk					(1-u)c					
Δ_{1x}	0.264	0.281	0.221	0.231			0.399		0.265	0.407
Δ_{2x}	0.056	0.059	0.046	0.050					0.063	0.085
Bulk					0.0					

^a The nomenclature used in this table is shown in Figure 3.3. “Bulk” rows represent values for the unrelaxed surface. All relaxations and distances are given in Å.

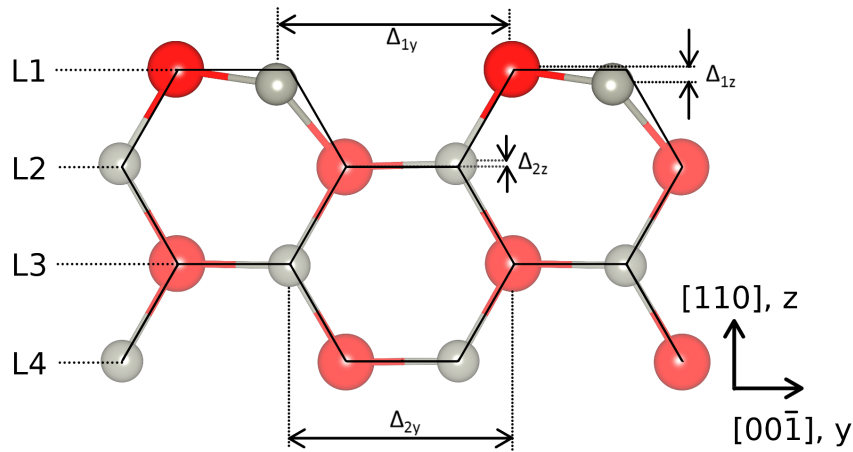
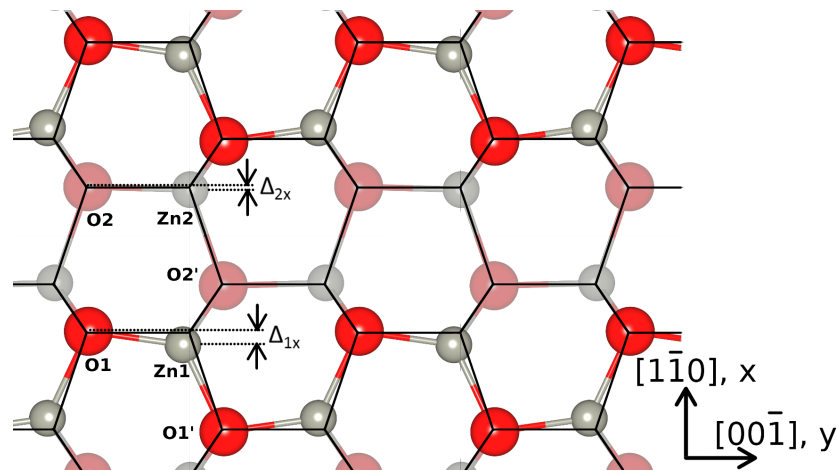
(a) Side view of the $(11\bar{2}0)$ ZnO surface(b) View along the hexagonal axis of the $(11\bar{2}0)$ ZnO surface.

Figure 3.3 Schematic representation of the relaxed and unrelaxed $(11\bar{2}0)$ ZnO surface. Black lines show the bulk position structure. The ball-and-stick representation is the relaxed $(11\bar{2}0)$ structure. Darker colours were used to represent ions in the first topmost layer. Δ values represent the distance between the selected ions along the specified direction.

surface is more stable for all the DFT functionals used. However, the difference in the surface energy between the two surfaces is small ($0.04 - 0.08 \text{ J/m}^2$), so we infer that under thermodynamic equilibrium these two surfaces will coexist in almost equal proportions.

The surface energy varies according to the functional used. For example, it has been seen that LDA and hybrid B3LYP functionals tend to overestimate surface energies; while the PBE functional underestimates surface energies [72]; PBEsol partially corrects the PBE deficiency and hybrid GGA functionals show more accurate

results [86]. The slightly smaller surface energy of the $(10\bar{1}0)$ might be attributed to the more distorted $(11\bar{2}0)$ surface, as was shown in STM images by Dulub et al. [57]. Using interatomic potential methods we calculated the same surface energy for both surfaces and obtained similar results to our DFT calculations.

The *ab initio* study by Wander and Harrison [84] determined a $(11\bar{2}0)$ surface energy of $2.05 \text{ J}/\text{\AA}^2$, which show a discrepancy with the rest of the work published. In their study, a small slab (seven layers) was used and not all parameters were allowed to relax, which could account for the high calculated surface energy.

Marana et al. [71] calculated a smaller surface energy difference between $(10\bar{1}0)$ and $(11\bar{2}0)$ surfaces than that given by Meyer and Marx [72]. However, Marana et al. [71] compared the surface energy difference of $0.1 \text{ J}/\text{\AA}^2$ with the cleavage energy difference of $0.2 \text{ J}/\text{\AA}^2$ given in Ref. 72. Since the cleavage energy represents double the surface energy, the cleavage energy difference of $0.2 \text{ J}/\text{\AA}^2$ mentioned in Ref. 72 is actually a surface energy difference of $0.1 \text{ J}/\text{\AA}^2$, which is the same value as calculated by Marana [71].

We consider that the surface structures presented in this Thesis are definitive models of the nonpolar surfaces of ZnO, as they have explored the effects of computational parameters in detail and are in agreement with experimental work.

3.4.4 Steps and Vacancies at the $(10\bar{1}0)$ ZnO Surface

Following the experimental results of Jedrecy [58] and of Parker [82] and the interatomic-potential calculations by Whitmore [55], we use IP methods to examine models consistent with a fractional surface site occupancy of 0.75 in the first layer, which has been suggested from experiment. As already seen in Ref. 55, Zn and O vacancies scattered randomly over the surface are less energetically favourable than nearest-neighbour Zn-O dimer vacancies. Therefore, we concentrate on the problem of the location of dimer vacancies; henceforth, the term “vacancy” will denote a dimer vacancy.

We built a one-sided 2D periodic surface model using a two-region approach, which has been widely employed in modelling surface structures for potentials based methods [30, 31]. This approach allows free movement of the ions in the

Table 3.5 Surface Energy, E_{surf} (J/m^2), of the Non-Polar ZnO Surfaces with the Different Functionals and in Comparison with Previous Calculations.

	(10 $\bar{1}$ 0)	(11 $\bar{2}$ 0)
PBE	0.85	0.89
PBEsol	0.99	1.05
PBE0	1.02	1.06
PBEsol0	1.11	1.19
IP ^a	1.00	1.00
LDA[72]	1.15	1.25
PBE[72]	0.80	0.85
LDA[68]	1.19	1.23
PW91[75]	1.04	1.06
B3LYP[71]	1.30	1.40
IP[80]	1.10	1.20
IP[55]	1.00	-
IP[68] ^b	-	1.20

^a using potentials reported by Whitmore [55].

^b using Binks [87] potentials.

region next to the vacuum, whereas the second substrate region is held fixed representing the bulk crystal. The (10 $\bar{1}$ 0)-ZnO surface calculations converged using five layers (20 atoms, ≈ 13 Å thick) in both region one and region two. To simulate 75% occupation of the topmost surface layer, we constructed a 4×4 supercell and removed 4 of the 16 Zn-O dimers in the first layer. We developed an in-house python code to build all possible reconstructions; all different configurations were fully relaxed using the GULP code employing interatomic potentials. We analysed the first five lowest energy structures. Key features of the results are as follows as (see Figure 3.4):

- The lowest energy structure is a line of four vacancies along the [001] direction as was seen in Ref. 55 (structure 1).
- The maximum number of vacancies in the same row along [001] is energetically preferable.

- Connected vacancies have lower energies (see 2-4 structures) than isolated (see structure 5).
- Zigzag patterns (structure 4) and diagonal connections among the vacancies are observed in the lowest energy configurations.
- Two or more vacancies in the same row along the [010] direction are not present in the first ten lowest energy structures.
- The highest energy structure has a line of four vacancies along the [010] direction (structure z).
- Massive reconstructions are seen when vacancies along the [010] direction are created: bonds are elongated along [010] direction (presumably driven by the two rows of differently charged ions); and oppositely charged ions, where the line of four vacancies is created, are bonded. In contrast, the structure is well preserved when vacancies are created in the [001] direction.
- Creating a line of vacancies along the [010] direction leaves undercoordinated second-layer atoms where ions are not in pairs as in structure 1, but form rows of positive (Zn) and negative (O) ions, which may explain the high instability of structure z.

Next, we calculated the vacancy formation energy as a function of vacancy concentration. Comparison of the energies among the different surface structures is possible; however, it only tells us which structure is more stable, but does not provide any information about the stability of the vacancy. The vacancy energy formation per ZnO dimer was calculated by:

$$E_{vac} = \frac{((E_{surface}^{def} + nE_{dimer}) - E_{surface}^{nondef})}{n}, \quad (3.1)$$

where $E_{surface}^{def}$ is the energy of the defective surface, n is the number of dimer vacancies (4), E_{dimer} is the energy of a ZnO unit in the bulk and $E_{surface}^{nondef}$ is the energy of the nondefective surface. The energy cost per vacancy values in Figure 3.4 are in a very good agreement with previous calculations [55].

The low energy of formation obtained in the IP calculations for the linear defect is suggestive of the ease of a step formation, which is supported by experiment [58, 82] where it has been shown that it is almost impossible to create a $(10\bar{1}0)$ ZnO surface free from steps. Therefore, we decided to make use of IP and *ab initio* methods to calculate the energy needed to create a step along [010] and [001] directions.

We find that vacancies aligning along the [001] direction show high stability. We use GGA/PBEsol calculations to investigate the energetic cost of forming a step along the [010] direction (vacancies aligning along the [001] direction) at the DFT level, as such steps were observed in experiment using grazing incidence X-ray diffraction (GIXD) techniques [58], and along the [001] direction (vacancies aligning along the [010] direction) building two sets of four different supercell models of different sizes: (2×1) , (4×1) , (8×1) and (16×1) ; and (1×2) , (1×4) , (1×8) and (1×16) . With these models, a vacancy will represent a step along the [010] and [001] direction, respectively. Half of the first and second Zn-O dimers were removed from all the structures. Dimers were removed in such a way that dimer vacancies stay together, increasing the size of the step as we increased the size of the supercell (see Figure 3.5). For the larger systems, using 16 unit cells results in a lateral separation of *ca.* 26 Å and *ca.* 44 Å between periodic images of steps along the [010] and [001] direction, respectively. Extrapolating the curve on Figure 3.6, we find that, when in the limit of infinite separation, $E_{step[010]} = 0.029 \text{ eV}/\text{Å}$ (*cf.* 0.027 eV/Å using IP). The calculated $E_{step[010]}$ suggests strongly that steps would be seen even at room temperature (kT at room temperature is equivalent to 0.025 eV).

The energy cost of a step along the [001] direction shown in Figure 3.6 does not seem to converge and could not be extrapolated to the limit of infinite step separation. However, we find that, where the size of the slab is (1×16) , the step energy is about nine times greater than that of creating a step along the [010] direction. The high energy cost per step along the [001] direction is as a result of exposing charged atomic rows on each side of the step, creating a strong electric field, which

is highly unstable without any major atomic reconstruction, as seen in polar (0001) and (000 $\bar{1}$) ZnO surfaces. Steps along the [001] direction show strong displacements with respect to bulk positions and will not be discussed further due to its high instability.

Atomic Relaxation Close to a Step Along [010] Direction

We now summarise the most notable structural features of the (10 $\bar{1}$ 0) ZnO surface with a step in the [010] direction (see Figure 3.5). In general, we observed larger relaxations for Zn than for O atoms. For the first layer, a strong average Zn relaxation of 0.312 Å towards the bulk and 0.155 Å along the [00 $\bar{1}$] direction is calculated (similar to the relaxation on a clean (10 $\bar{1}$ 0) surface, summarised in Table 3.3). Moreover we find a relaxation of 0.116 Å outwards from the step only for the Zn ions that are on the edge of the step (denoted as Zn_[1*], where the number refers to the layer and the “*” indicates an ion in the edge of the step), while smaller relaxations are seen in this direction for the rest of Zn atoms. The maximum displacement of 0.063 Å (with an average of 0.036 Å) is observed for O_[1*] away from the bulk; the relaxations are less pronounced in the other two directions. For the remaining O atoms there are no significant relaxations.

For the second layer, Zn_[2*] atoms showed the strongest relaxations of 0.292 Å, 0.115 Å and 0.105 Å towards the step, in the [00 $\bar{1}$] direction and inwards, respectively. The rest of the Zn_[2] ions behave in a completely different way with an average strong relaxation of 0.143 Å outwards and smaller relaxations along the other two directions. Again, the O_[2] ions show smaller relaxations.

The atoms in the third layer are divided into two sets: atoms with reduced coordination number (*e.g.* Zn_[3-], where the minus sign indicates the reduction in the number of bonds) and full-coordinated atoms (Zn_[3]). As expected, Zn_[3-] atoms show the larger relaxations, whereas the O_[3] atoms remain close to their bulk positions. The Zn_[3-] ions showed an average relaxation of 0.170 Å and 0.320 Å in the [00 $\bar{1}$] direction and towards the bulk, respectively (similar to the relaxations in Zn_[1]). Smaller relaxations were observed for Zn_[3] ions.

The ions in the fourth layer are also divided into two sets: ions below under-

coordinated atoms (*e.g.* $\text{Zn}_{[4\frac{1}{2}]}$) and ions below full-coordinated atoms (*e.g.* $\text{Zn}_{[4]}$). In general, only $\text{Zn}_{[4\frac{1}{2}]}$ atoms relax outwards (0.140 Å) in a similar manner to the $\text{Zn}_{[2]}$ ions, with the only difference being that the $\text{Zn}_{[4*\frac{1}{2}]}$ showed a smaller relaxation (0.045 Å) in the same direction.

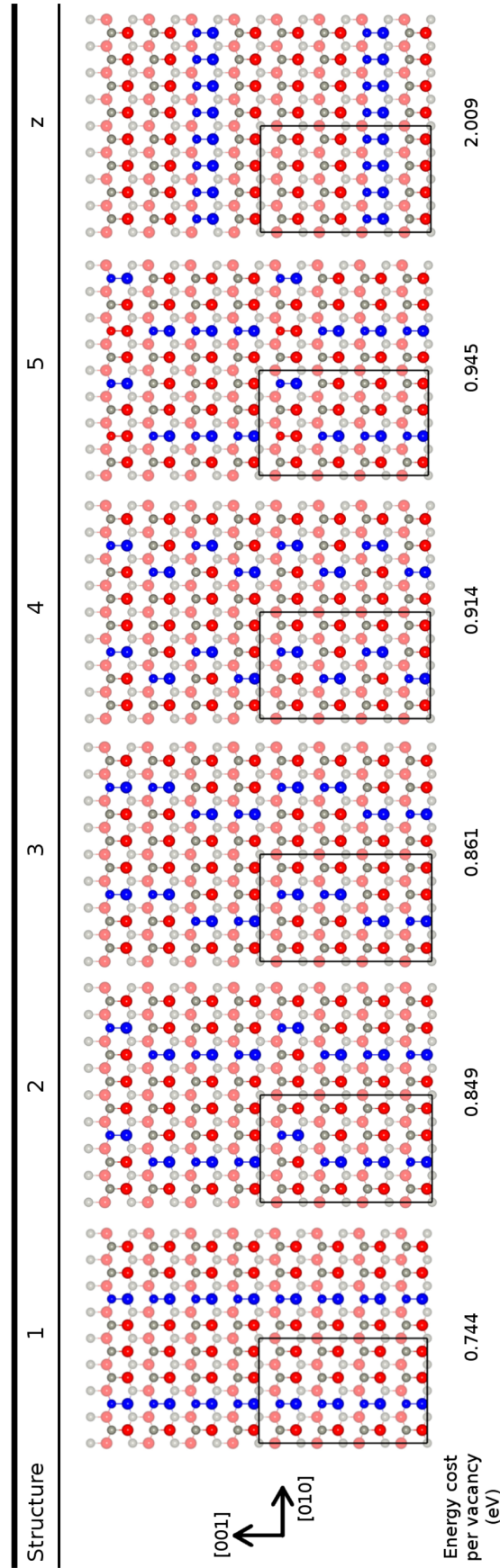


Figure 3.4 Top view of the lowest five (1-5) and highest (z) energy $(10\bar{1}0)$ ZnO structures with 75% first layer occupancy. Energy cost per vacancy is represented below each structure. Red, grey and blue balls represent oxygen, zinc and vacancies, respectively. Darker balls are first layer atoms. The black box represents the 4×4 supercell.

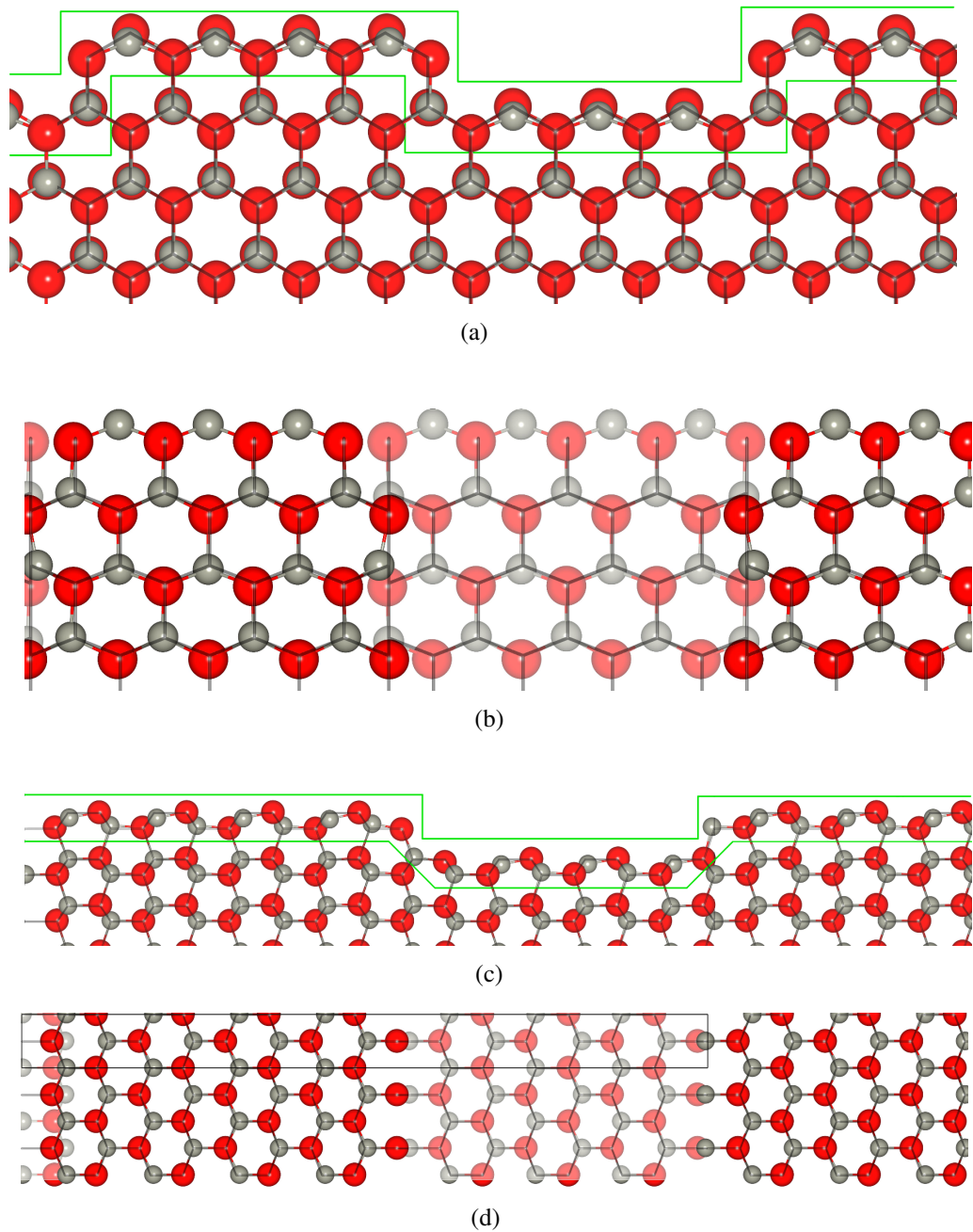


Figure 3.5 Schematic representation of the relaxed and unrelaxed $(10\bar{1}0)$ ZnO surface showing a step along the (a,b) $[010]$ direction and along the (c,d) $[010]$ direction. (a) Side view along the $[001]$ direction of the $(10\bar{1}0)$ ZnO surface, (b) top view along the hexagonal axis of the $(10\bar{1}0)$ ZnO surface, (c) side view along the $[010]$ direction of the $(10\bar{1}0)$ ZnO surface and (d) top view along the hexagonal axis of the $(10\bar{1}0)$ ZnO surface. Black lines show the bulk position structure. Ball and stick representation is the relaxed structure. Only atoms that are in the green region were shown in the top view; darker colours, in (b) and (d), were used to represent uppermost ions.

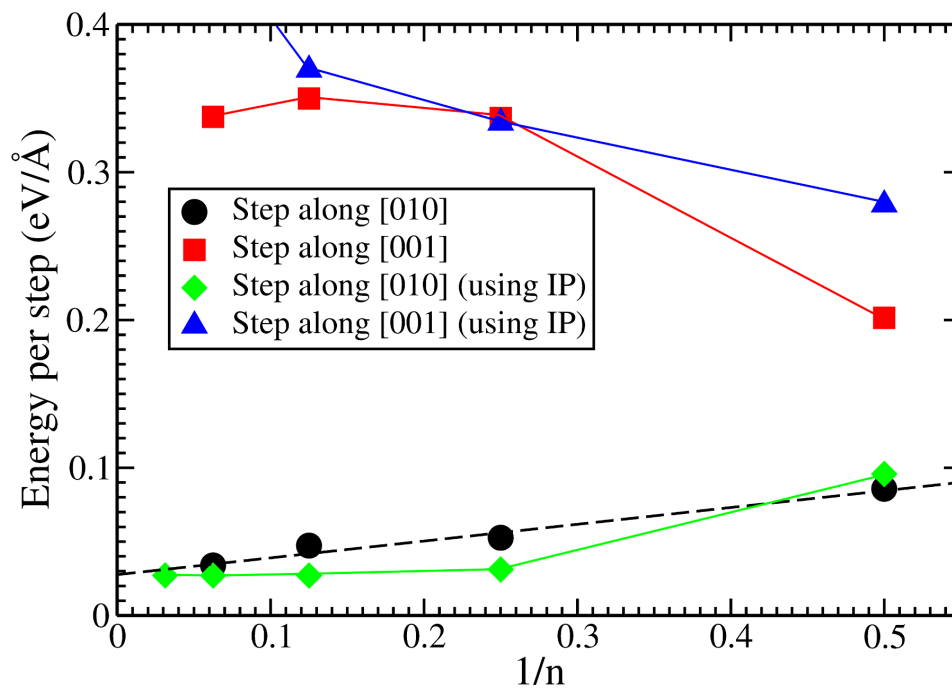


Figure 3.6 Energy of step formation on the $(10\bar{1}0)$ ZnO surface, where n is the size of the supercell along the $[010]$ or $[001]$ direction. The dashed line is a linear fit for the step along the $[010]$ direction.

3.5 Electronic Properties of Non-polar Surfaces

With the ZnO bulk and surface well defined, its electronic properties can be predicted using *ab initio* techniques. A correct positioning of the band edges is vital to calculate a great variety of physicochemical properties such as work function (Φ), ionisation potential (I), electron affinity (A), band gap, among others, which are essential in the design of electronic devices, for example, transparent conducting oxides (TCO). One of the fascinating uses of zinc oxide is as a TCO for electrodes in solar cells, energy efficient low-emissivity windows, flat panel displays, touch screens, light-emitting diodes and architectural glass applications [88–91]. The behaviour of transparent conducting oxides is controlled by the fundamental electronic properties band gap, Fermi level and correct positioning of the valence band maximum (VBM) and conduction band minimum (CBM). To date, various theoretical approaches have been used to calculate the bulk ionisation potential and band alignment; however, each has implicit difficulties [6]. Sokol et al. [92] used a hybrid QM/MM approach to calculate the ZnO bulk ionisation potential (I^b) as 7.71 eV, which is in close agreement with the experimental value reported by Swank [1] (7.82 eV). A recent method developed by Logsdail et al. [6] to calculate I^b (at the plane wave DFT level) showed an agreement with experimental data for a range of different rocksalt ionic oxides using the PBEsol0 functional. This method uses simple polarisable shell-based interatomic potentials to include the surface polarisation effects. At the surface, near to the vacuum, there is a shift in the electronic energies, or the band structure (known as surface band bending) caused by surface polarisation effects, band width and the change of the Madelung potential. Hence, the ionisation potential and electron affinity will differ between the bulk and the surface. In a recent study, Hinuma et al. [93] have calculated the surface ionisation potential (I^s) and electron affinity for the (10 $\bar{1}$ 0) and (11 $\bar{2}$ 0) ZnO surfaces using $GW\Gamma^1@HSE$ (GW approximation with vertex corrections in the screened Coulomb interaction using Heyd-Scuseria-Ernzerhof hybrid functional). They report an I^s value of 8.15 eV (exp. 8.00 eV) [4] and 8.17 eV (exp. 7.82 eV) [1] and an EA value of 4.28 eV (exp. 4.60 eV) [4] and 4.30 eV (exp. 4.38 eV) [1] for (10 $\bar{1}$ 0) and (11 $\bar{2}$ 0)

surfaces, respectively.

3.5.1 Ionisation Potential and Band Alignment

The bulk ionisation potential (I^b) is the energy required to remove an electron from the system. Ideally, we would like to determine this as a “bulk” property, which is independent of the surface termination. When I^b is known, the effect of a particular surface, i.e. the surface band bending, or offset can be determined, yielding the surface ionisation potential, I^s , which is in turn related to a wide range of surface physical/chemical properties. We calculated the ZnO bulk ionisation potential using a recently developed method by Logsdail et al. [6], then determined surface ionisation potential, and finally studied the effect of different surface features (including point defects in the form of dimer vacancies and a line of four vacancies along the [001] direction, grooves and steps) on the ionisation potential.

As noted by Jacobi et al. [4] and Uhlrich et al. [5], the particular surface morphology will affect the positioning of the bands: ideal surfaces result in higher band bending values. The surface treatment given by Swank et al. [1] in the $(11\bar{2}0)$ surface and the extrapolation to time zero after ion bombardment and annealing by Jacobi et al. [4] in the $(10\bar{1}0)$ surface minimised the surface effects on the ionisation potential. Therefore, the values reported there closely correspond to the bulk values.

Bulk and Surface Ionisation Potential

The calculated bulk ionisation potentials (I^b) are reported in Table 3.6. There is a significant improvement in the calculation of the I^b values with the method proposed in Ref. 6: I^b (where “D” makes reference to the multipolar shift) is enhanced by *ca.* 1 eV when compared to the widely-used “band alignment” technique [94]. As mentioned earlier, this method takes into account surface polarisation effects using polarizable-shell based IP. There is neither a significant difference between PBE and PBEsol functionals nor between PBE0 and PBEsol0 (Figure 3.7). Moreover, the calculated $I^{b,D}$ values using hybrid functionals show a good agreement with experiment (7.82 eV) [1] (Figure 3.7), and calculations [92] using a QM/MM approach (7.71 eV). Moreover, this method [6] is shown to be practically surface

independent.¹

Table 3.6 shows that the surface effect on I^s is stronger when hybrid functionals are used. Uhlrich et al. [5] observed an I^s value of 8.1 ± 0.1 eV for dry annealed $(10\bar{1}0)$ crystals, whereas Klein et al. [88] reported a value of 7.7 eV. Hinuma et al. [93] calculated values of 8.15 eV and 8.17 eV for $(10\bar{1}0)$ and $(11\bar{2}0)$ surfaces with $GWT^1@HSE$ calculations while Stevanović et al. [95] calculated 7.53 eV and 7.60 eV using DFT and GW approaches. However, the calculated numbers by Stevanović et al. might have converged to the incorrect value as suggested by Klimeš et al. [96] in their study of about the energy convergence in the GW approximation using the PAW method.

The theoretical values reported for the surface ionisation potential I^s are affected by the method used. Hinuma et al. [93] aligned the CBM by adding the experimental bulk band gaps to the calculated VBM; however, VBM and CBM bend differently, as noted for ZnO in Figure 3.9 and in CdO [97]. The creation of steps and grooves at the $(10\bar{1}0)$ surface has a very small effect on the ionisation potential (a decrease of only *ca.* 0.04 eV), which might be an explanation of the great stability of such features as suggested by this and previous work [55, 58]. However, creating a 25% dimer vacancy at the same surface has a bigger impact on I^s (a decrease of *ca.* 0.13 eV).

We proceed with the calculation of the band gap for the surfaces using hybrid functionals (Figures 3.7 and 3.8). We observed that for the $(10\bar{1}0)$ surface, the band gap is slightly smaller (*ca.* 2.9 eV) than in bulk (*ca.* 3.13 eV); whereas, for the $(11\bar{2}0)$ surface, the band gap is slightly larger (*ca.* 3.2 eV). The latter finding suggests that the thickness of the $(11\bar{2}0)$ surface (15 layers) is not sufficient to represent the band gap correctly. We attribute this overestimation to a quantum confinement effect in a relatively thin slab surface model, which is particularly strong for delocalised conduction states. This behaviour was confirmed using a computationally less expensive GGA/PBESol functional: when the $(11\bar{2}0)$ slab is increased from 15 to 29 layers the band gap decreases from 0.89 eV to 0.77 eV to be compared with

¹Ionisation potential for the surface features was only calculated only at GGA level (PBESol) as the size of the supercells makes hybrids very computationally expensive.

the ideal bulk value of 0.70 eV. The rate of the band gap decrease in these calculations, however, is significantly smaller than that in our hybrid functional calculations and we note, the hybrid functional Gaussian function based study reported in Ref. 71, where no difference between the $(11\bar{2}0)$ surface and bulk band gap values are reported.

To rationalise further the behaviour of the surface band gap, we have separated the band edges as a function of the atomic layers (Figures 3.8 and 3.9). The smaller band gap at the $(10\bar{1}0)$ surface is attributed to the upwards bending of the VBM. With the atomic structure and surface energy converged, the slightly larger band gap for the $(11\bar{2}0)$ surface is caused by the quantum confinement effects: whilst the $(10\bar{1}0)$ surface has 15 *double* layers with a pair of ZnO in each single layer and a slab thickness *ca.* 40 Å, the $(11\bar{2}0)$ surface is composed by 15 layers with two pairs of ZnO on each layer and only half of the $(10\bar{1}0)$ thickness. Therefore, for the $(11\bar{2}0)$ surface there are the same number of ions as for $(10\bar{1}0)$, but the slab has only half the thickness, resulting in a stronger quantum confinement effect on the $(11\bar{2}0)$ surface.

Work Function

The work function (Φ) can be defined as the energy needed to take an electron from the Fermi level to vacuum. A strong emphasis has been made in the determination of this property; however, this property is, like I^s , very sensitive to the sample history, surface preparation procedure, the method of measurement and the facet involved [98, 99]. For example, for the $(10\bar{1}0)$ face, different work function values have been reported by experiment and theory: *ca.* 4.6 eV [1, 4, 5, 100–102], *ca.* 4.3 eV [95, 103–106]. Kuo et al. reported a work function value of 3.74, 3.95 and 4.21 eV for as-deposited ZnO films, after Ar sputter cleaning and after exposure to oxygen plasma [105]. Typically, in intrinsic ZnO, the Fermi level lies just below the CBM. Therefore, the values CBM values reported on Figure 3.7 are comparable to the ZnO work function.

Density of States (DOS)

The shift of the band edges at the nonpolar surfaces across the slab is represented in Figure 3.9. In general, cleaving a nonpolar ZnO surface along the $(10\bar{1}0)$ and $(11\bar{2}0)$ planes results in a local rise of the VBM and CBM energy, respectively. For these calculations, we separated the total DOS into projected DOS per layer. The VBM of the middle layer was set to the corresponding negative I^s value (as this layer represents the bulk). The total DOS for the bulk is shown for comparison and only the hybrid calculations are shown since GGA functionals tend to underestimate severely the band gap. No significant differences were observed when using PBE0 and PBEsol0 functionals. For the $(10\bar{1}0)$ termination, we see a split in the O $2s$ band at the surface due to the lower coordination of the surface atoms. There is also a decrease in the intensity of the Zn d band. For the valence band of the “surface” layer, there is a shift to the VBM of the highest peak, indicating a relative destabilisation of the majority of the valence electrons near the surface, which places their energies close to the VBM. Another important feature is the peak that is seen in the CBM (indicated by a dashed line in Figure 3.9); at the surface, this peak overlaps completely with the adjacent peak.

For the $(11\bar{2}0)$ surface, different behaviour is observed. There is no splitting in the O $2s$ band at the surface. However, there is a displacement of the top of this band. The Zn d band is pushed away from the VBM and the O $2p$ band is concentrated close to the VBM, as in $(10\bar{1}0)$. The band gap shrinks at the surface for both $(10\bar{1}0)$ and $(11\bar{2}0)$ terminations due to the displacement of the top of the VBM; the position of the bottom of the CBM is preserved. The first peak in the conduction band overlaps completely with the adjacent peak, as in $(10\bar{1}0)$.

Table 3.6 ZnO Ionisation Potential. Where I is the Ionisation Potential, “b” Refers to the Bulk, “s” to the Surface and “D” to the New Method Used (Taking into Account Surface Polarisation Effects) [6]. Energies are in eV.

		Bulk ^a		Surface	Step ^b	Groove ^b	25% Dimer Vacancy ^b
		I^b	$I^{b,D}$	I^s	I^s	I^s	I^s
ZnO (10 $\bar{1}$ 0)	PBE	5.49	6.52	6.03			
	PBEsol	5.42	6.42	6.18	6.07	6.08	5.98
	PBE0	6.56	7.58	7.30			
	PBEsol0	6.57	7.58	7.41			
ZnO (11 $\bar{2}$ 0)	PBE	5.46	6.57	6.13			
	PBEsol	5.42	6.51	6.10			
	PBE0	6.52	7.63	7.29			
	PBEsol0	6.53	7.62	7.35			

^a Experimental bulk ionisation potential, $I^b = 7.82$ eV [1].

^b Ionisation potential for the surface features was calculated only at GGA level (PBEsol) as the size of the supercells makes hybrids very computationally expensive.

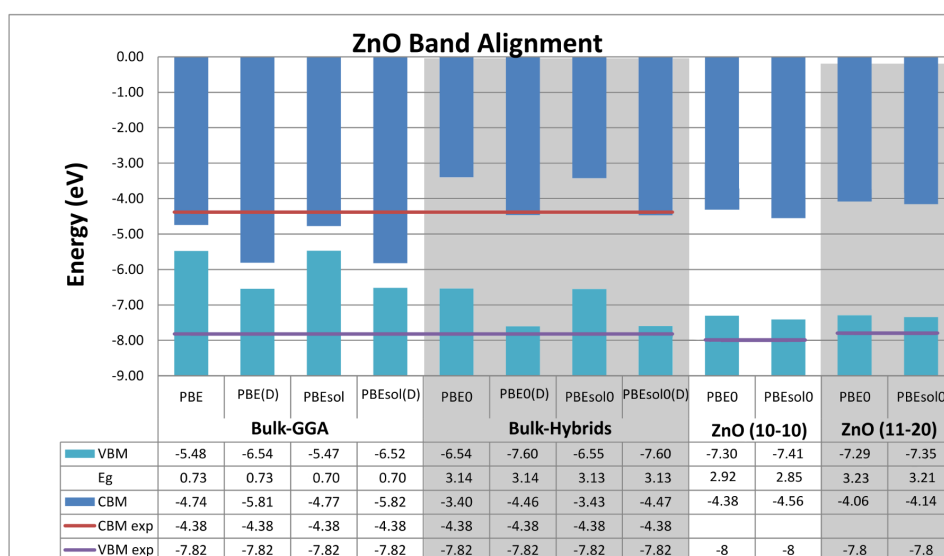


Figure 3.7 ZnO band alignment based on the ionisation potential. The horizontal lines represent the experimental reported values: 7.82 eV for I^b [1] and 3.44 eV for the bulk band gap [2, 3]; for the (10 $\bar{1}$ 0) and (11 $\bar{2}$ 0) a I^s value of 8.00 eV [4, 5] and 7.82 eV [1], respectively. “(D)” [6] has the same meaning as in Table 3.6. The positioning of the CBM bands for the relaxed (10 $\bar{1}$ 0) and (11 $\bar{2}$ 0) surfaces was made by adding the band gap calculated for each relaxed surface presented on Table 3.6 to the VBM value.

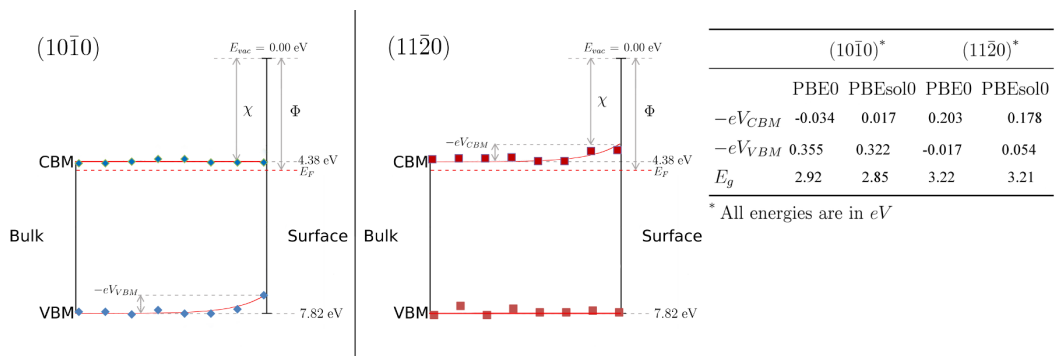


Figure 3.8 ZnO band bending of the CBM and VBM. Bulk values for CBM and VBM were taken from experiment. E_{vac} , $-eV_{CBM}$, $-eV_{VBM}$, E_F , χ and Φ represent the vacuum, band bending at the CBM, band bending at the VBM, the Fermi level, the electron affinity and the work function, respectively. Each diamond/square represents a layer. Values were taken from Figure 3.9.

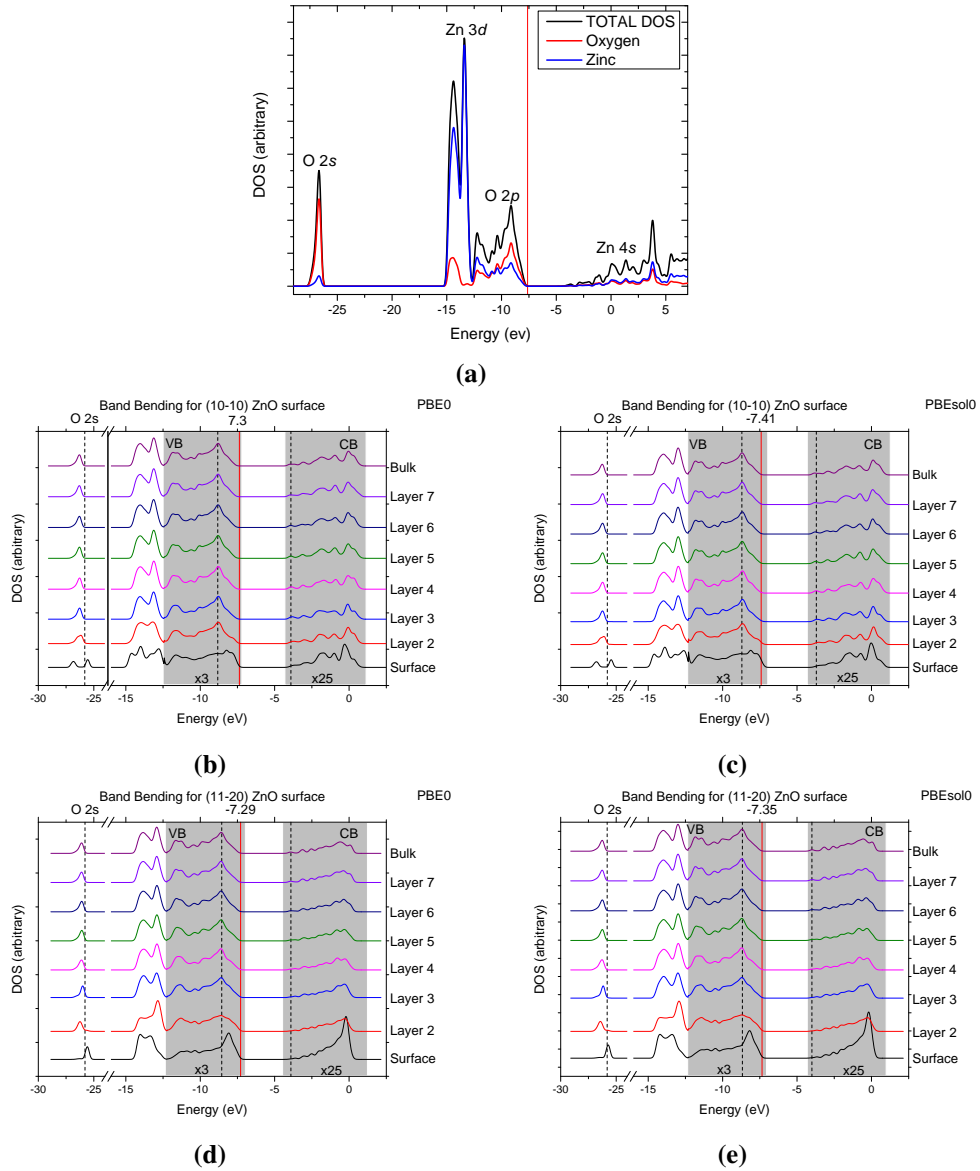


Figure 3.9 (a) Representation of the total density of states for wurtzite ZnO structure using PBEsol0 functional, for comparison see Figure 2 in Ref. 7. Surface band bending across the ZnO surfaces: (b,c) $(10\bar{1}0)$ and (d,e) $(11\bar{2}0)$. Surfaces structures from (b,d) PBE0 and (c,e) PBEsol0 functionals were taken to produce the surface band bending. Layer 1 and 8 are labelled as “Surface” and “Bulk” layers, respectively. The vertical red line represents the top of the valence band. The VB and CB were amplified by a factor of 3 and 25 to make the changes more visible.

3.6 Summary and Conclusions

In this Chapter, the surface structure and electronic properties of the nonpolar $(10\bar{1}0)$ and $(11\bar{2}0)$ ZnO surfaces have been investigated using three different levels of theory: interatomic potentials, density functional theory and using hybrid functionals.

Our hybrid DFT calculations for the clean nonpolar surfaces of ZnO confirm earlier GGA reports of the strong inward cationic relaxation in the topmost atomic layers of the material, although with smaller amplitudes, accompanied by pronounced lateral displacements of cations and anions especially on the $(11\bar{2}0)$ surface.

The calculated surface energies indicate a higher stability of the $(10\bar{1}0)$ surface over the $(11\bar{2}0)$ surface. However, the difference in the surface energy between the two surfaces is small, which implies the importance of thermal vibrational contributions to the free energy, that could determine the crystal morphology under thermodynamic equilibrium or of the kinetic crystal growth factors. However, the $(10\bar{1}0)$ surface is seen predominantly in experiment.

Our calculations provide the first computational rationale for the extensive steping observed on the nonpolar surfaces of ZnO at the *ab initio* level of theory. The energy cost of creating a step along the $[010]$ direction, $E_{step[010]}$, on the $(10\bar{1}0)$ was found to be $0.029 \text{ eV}/\text{\AA}$ (*cf.* $0.027 \text{ eV}/\text{\AA}$ using interatomic potentials). Thus, we expect that steps would be seen even at room temperature ($k_B T \approx 0.025 \text{ eV}$).

The surface structures obtained in this work have been employed to determine the bulk and surface ionisation potentials of ZnO along with the electronic band bending. The calculated bulk ionisation potential values using the method described in Ref. 6 show an improvement of about 1 eV with respect to the widely used “slab alignment” method. For hybrid functionals, I^b is calculated as $\approx 7.6 \text{ eV}$, compared to the experimental value of 7.82 eV. Surface features such as steps and grooves are shown not to have a strong effect on the ionisation potential (a decrease of *ca.* 0.04 eV), whereas a 25% dimer vacancy formation at the surface would decrease the ionisation potential by 0.13 eV.

The surface electronic properties are shown to converge much slower with the slab model thickness. Using hybrid functionals, the band gap at the $(10\bar{1}0)$ surface is still smaller (*ca.* 2.9 eV) than in the bulk (*ca.* 3.13 eV). For the $(11\bar{2}0)$ surface, using a slab of fifteen layers thickness was not enough to represent the band gap correctly, which could be attributed to quantum confinement. It is expected that with a thicker slab, the band gap of the surface will become closer to the bulk band gap, as confirmed by our GGA calculations.

To characterise the band bending we have decomposed the density of states into atomic layer contributions. The two nonpolar surfaces are seen to behave markedly differently with a local rise of the VBM for $(10\bar{1}0)$, whilst remaining nearly flat for $(11\bar{2}0)$. In contrast, the CBM rises for the $(11\bar{2}0)$ surface. Therefore, a band gap closing will be seen on the first surface by 0.31 eV and band gap opening on the second by 0.12 eV. No significant differences were seen between PBE0 and PBEsol0 functionals.

Chapter 4

Polar Surfaces of ZnO

4.1 Introduction

In the previous Chapter, we described in detail the surface structure and electronic properties of the zinc oxide nonpolar surfaces. In this section, we continue with a discussion of the two main low-index polar ZnO surfaces. Cleaving the ZnO crystal along the c axis creates, inevitably, two different polar surfaces: the Zn-terminated (0001) and the O-terminated (000 $\bar{1}$) (Figure 4.1), which present different physical and chemical properties [107]. These polar surfaces are classified as type 3 (Tasker [46]) and are unstable without a major reconstruction.

One of the most puzzling features of ZnO is the stability of its polar surfaces, which is not present in other oxides [13]. Clean polar ZnO surfaces are not stable due to an inherent dipole formed in each unit cell along the c axis. These polar surfaces, however, are present in nature; as a consequence, we must take into account the factors that stabilise these surfaces.

Over the last 40 years, both experimental and theoretical approaches have been applied in order to understand the stability of these surfaces. The particularly strong interest in apprehending the stabilisation mechanism of the ZnO polar surfaces can be attributed to their profitable use in catalysis (methanol synthesis), photocatalysis and hydrogen gas sensitivity [108]. Nowadays, there is a clear industrial need for improving methanol synthesis, which was estimated to be 65 million tonnes worldwide in 2013 [12]. If this can be done cheaply it will have a major impact on

industrial processes and the science of clean energy fuels. Understanding the stabilisation mechanism of these surfaces will help us with their characterisation and synthesis, as well as with the identification of active sites in the Cu/ZnO catalyst.

To date, the stabilisation of the polar ZnO surfaces remains poorly understood. On the zinc terminated face, LEED [109–111] and HAS (Helium atom scattering) [112] studies have shown surfaces with a (1×1) periodicity with no evidence of atomic reconstruction. If no reconstruction is present, a charge transfer between the two terminations must stabilise these surfaces, as suggested by Nosker et al. [113]. The (1×1) periodicity would lead to surface metallic states in both terminations, which is discussed in more detail below. In contrast, the best fitting of a grazing incidence X-ray diffraction (GIXD) study [58, 114] could be obtained when only 75% of the topmost Zn ions are present. This finding was corroborated by one recent STM study on the (0001) ZnO surface, where a large number of steps are seen which form triangular reconstructions of different sizes [57]. For the O terminated face, LEED [101, 110, 115], LEIS [116], GIXD [58, 114, 117], and surface X-ray diffraction [117] have shown a bulk-like (1×1) structure with no atomic reconstruction. Moreover, a (1×3) $(000\bar{1})$ reconstruction with rows of O vacancies along the $[10\bar{1}0]$ direction has been proposed by Wöll [118]. The latter reconstructions are supported by an XPS (X-ray photoelectron spectroscopy) quantitative analysis [119] of the O 1s intensities, where a deficiency of $39 \pm 10\%$ of the topmost O ions in a (1×3) periodicity is suggested. More recently, a small portion of high-resolution STM images [120] show an oxygen terminated face with (5×5) hexagonal-shape reconstructions.

Recent theoretical investigations of polar surfaces of ZnO have been mainly following experimental studies. Early DFT studies have predicted unreconstructed ZnO polar surfaces [72, 117]. On the other hand, a set of *ab initio* studies [113, 121–124] calculated more stable non stoichiometric polar ZnO surfaces. Following experiment, calculations have shown that, on the Zn face, the stabilisation mechanism happens through triangular shaped reconstructions of different sizes [122, 123, 125, 126], whereas on the O terminated side there are hexagonal atomic

reconstructions [120, 124] with a (5×5) periodicity. The calculations involved have, however, been based on limited experimental data, giving only a partial solution to the problem and leaving many experimental findings unexplained.

In this Chapter, we investigate the origin of the stability of polar ZnO surfaces using global search techniques coupled with methods based on interatomic potentials. We report a detailed computational study of the mechanism of surface reconstruction that rationalises their unique behaviour. Our calculations explain the many differing experimental findings [58, 101, 109, 110, 110–120], which seem to be self contradictory, by examining in detail the crystal growth along the polar directions. Firstly, we explain the polar surface problem and we discuss the different stabilisation mechanisms that have been proposed in the literature. Secondly, we introduce the approach we use throughout our study. We then describe the methods and computational details used for this work. Thirdly, we present an analysis on the surface structure and stability of the ZnO polar surfaces obtained from our calculations. Finally, we present a summary of our work and the conclusions which it leads to.

4.2 Stabilisation Mechanisms of Polar Surfaces of ZnO

The instability of the ideally terminated ZnO polar surfaces can be described from two different points of view: the covalent and the ionic. In the covalent picture, there is a loss of 25% in the coordination number ($0.5e$) of the surface atoms, which would result in the appearance of dangling bonds. As ZnO is a polar semiconductor, the Zn terminated face would be expected to show an excess of electrons in the Zn $4s$ conduction band, while at the O terminated face there would be electrons missing (holes) from the O $2p$ valence band. Both dangling bonds and excess charge carriers should be evident from surface metallization, which, however, is not usually observed. Moreover, in the ionic picture, the instability of the ZnO polar surfaces is clearly associated with the charge distribution of the ionic monolayers along the c axis. Assembling such monolayers would produce a dipole moment in the repeat

unit cell normal to the surface [46] (Figure 4.3). Therefore, crystals with unreconstructed polar surfaces would resemble charged capacitors. If the crystal slab is thick enough, the stored energy will result in a dielectric breakdown causing the material to collapse and conduct. The dipole moment is a function of the size of the material: in principle, polar surfaces of very small oxide particles could be stable [118]. In theoretical calculations, the surface energy of these surfaces diverges as the slab size increases.

Three different mechanisms have been proposed to stabilize the ZnO polar surfaces: (i) surface “metallization”, (ii) change of the stoichiometry at the surface (removing/adding Zn/O ions) and (iii) adsorption of H, O and OH ionic species. All three mechanisms involve charge transfer between the two opposing polar surfaces in the ionic picture.

4.2.1 Surface “Metallization”

The “metallization” mechanism has been studied by different groups with *ab initio* techniques [72, 117, 122, 123, 127]. This method arises naturally from the covalent picture, whereas in the ionic description it implies electron transfer from the O face to the Zn. The surface “metallization” is quite common for polar semiconductor surfaces [121]; however, it has not been observed for ZnO polar surfaces using either photo-emission experiments [76, 128] or scanning tunnelling spectroscopy [57], whereas calculations yield high surface energies [46].

4.2.2 Adsorption of Adatoms.

Metal oxide surfaces are usually in contact with some water and its dissociated species. There is experimental and theoretical evidence that the stability of the ZnO polar surfaces can be achieved by adsorption of charged H, O, and OH species, mainly by the creation of stable hydroxylated surfaces [124]. Thus, the excess (at the Zn side) and deficiency (at the O side) of electrons/charge can be compensated by the adsorption of these charged ions.

Earlier B3LYP studies [129] suggested that the adsorption of OH on the Zn face and H on the O face was energetically unfavourable when compared to an *ab*

initio study [117] where metallic surface states are allowed. However, the coverage tested in the *ab initio* study was one monolayer (ML) of OH on the Zn side and one ML of H on the O side, which are not the concentrations needed to neutralise the dipole moment. Whenever OH adsorption is compared to H at the (0001) surface, a more stable OH adsorption is reported [122], the reason being that the adsorption of hydrogen on the Zn side is so reactive (exothermic) that it can reduce ZnO units to metallic Zn, forming OH groups —implying oxygen mass transport close to the surface (for experimental reference, see [112]). Structurally, *ab initio* calculations [122] have reported a bulk-like structure of the (0001) surface in the presence of hydrogen; while OH groups are more stable when adsorbed at interstitial sites, where oxygen atoms are coordinated to three surface Zn atoms.

Another stabilisation alternative is the adsorption of oxygen atoms on the Zn face. The best O adsorption site on the Zn terminated surface was shown to be more stable than the creation of random Zn vacancies on the same surface [122]. Nevertheless, triangular reconstructions are reported to be even more stable than random Zn vacancies or isolated O adatoms [122]. On the other hand, hydroxylated (000 $\bar{1}$) surfaces are stable [124]. However, metal oxide surfaces are strongly passivated by the presence of hydroxyl groups, which is not desirable if high a concentration of active sites is needed.

4.2.3 Vacancies.

Experiment and theory have proposed that the stability of the non stoichiometric polar ZnO surfaces can be attributed to Zn and/or O vacancies [113, 121–124]. For example, the best fit to X-ray diffraction data was obtained in [130] with 25% Zn⁺² vacancies at the Zn-terminated surface, which according to the ionic model is the charge needed to compensate the dipole. On the (0001) ZnO surface, portions of STM images and density functional theory (DFT) calculations have shown that the vacant Zn sites can cluster as triangular shaped reconstructions [122, 123, 125]. Triangular terraces terminated by single-layer steps, *ca.* 2.4 Å in height [57], will be decorated by oxygen. Such reconstructions could be produced by removing the topmost pairs of Zn and O atoms from the surface, as confirmed by Monte Carlo

(MC) simulations using empirical potentials [126]. In general, larger triangles are preferred over smaller triangles [57]. The energetic competition between triangles of different size is, however, found to be very tight, explaining the observed macroscopic roughening of the surface in experiment. These MC calculations showed that triangular reconstructions are even more stable than isolated oxygen adatoms or Zn vacancies at the Zn termination, in agreement with STM measurements [123]. These reconstructions appear to be electrostatically driven and are stable over a wide range of oxygen and hydrogen chemical potentials [123]. In contrast, at the $(000\bar{1})$ surface, honeycomb-like reconstructions are observed occasionally in experiment and are supported by *ab initio* calculations [120, 124]. The difference in reconstructions between the two polar surfaces has been attributed to a higher flexibility of Zn atoms to form bonds than O atoms [124].

Different factors will determine the reconstruction and stabilisation mechanism of the ZnO polar surfaces including synthesis conditions and residuals in the ultra-high vacuum (UHV) chamber used in STM experiments. STM images [57] have shown that at high annealing temperatures, terraces grow wider and triangular pits smaller for the (0001) surface. Whereas at the $(000\bar{1})$ termination, some STM images show partial hexagonal reconstructions [120, 124], with others displaying no clear reconstruction and a (1×1) periodicity [109–112].

4.2.4 Faceting

It is widely reported that small changes in the synthesis conditions may lead to different atomic structures. For example, Zheng et al. [131] have proposed an alternative stabilisation method for the (0001) ZnO structure. According to their STM images, depending on preparative conditions, the (0001) surface consists of either triangular islands and pits of different sizes or the formation of facets of high step density with $(10\bar{1}4)$ surface orientation. We note that these structures are created after annealing at ≈ 850 °C: the use of high annealing temperatures (> 700 °C) causes roughening. Facets were already suggested by Nosker et al. [113], which according to their study yields a lower surface energy.

Wherever the polar ZnO surface properties are to be exploited, the presence of

high step density with another surface orientation might not be beneficial. The use of lower annealing temperatures (< 700 °C) or the growth of ZnO polar epitaxial layers may avoid surfaces with a high density of steps.

4.3 Methods and Computational Details

4.3.1 Strategy

One of our main interests is the study of the catalytic Cu/ZnO system. Therefore, we focus our efforts on clean ZnO polar surfaces, which show a higher catalytic activity than those surfaces compensated with OH groups.

In view of the complexity of the chemistry of polar ZnO surfaces, here we investigate the origin of the stability of polar ZnO surfaces using unbiased global search techniques on the energy landscape defined by highly accurate interatomic potentials [55]. A two-dimensional (2D) periodic surface supercell model is used throughout. A top layer vacancy concentration of 25% has been suggested [57, 122, 123, 126] to compensate the inherent dipole; however, this percentage would only be correct if there were no polarisation. We used interatomic potential (IP) based methods with a polarisable shell model [55] to calculate the Zn/O vacancy ratio needed to minimise the dipole. First, bulk ZnO was optimised and cleaved along the c axis, creating both the (0001) and the (000 $\bar{1}$) surfaces. Second, we calculated the dipole produced for the three charged atomic layers (Zn, O core and O shell). Finally, we calculated the charge compensation needed to reduce the dipole to a minimum value. This compensation is done through an ionic transfer between opposing polar sides (Figure 4.1).

The Zn/O vacancy ratio was calculated as follows. The dipole moment of the unreconstructed surface is given by:

$$P = [q_{Zn}(j) + q_{Oc}(u_c - k_c) + q_{Os}(u_s - u_c)]cNz, \quad (4.1)$$

while the dipole produced by the ion transfer is:

$$P_{counter} = [-m_{Zn}q_{Zn} - m_O(q_{Oc} + q_{Os})]cN \quad (4.2)$$

and the condition of nonpolarity, dipole = 0:

$$P - P_{counter} = 0 \quad (4.3)$$

where q_{Zn} , q_{Oc} and q_{Os} are the charges of Zn, O core and O shell, respectively. k and u are the fractional distances described in Figure 4.1, and $j = k + u$. N , m , c and z are the number of unit cells, the number of ions to be transferred, the lattice parameter c and number of surface atoms. Sub-indices are used for core and shell units.

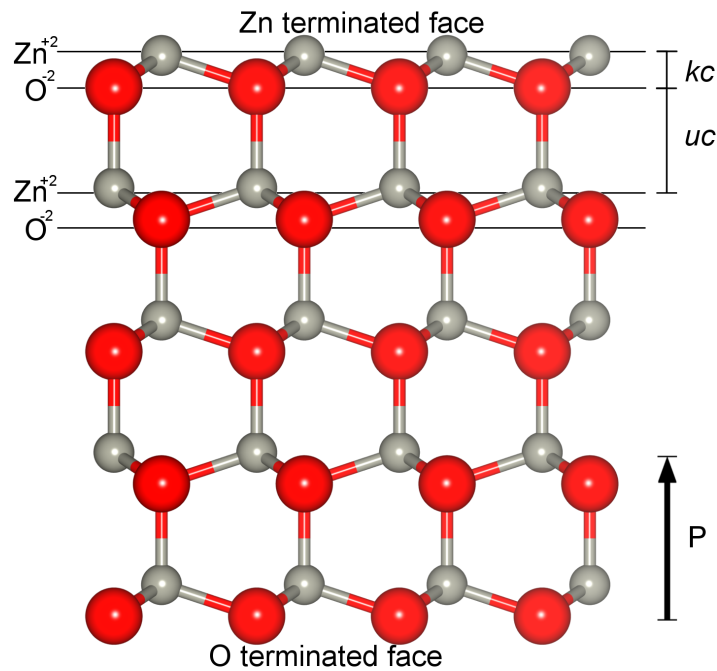


Figure 4.1 ZnO polar surface. The internal parameter u and the fractional distance k are shown. Red colour is reserved for O and grey for Zn.

From Equations (4.1), (4.2) and (4.3), the ionic transfer needed to minimise the dipole depends on two parameters: the ionic charge of all species and on the distances between charged layers in c direction. By solving (4.3), we calculated the optimum number of vacancies being at $|m_{Zn} - m_O|/25 = 0.240988$ (ca. 24%; this ratio has been already proposed by [120, 124]) — using both: the potentials reported in Ref. 55 and the IP atomic structure given by our previous calculations [86].

Another important variable in the reconstructions of the surfaces is their size.

This variable constrains the size of the reconstruction patterns and the lowest dipole that can be achieved. Figure 4.2 shows the smaller possible dipole values for a range from 1 to 400 unit cells and the inset only shows the data points where the dipole is improved with respect to the previous data point. Three interesting cells sizes are shown in the inset: (2×2) , (5×5) and (19×19) . The first data point, (2×2) , is too small for our purposes, e.g. does not allow many different reconstructions, and its dipole is *ca.* 50% stronger than the (5×5) cell size. The second data point, (5×5) , produces a reasonable low dipole and is supported by STM images [9, 120]. The last data point, (19×19) , gives the lowest dipole from all the 3 data points; however, this size is very computationally expensive — calculations *ca.* 3000 times slower than the (5×5) size. In conclusion, the (5×5) supercell gives a good balance between size and the magnitude of the dipole. Attempts to reduce the dipole to a value of $10^{-6}e\text{\AA}$ would require a computationally infeasible (1000×1000) cell size.

However, our approach raises another interesting question: what is the structural and energetic influence of a very weak dipole? We studied this problem by creating an artificial dipole of the same magnitude and opposite direction as the one that remains in the surface after the ionic transfer as illustrated in Figure 4.3. The artificial dipole is generated by a set of point charges (pc) distributed over the surface (Figure 4.3); a more detailed description of this approach is given below.

4.3.2 Polar ZnO Surface Models

We have used an atomistic approach as implemented in the interatomic potential (IP) code GULP (General Utility Lattice Program) [30, 31]. The use of IP allowed us to optimise a vast number of structures generated by our in-house global optimisation code, the Knowledge Led Master Code (KLMC) [50, 51] (introduced in Chapter 2), and identify the lowest energy configurations.

The surface structures were built and optimised by KLMC and GULP, respectively. We used the Born, shell model potentials for ZnO developed by Whitmore, Sokol and Catlow, which show excellent agreement with a range of experimental data (see Table 1 in Ref. [55]), as with of calculations.

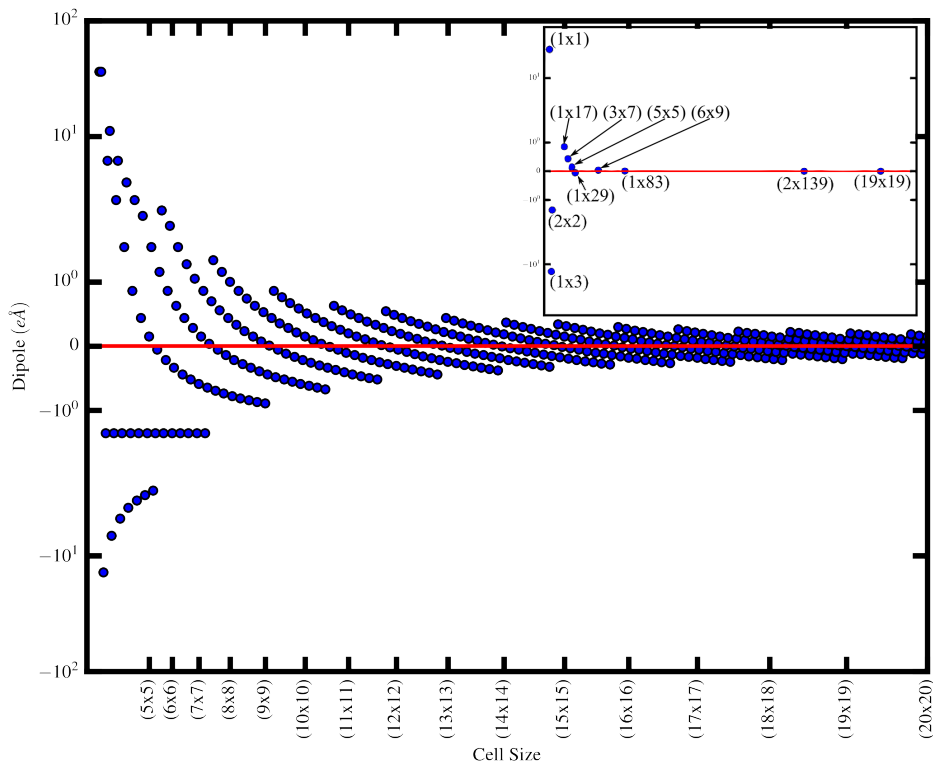


Figure 4.2 Lowest dipole possible using entire ionic transfer from a range of 1 to 400 supercell size. Inset: only points that reduce the dipole while increasing the cell size shown.

The bulk structural parameters used were $a = 3.2518$, $c = 5.1969$ and $u = 0.3806$ as calculated in our recent publication [86]. The dipole compensation was performed by removing Zn and/or O atoms from the surface and spreading compensating charge uniformly over the slab bottom. As discussed above, the optimum configuration is a (5×5) supercell with a ratio of $|m_{\text{Zn}} - m_{\text{O}}|/25 \approx 0.24$, e.g. having 6 Zn vacancies (V_{Zn}) produces a similar dipole to that for 13 V_{Zn} and 7 O vacancies (V_{O}). We employ a one-sided 2D-periodic surface model using a two region approach which has been widely employed in modelling surface structures with interatomic potential based methods. Our models consist of 6 layers thick in the c direction (250 atoms, *ca.* 15 Å), the top 3 atomic layers were allowed to relax (region 1), whereas the bottom 3 were held fixed representing the bulk crystal (region 2). The bottom layer (6th layer) was used to spread compensating charge uniformly (Figure 4.3). The lowest energy structures were tested with a slab twice as big as the one implemented in our calculations; no significant structural changes were

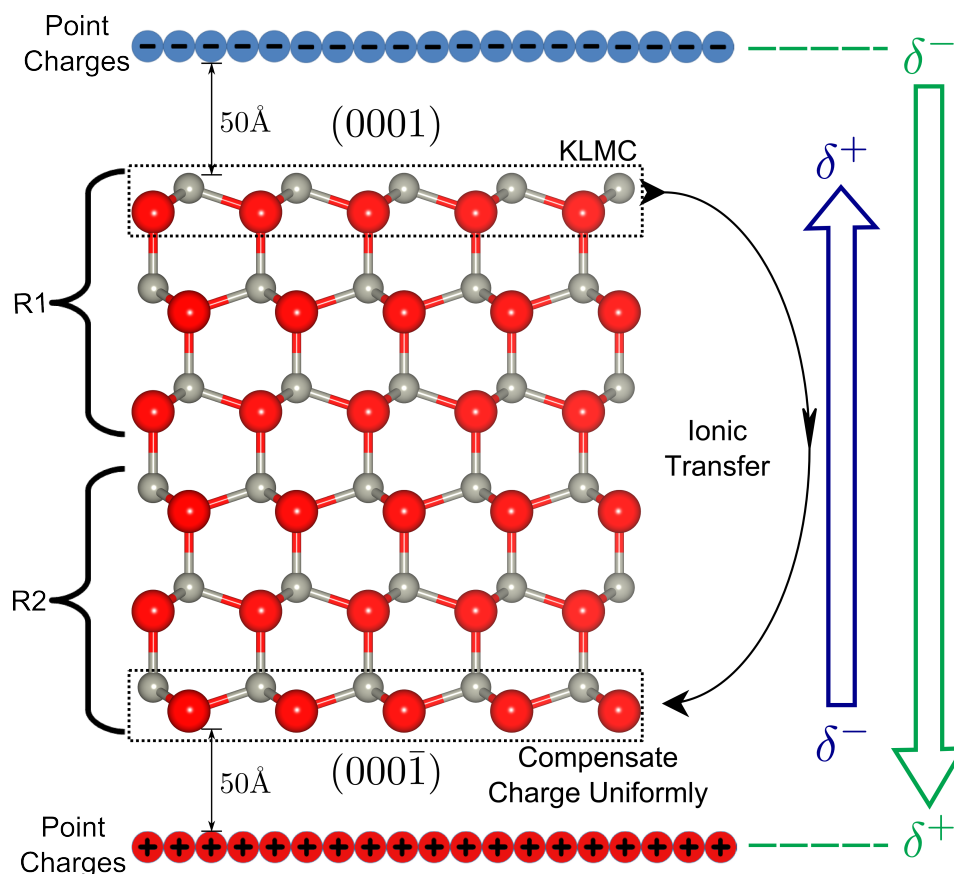


Figure 4.3 ZnO polar surface. A dipole-corrected one-sided model of the Zn-terminated polar surface of ZnO. A two-region setup is used in our calculations with region one, R1, allowed to relax, and region two, R2, held fixed. The residual surface dipole is compensated by the opposite and equal in magnitude dipole due to two planes of point charges: placed outside of the surface slab at a large distance. In this paper, red colour is reserved for O and grey for Zn.

observed and the difference in the average surface energy is only by -0.1 J/m^2 .

As discussed earlier, after ionic transfer there is a weak remaining dipole. The latter was completely cancelled by the creation of one point charge layer on each side of the slab, which contained 100 points that were distributed over the surface. The point charges were situated *ca.* 50 \AA from the surface to avoid any interactions with the topmost atoms (Figure 4.3). The same approach was used to model both zinc and oxygen terminations.

We used Monte Carlo routines as implemented in KLMC for the surface structure global optimisation of ZnO polar surfaces. The top layer was made of a grid with Zn and O bulk lattice positions where the number of V_{Zn} and V_O was specified

and KLMC created the surface structures by swapping the vacancies among the grid positions. Two restrictions were specified: KLMC restricted anions from swapping with cations and vacancies were only allowed to occupy bulk lattice positions of the top layer. For each structure created, KLMC called GULP to perform a structure optimisation using the BFGS algorithm.

We tested all the Zn/O (and O/Zn) possible ratios in a (5×5) supercell: a total of 26 different stoichiometries for each surface termination. The global search using Monte Carlo routines as implemented in KLMC probed more than 10,000 different reconstructions for each stoichiometry — more than 500,000 different structures in total. The need to analyse the whole range of Zn/O stoichiometries arises from the fact that the concentration of Zn and O ions on each surface depends strongly on the sample preparation conditions, including temperature, annealing time, sputtering time and energy [57].

4.3.3 Surface Energy Calculation

Since the number of ions at the top and bottom layers is different for each stoichiometry, an energetic comparison across stoichiometries cannot be made using total but surface energies. The surface energy (E_{surf}) of a material is the energy per unit area required to create a surface and is associated with the stability of the surfaces. Given a bulk energy containing the same number of atoms as the slab, E_{bulk} , and a relaxed energy of the cleaved system, E_{slab} , then the surface energy, E_{surf} , is defined by:

$$E_{surf} = \frac{E_{slab} - E_{bulk}}{A}, \quad (4.4)$$

where A is the surface area of the cleaved system. For any stable material the surface energy must be positive. In our 2D model, E_{surf} is calculated as:

$$E_{surf} = \frac{E_{slab} - E_{bulk} - E_{pc}}{A}, \quad (4.5)$$

where E_{pc} is one half of the energy of an unrelaxed cleaved slab where the charge of the top and bottom layer was spread uniformly minus E_{bulk} .

4.4 The Dipole Effect on the Atomic Structure of ZnO Polar Surfaces

As discussed above it is essential to compensate the inherent dipole of the ZnO polar surfaces; however, there is no energetic and structural study of the importance of cancelling completely the dipole. In this section, we study the effect of the dipole moment on the atomic structure and energetic rankings. Our first model (weak dipole) was built by moving Zn and/or O ions from the top to the bottom layer until satisfying the relation: $|m_{Zn} - m_O|/25 \approx 0.24$, where m is the number of ions i in the topmost surface layer. Twelve different stoichiometries were chosen between the two polar ZnO surfaces. In the second model (dipole = 0), the inputs of the lowest five energy structures from the first model were then locally optimised with the use of point charges. Results are displayed in Figure 4.4, which shows the ranking for the different approaches. We note that the residual dipole plays a very important role on the ZnO polar surfaces, as energies and surface structures differ and only data points on the blue line did not change rankings after cancelling completely the dipole. Therefore, all the structures discussed below will be referred to those optimised with the use of point charges.

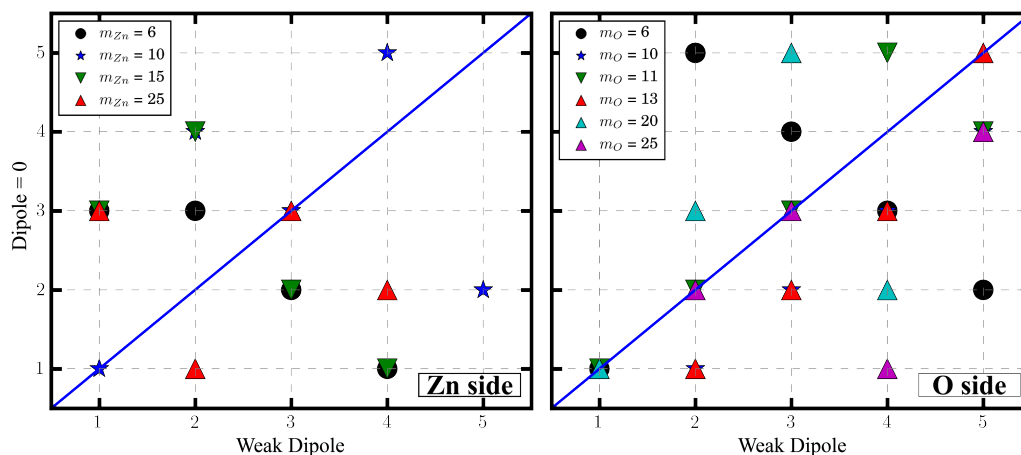


Figure 4.4 Energetic rankings for five optimised structures using both with and without compensating point charges. Twelve different stoichiometries were tested between the two ZnO polar surfaces. Data points on the blue line represent atomic structures that did not change energetic rankings. Data points out of the blue line show structures that changed energetic rankings, meaning a difference between *weak dipole* and *dipole = 0* approaches (more description of these methods is given in Section 4.4).

4.5 Surface Energies

The surface energy of a material determines its stability along a specific orientation. Figure 4.5 displays the surface energy for the whole range of stoichiometries for both polar surfaces, 26 in total for each surface termination. The O-terminated $(000\bar{1})$ surface proves to be more stable than the Zn terminated (0001) surface by *ca.* 0.105 J/m^2 on average. The higher stability of the oxygen terminated surface predicted in this study implies that, under thermodynamic control, the $(000\bar{1})$ surface is expected to be more expressed; whereas experiment report a faster $(000\bar{1})$ growth with respect to the (0001) surface [132]. The oxygen terminated surface shows less variation in energy than the Zn terminated face; the difference between the maximum and minimum is about *ca.* 0.175 J/m^2 compared to *ca.* 0.230 J/m^2 for the Zn face. The relatively small difference in surface energy in the $(000\bar{1})$ surface with respect to the stoichiometry suggests a larger range of approximately equally stable structures, which would make it very difficult to attribute a single pattern to this surface. In the Zn terminated surface, the crystal growth will be mainly attributed to those compositions with low energies. The change of surface energy as a function of the stoichiometry (Figure 4.5) might be an explanation for the experimental

behaviour observed for the polar surfaces of ZnO crystals: experiment have shown that to identify a reconstruction pattern in the (0001) termination is easier than in the (000 $\bar{1}$) surface. Experimentally, it has been more difficult to attribute a single reconstruction pattern to the (000 $\bar{1}$) surface than to the (0001) surface. Experiments supported by *ab initio* calculations have shown that, under certain conditions, triangular patterns are formed as a stabilisation mechanism for the (0001) surface whereas for the (000 $\bar{1}$) surface hexagonal patterns form occasionally [57, 120, 122, 123, 126]. Moreover, in the case of the (000 $\bar{1}$) surface, substantial amounts of OH groups are expected to be present at low temperatures even at UHV conditions. However, the areas covered by hexagonal patterns in the O terminated surface are not as wide as the triangular ones in the Zn terminated surface. Additionally, the (1 \times 1) periodicity suggested by experiment [109–112] can be a result of the amount of disorder suggested by our calculations. Our calculations support the fact that slight changes to the synthesis conditions lead to different atomic configurations.

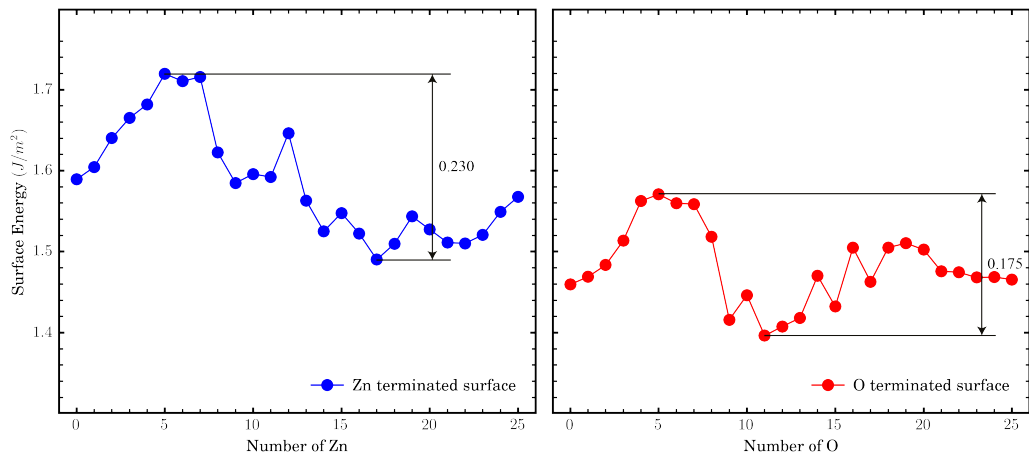


Figure 4.5 Surface energies of the polar surfaces as a function of the stoichiometry. For each data point the relation $|m_{Zn} - m_O|/25 \approx 0.24$ was conserved.

4.6 Atomic Structure

Figure 4.6 presents the lowest energy surface structures for each stoichiometry with the Zn termination, and Table 4.1 shows the average atomic relaxation for the first two atomic double layers. On average, for this termination, we observed strong

inwards relaxation from the topmost Zn atoms. For the topmost O atoms, the movement depends on the stoichiometry and is only strong for $0 < m_{Zn} < 5$. In this range, the oxygen atoms relax towards the bulk by -0.15 \AA to -0.66 \AA , increasing the relaxation as the Zn coverage decreases. For the second double layer, we calculate weak outwards relaxations. For example, the strong relaxations observed for $m_{Zn} < 9$ make some Zn ions move from the second layer to the top layer. In our calculations, three different atomic configurations are observed: stripes, triangles and random vacancies. As the size increases the triangular reconstructions start to appear, but it is not until $m_{Zn} = 9$ that a well defined triangular configuration is observed. Triangular reconstructions appear among several different stoichiometries and their stability is supported by the surface energy plot (Figure 4.5). For a higher m_{Zn} , the lowest energy structures are with conglomerated vacancies rather than isolated ones. We observed that for $m_{Zn} > 19$, oxygen adatoms are spread above the first layer in interstitial sites. The extra zinc ions help to fill the holes left by the missing zincs. At $m_{Zn} = 25$ there is no vacancy either in the first or second layer. The first layer presents smooth lateral displacements with 6 oxygen on top in interstitial sites. Triangular reconstructions of different sizes are observed among the stoichiometries. We noted as well that, most of our reconstructions are surrounded by oxygen edges. Even though triangular reconstructions appeared in some stoichiometries, in agreement with experiment, we do not see a definitive preference for such reconstructions. From Figures 4.5 and 4.6 we conclude that triangular reconstructions are a mechanism of stabilisation but not the only one. The preferred configuration, as seen in experiment, will depend on synthesis conditions and surface stoichiometry.

Figure 4.7 shows the lowest energy surface structures for the $(000\bar{1})$ surface. In contrast to the Zn termination, there is no ionic exchange between layers. For a range of $0 < m_O < 6$, the lowest energy structures show small islands spread all over the surface with Zn interstitials. For $m_O = 0, 2$, hexagonal patterns appear formed with a combination of zinc and oxygen interstitials, the smaller hexagon is regular with a side length of 5.65 \AA ; whereas the bigger hexagon has two sides

of 11.3 Å and four of 8.59 Å. At $m_O = 6$, there is the first well defined triangular pattern, which increases smoothly till $m_O = 11, 12$, where well defined big triangles connected by oxygen interstitials are formed. These big triangles have the lowest energy surfaces of all the stoichiometries. For $m_O > 12$, the triangular patterns start to distort and the surface energy increases slightly. An attempt to create a bigger triangle is seen in $m_O = 16$. For $m_O > 19$, oxygen ions start to fill the vacancies and zinc ions sit above the first layer bonded to 3 oxygens from the first layer. The surface energy for $m_O > 19$ remains nearly constant. At $m_O = 25$ all the vacancies from the first layer are filled and the excess of three-coordinated zinc ions are spread over the surface in interstitial sites.

We note that each of the data points displayed in Table 4.1 and Figures 4.5, 4.6 and 4.7 represent the lowest energy structure from 10,000 calculations for a given stoichiometry. Therefore, it is important to know the influence of higher energy states on our system: are there more reconstruction patterns that can be seen? or are only the GM representative? In order to answer these questions, we calculated the average number of unique configurations that can be present at a given temperature as a function of the stoichiometry as:

$$n(T) = \sum_i^N \exp^{-(E_i - E_1)/k_B T} \quad (4.6)$$

where N , E_i , E_1 , k_B and T are the total number of unique configurations, the energy of a unique state i , the energy of the GM, the Boltzmann constant and the temperature, respectively. Equation (4.6) is used under the assumption of a canonical ensemble. Figure 4.8 shows the number of unique structures for four different temperatures: 300 K, 500 K, 1000 K and 5000 K. We observe that, at room temperature (RT), the number of unique structures that are thermally occupied for most of the stoichiometries for both terminations is close one, thus, validating the data presented in Sections 4.5 and 4.6. The latter means that the gap between the GM and the second lowest energy structure is large enough to prohibit the second lowest and higher energy from being present at RT. As expected, for higher temperatures, the number of statistically significant structures increases as there is more disorder.

We also note that where the number of unique structures is greater than one at RT is mainly for the extreme stoichiometries (at the edge of the graph), which could also be expected as the number of possible structures for midrange stoichiometries is much larger than those with high and low stoichiometries. This can be related to the fact that for high and low stoichiometries are easier to change their atomic structure without a strong energetic penalty. As we saw from the Figure 4.9), this happens by moving the isolated atoms. That task is not as easy for midrange, here, to move an atom means a change of coordination number with a strong penalty, making bigger the gap between GM and second lowest minimum. For those cases with more than one unique structure at RT, we compare the atomic arrangement of the higher energy structures with respect to their GM. Figure 4.9 shows four second lowest energy structures for different stoichiometries. For the stoichiometry 2 at the Zn termination, there are no significant changes between the GM and the second lowest energy structure to the naked eye. A similar behaviour is observed for the O termination (stoichiometries 6 and 1); the patterns are conserved, only small changes can be seen: at O-6, the two isolated zinc atoms are closer for the second lowest minimum and for O-1 the energetic difference is also attributed to the distribution of their isolated zinc atoms. For the O-13 stoichiometry, there are some structural changes; however, the pattern is conserved: a big triangle made of vacancies, with the rest of the vacancies being close together. In general, for the cases where more than one structure is significant, the slightly higher energy structures show a very similar atomic arrangement to their GM with only a few changes like a different distribution of isolated atoms or/and a change of coordination number. Therefore, the data in Table 4.1 and reconstruction patterns in Figures 4.5, 4.6 and 4.7 are the only meaningful information at room temperature.

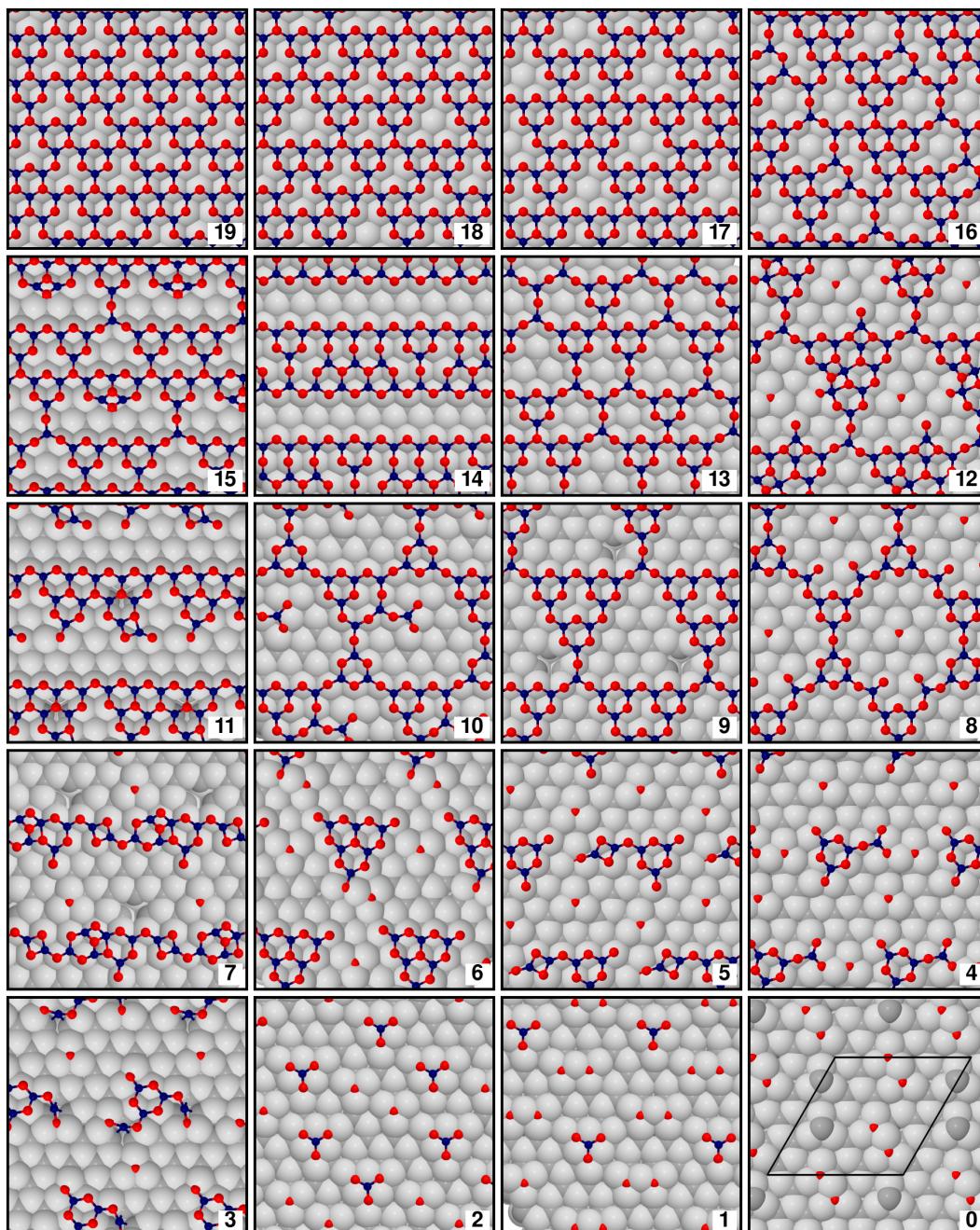


Figure 4.6 Lowest energy structures for the zinc terminated surface. Numbers in each sub-figure represent the number of zincs at the top surface (m_{Zn}); for each stoichiometry there are 6 oxygens more than zincs. The grey colour is reserved for the second layer atoms, dark grey and light grey represent oxygen and zinc, respectively. Red and blue were used for top oxygen and zinc atoms, respectively.

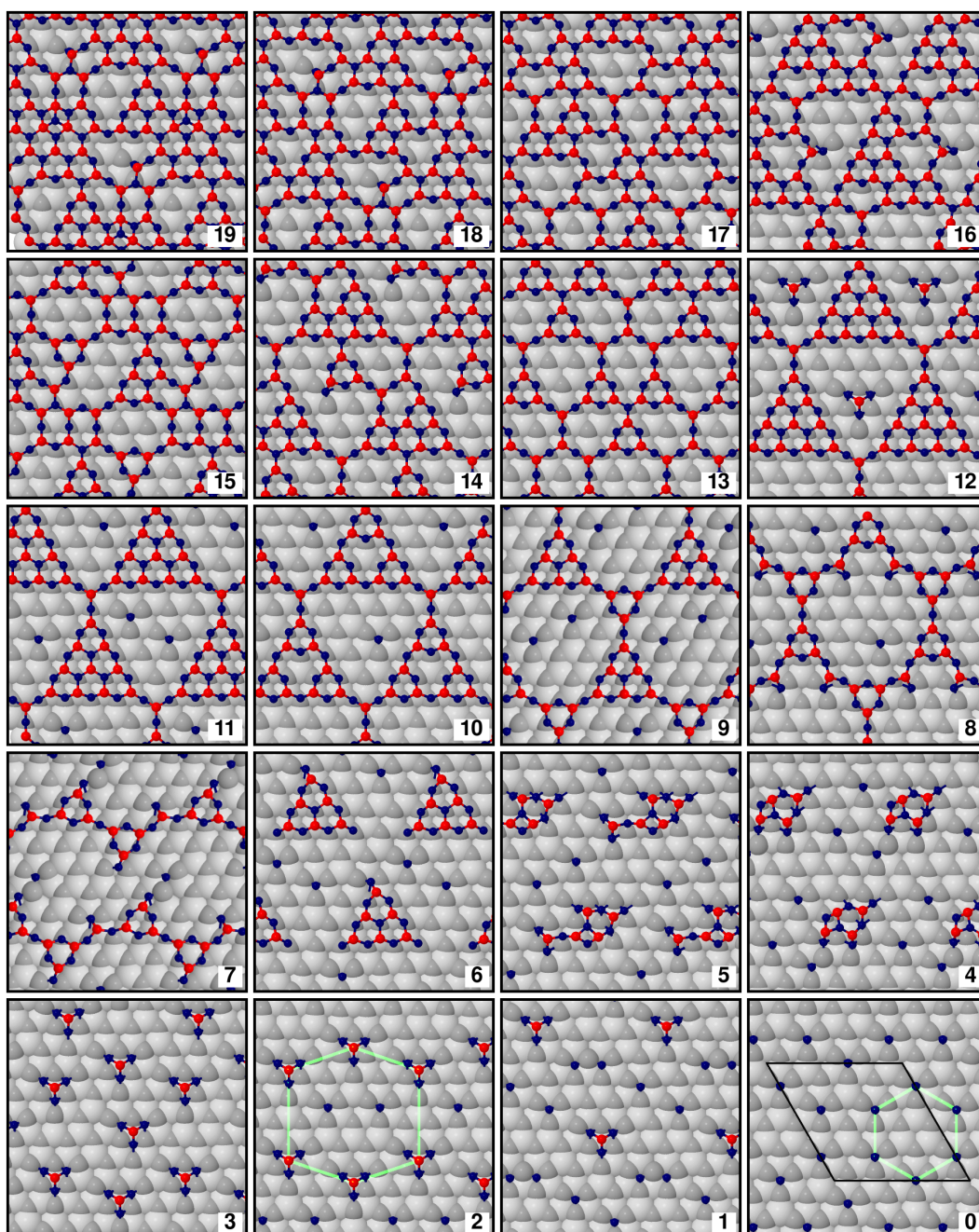


Figure 4.7 Lowest energy structures for the oxygen terminated surface. Numbers in each sub-figure represent the number of oxygens at the top surface (m_O), for each stoichiometry there are 6 zincs more than oxygens. The grey colour is reserved for the second layer atoms, dark grey and light grey represent oxygen and zinc, respectively. Red and blue were used for top oxygen and zinc atoms, respectively.

Table 4.1 Atomic Relaxations of the First Two Layers Along the c Axis of the Polar (0001) and (000 $\bar{1}$) Surfaces. All Relaxations are given in Å.

No. of Zn/O	(0001)-Zn					(000 $\bar{1}$)-O				
	Zn ₁	O ₁	Zn ₂	O ₂	O ₀	O ₁	Zn ₁	O ₂	Zn ₂	Zn ₀
25	0.073	0.124	0.027	0.013	-0.746	0.091	0.045	0.013	0.011	-1.006
24	-0.037	0.036	0.035	0.016	-0.645	0.077	0.049	0.014	0.008	-0.987
23	-0.180	0.028	0.093	0.019	-0.686	0.052	0.049	0.018	0.011	-0.990
22	-0.244	0.028	0.093	0.018	-0.747	0.065	0.094	0.032	0.012	-1.066
21	-0.270	0.016	0.055	0.014	-0.749	0.066	0.127	0.029	0.012	-0.919
20	-0.304	0.001	0.015	0.006	-0.757	0.050	0.135	0.034	0.014	-0.944
19	-0.385	-0.010	0.011	0.003		0.047	0.141	0.024	0.012	
18	-0.368	-0.004	0.014	0.006		-0.016	0.086	0.029	0.014	
17	-0.354	0.002	0.018	0.010		-0.079	0.010	0.012	0.007	
16	-0.344	-0.004	0.015	0.007		-0.029	0.029	0.035	0.015	
15	-0.227	0.077	0.018	0.012		-0.111	-0.040	0.009	0.007	
14	-0.277	0.028	0.023	0.017		-0.107	-0.059	0.021	0.011	
13	-0.227	0.039	0.026	0.016		-0.145	-0.092	0.001	0.006	
12	-0.236	0.029	0.015	0.018		-0.075	-0.106	0.047	0.005	
11	-0.311	0.040	0.064	0.017		-0.026	0.029	0.050	0.020	
10	-0.244	-0.026	0.022	0.025		-0.086	-0.167	0.030	0.013	
9	-0.270	0.014	0.078	0.033		-0.069	-0.203	0.053	0.015	
8	-0.212	-0.039	0.031	0.033		-0.101	-0.274	0.061	0.013	
7	-0.450	0.115	0.183	0.033		-0.082	-0.311	0.089	0.022	
6	-0.196	-0.084	0.027	0.034		-0.058	-0.278	0.074	0.029	
5	-0.238	-0.151	0.012	0.031		0.032	-0.351	0.108	0.032	
4	-0.234	-0.218	0.023	0.037		0.072	-0.392	0.140	0.058	
3	-0.333	-0.321	0.023	0.039		-0.144	-0.646	0.126	0.048	
2	-0.340	-0.548	0.010	0.045		-0.317	-0.781	0.109	0.037	
1	-0.344	-0.588	0.001	0.038		-0.317	-0.877	0.119	0.047	
0	0.000	-0.664	0.015	0.050		0.000	-1.016	0.112	0.042	

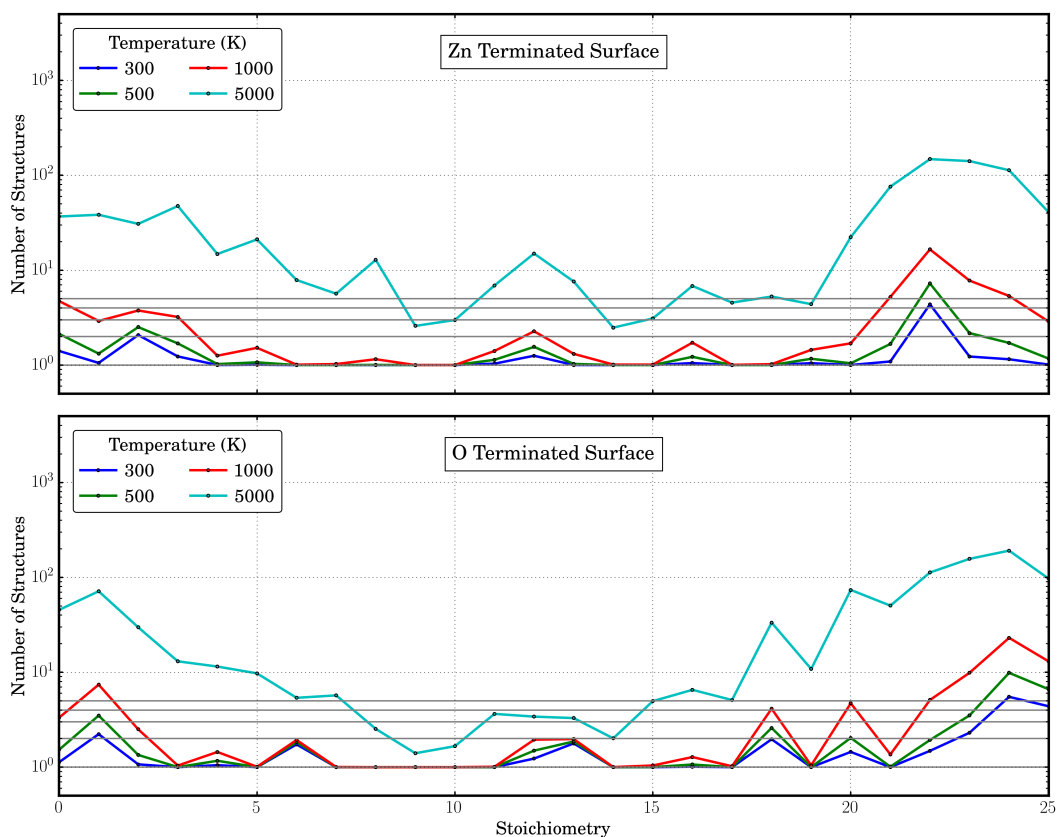


Figure 4.8 Number of significant unique surface reconstructions as a function of the stoichiometry for different temperatures. The horizontal grey lines represent 1,2,3,4 and 5 unique structures, respectively. The nomenclature of the stoichiometries are used as in Figures 4.5, 4.6 and 4.7

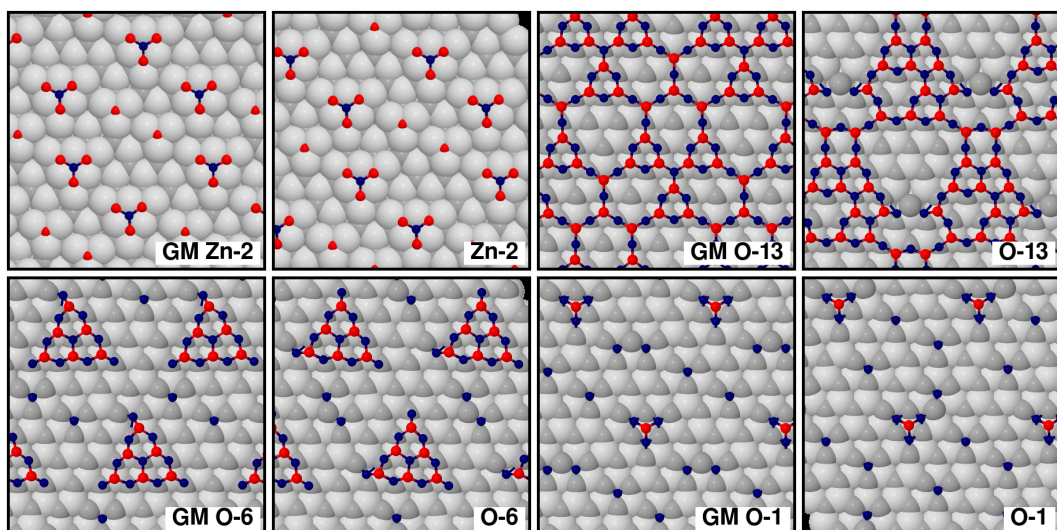


Figure 4.9 GM and second lowest energy structures for selected stoichiometries. Nomenclature represents the surface termination and the stoichiometry.

4.7 Summary and Conclusions

We studied the stabilisation mechanism of the polar ZnO surfaces by means of inter-atomic potential methods. Our calculations provide a detailed computational study for the crystal growth of the polar ZnO surfaces. The inherent dipole in the polar ZnO surfaces was cancelled by both ionic transfer between surface sides and a set of point charges spread over both sides of the surfaces. We have demonstrated the importance of cancelling the dipole on the ZnO polar surfaces. Neither the atomic structure nor the energetic ranking was kept between the *weak dipole* and *zero dipole* stabilisation mechanisms for the polar surfaces. The first approach minimises the dipole by transferring ionic charges between top and bottom layers, while the second one adds a set of point charges, which cancels completely the dipole. Among twelve different stoichiometries distributed between the two polar terminations, the two approaches showed difference in atomic structure and energetic rankings. Therefore, we conclude that the dipole plays a crucial role in energetics and atomic structure.

The calculated surface energies indicate a higher stability of the $(000\bar{1})$ -O surface over the (0001) -Zn surface. On average, there is a *ca.* 0.102 J/m^2 higher surface energy for the Zn terminated face. For the $(000\bar{1})$ surface, the change in surface energy as a function of stoichiometry is about a 24% of that seen for the (0001) surface. This finding suggests that it is more likely to find a larger range of approximately equally stable stoichiometries in the $(000\bar{1})$ surface than in the (0001) surface. The latter finding is supported by experiment, where it has been easier to identify patterns in the (0001) -Zn surface than in the $(000\bar{1})$ -O surface. We suggest that the (1×1) periodicity seen in experiment can be a result of the amount of disorder predicted by our calculations.

Structurally, the ZnO polar surfaces also behave differently. While on the Zn terminated side, we calculated pronounced relaxations across the surface with some ions (Zn) jumping from the second layer to the first layer, on the O terminated side the movements are not so strong and the ionic transfer between layers only happens when the top zinc layer is full ($m_O > 19$), and every oxygen that is transferred

to the top layer serves to fill the oxygen vacancies. For both surfaces, triangular reconstructions are common. The triangular reconstructions shown in this work for the Zn terminated side agree with STM images [57], whereas experiment suggests hexagonal reconstructions. In our calculations, only hexagonal patterns are observed for $m_O = 1$ and $m_O = 3$ (Figure 4.7). We demonstrated that, in general, the different stoichiometries will be represented by their GM and that for the cases where more unique structures are representative, a similar reconstruction pattern is expected. We note that further stabilisation of the structures presented here may be possible. Future work will examine larger reconstruction patterns in a (10×10) supercell size, as well as the possible combination of two stoichiometries with low surface energy.

Chapter 5

The Cu/ZnO System

5.1 Introduction

The Cu/ZnO system is of great interest in the chemical industry due to its wide use in the water-gas shift reaction [133], methanol steam reforming [134] and synthesis of methanol [135]. For example, the production of methanol was estimated to be 65 million tonnes per year in 2013 [12]. This system has been widely studied both experimentally and theoretically. Due to its activity in the methanol synthesis process, most of the studies have been focused on copper deposition on the ZnO polar surfaces. However, the nonpolar ZnO surfaces are predominant and contribute up to *ca.* 80% of the total surface area [136]. Additionally, nonpolar surfaces are easier to model (*e.g.* they do not present a dipole moment across the slab nor show atomic reconstructions), which makes them ideal to describe Cu-ZnO interactions.

The low computational cost of IP calculations compared with *ab initio* allow us to optimise a vast number of structures (*e.g.* a bigger portion of the energy landscape) in a reasonable amount of time, from which the lowest energy structures can be selected as candidates to be refined with the DFT approach.

In this Chapter, we focus on the atomic structure that results from the interaction between copper clusters and ZnO nonpolar surfaces, which have been investigated by means of interatomic potentials and DFT methods. The first section is focused on the atomic structure of small copper clusters and their growth on the nonpolar ZnO surfaces, which is followed by a description of the methods used

throughout this Chapter. In the results section, we discuss the fitting of the Cu/ZnO interatomic potentials to DFT structures and energies, followed by DFT calculations performed to optimise the procedure for our global optimisation technique. Then, the new Cu-ZnO IP are used to perform global optimisation calculations of eight Cu atoms (this number provides a good balance between cluster size and computing time required to find the global minima) deposited on the $(10\bar{1}0)$ surface. From the latter calculations, the lowest five energy Cu/ZnO structures were refined and compared through DFT. Lastly, we perform global optimisation calculations of Cu_n clusters ($1 \leq n \leq 7$) deposited on the $(10\bar{1}0)$ surface at the atomistic level. At the end, we give a brief summary of our results and future planned work.

The work summarised in this Chapter is part of an international collaboration with Professor Stefan Bromley (Universitat de Barcelona) to fit potentials between metals and metal oxide surfaces as interatomic potentials are used in global optimisation techniques to study metal cluster growth as well as to predict new interface structures. All work presented in this Chapter is, however, my own.

5.1.1 Small Cu Clusters

We showed in Chapters 3 and 4 that ZnO IP provide very similar structures to those from DFT calculations. With respect to the Cu-Cu interatomic interactions, the Gupta many-body potentials by Cleri and Rosato [8] have been widely used to study cluster structures, growth and dynamics [137–140]. For example, these Gupta potentials have been used to study Cu_n clusters ($n \leq 56$) using a genetic algorithm (GA) [137]. Atomic structures were found to have high symmetry geometries (an effect of attractive long-range forces in the Gupta potential) and mainly based on icosahedral structures [137]. The latter structures can be compared with previous studies using different techniques [141–143].

Global minimum structures for Cu_n clusters ($3 \leq n \leq 8$), predicted in this work using the Gupta potentials derived by Cleri and Rosato [8], are presented in Figure 5.1. These structures show a good agreement with previous experimental and theoretical studies [137, 138]. All global minima structures have triangular faces (as mentioned earlier, the high symmetry is attributed to the attractive long-range

forces in the Gupta potential). The atomic structure of Cu_n clusters is as follows: Cu_3 cluster = equilateral triangle, Cu_4 = triangular pyramid (tetrahedron), Cu_5 = triangular bipyramid, Cu_6 = regular octahedron, Cu_7 = pentagonal bipyramid, and Cu_8 = snub disphenoid.

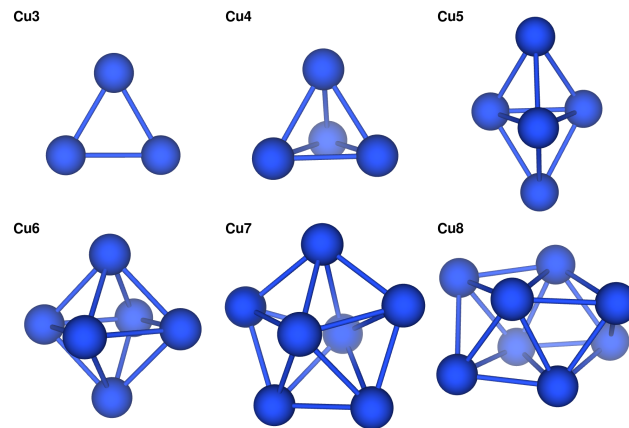


Figure 5.1 Global minima Cu_n clusters ($3 \leq n \leq 8$) as calculated with the Gupta interatomic potentials [8].

5.1.2 Cu Growth on Nonpolar Surfaces of ZnO

As mentioned previously, the growth of copper on ZnO surfaces is of great interest due to its commercial applications. STM images [144] show that one mono-layer (ML) of copper on the $(10\bar{1}0)$ ZnO surface wets the surface, whereas at lower coverages of 0.025 ML exclusively 3D Cu clusters are found. These 3D metallic particles include 2-3 layers of Cu, 6 – 9 Å height and 15 – 40 Å diameter. As discussed in Chapter 3, the $(10\bar{1}0)$ ZnO surface is highly stepped. STM images [144] display a high concentration of steps with edges decorated with Cu clusters, mainly on steps running along the $[001]$ direction. Clusters on edges along the $[1\bar{2}0]$ direction and on terraces (away from the step edges) are rarely seen. At higher Cu coverages (0.05-0.5 ML), the concentration of clusters increases faster than their average size. According to this STM study [144], the nucleation of Cu takes place in the following sequence: along the $(1\bar{2}10)$ steps > on the terraces > along the (0001) steps.

Electronically, photoelectron experiments show that at low Cu coverages, there is a downward band bending of ZnO which is attributed to an electronic transfer from Cu to ZnO [104, 145], whereas at high Cu coverages, the ZnO band bending

disappears. This charge transfer was confirmed with a hybrid DFT study by Hellström et al. using small Cu clusters (with $n \leq 9$) on the $(10\bar{1}0)$ ZnO surface. In the latter study it was concluded that even-numbered clusters are always charge-neutral, while odd-numbered clusters can become positively charged by donation of an electron to the ZnO conduction band.

5.2 Methodology

In this Chapter, all the electronic structure calculations were performed using the periodic plane-wave Vienna Ab-initio Simulation Package (VASP) [47, 48] employing the generalized gradient approximation (GGA) PBEsol functional [40]. The interactions between core (Zn:[Ar], O:[He] and Cu:[Ar]) and valence electrons were described with the projector augmented wave (PAW) approach [45, 49]. The ZnO surface models employed in this Chapter were the nonpolar $(10\bar{1}0)$ and $(11\bar{2}0)$ surfaces. As in previous Chapters, a kinetic energy cutoff of 700 eV was sufficient to converge the lattice energy to less than 1 meV. Supercell sizes of (4×4) and (4×3) with a vacuum slab of 18 Å were found to be large enough to avoid the effects of spurious interactions between repeated cells. In the $(10\bar{1}0)$ ZnO surface, a $2 \times 1 \times 1$ gamma centred k -point mesh was used for the (4×4) supercells and $2 \times 2 \times 1$ for the (4×3) . When an atomic relaxation was performed, the forces on all ions were converged to less than $0.02 \text{ eV}\text{Å}^{-1}$. DFT calculations served two purposes in this Chapter: to generate the data to which the interatomic potentials are fitted and to refine the Cu/ZnO structures obtained with global optimisation techniques.

The interatomic potential calculations were carried out using the General Utility Lattice Program (GULP) [30, 31] with the shell model potentials for ZnO developed by Whitmore et al. [55] (presented in Table 5.1 and used in Chapters 3 and 4), and an embedded-atom model interatomic potentials for Cu by Cleri and Rosato [8] (Table 5.2). The interatomic potential parameters representing the Cu-O and Cu-Zn interactions were fit to a set of data: geometries and energies of a series of periodic single point (SP) DFT calculations of Cu_4 and Cu_8 clusters interacting with the bulk terminated nonpolar $(10\bar{1}0)$ and $(11\bar{2}0)$ ZnO surfaces. These data

were validated using a higher quality hybrid DFT test on the $\text{Cu}_4/(11\bar{2}0)\text{-ZnO}$ system. Figures 5.2 and 5.3 show the schematic model used to generate the data. For Cu_4 , one adsorption site on each ZnO surface was employed (Figure 5.2), whereas for Cu_8 , 3 different sites were chosen: two on the $(10\bar{1}0)$ and one on the $(11\bar{2}0)$ ZnO surface (Figure 5.3). A set of 18 SP calculations for each site was used for the fitting procedure (90 points in total). Among these 18 SP calculations, only the z coordinate of the Cu atomic positions varies, see side views of Figures 5.2 and 5.3. The distances between the topmost ZnO surface atom and the closest Cu atom were varied in steps of 0.1 Å from 1.5 to 2.0 Å, of 0.2 Å from 2.0 to 3.0 Å, and of 0.5 Å from 3.0 to 6.0 Å. Additionally, one SP calculation was made at 9.0 Å (at the middle of the vacuum slab), which represents the Cu cluster being in gas phase having no interaction with the ZnO slab and where the adsorption energy is zero, the energy of this point was shifted to zero and the rest of observables are reported with respect to this value. Buckingham and Morse potentials (Table 5.3) were used to describe the Cu-O and Cu-Zn short-range interactions, respectively. Greater details of the fitting procedure are given in the following section.

The new Cu-ZnO interatomic potentials were used in global optimisation calculations of Cu_8 on the $(10\bar{1}0)$ ZnO surface with the Knowledge Led Master Controller (KLMC) code, the features of which have been discussed in Chapter 2, and which was applied in Chapter 4. The solid solutions routine was used to perform this task, which created 1,000 different Cu/ZnO structures by swapping Cu ions over a given lattice mesh. A ZnO slab of size (4×3) and a depth of 5 *double* atomic layers (240 atoms) was employed with the restriction that only Cu atoms are fully relaxed. The Cu mesh used was 3 atomic layers (41 atoms) in a (4×4) supercell of the (110) Cu surface, where the closest Cu atoms are at *ca.* 2.5 Å above of the topmost ZnO surface atom (Figure 5.4). The structure and stability of the lowest five structures were verified with DFT calculations.

Table 5.1 Parameters of the Interatomic Potentials Used for Zinc Oxide. ^a

Buckingham	Range (Å)	A (eV)	ρ (Å)	C (eV Å ⁶)
Zn _c -O _s	0.0 – 2.2	592.342818	0.352159	12.896893
Zn _c -O _s	3.1 – 3.3	157.297013	0.429673	5.815914
Zn _c -O _s	3.6 – 12.0	912.517869	0.078935	11.723055
O _s -O _s	0.0 – 12.0	23674.698081	0.226404	33.476469
Polynomial		C ₀ (eV)	C ₁ (eV Å)	C ₂ (eV Å ²)
Zn _c -O _s	2.2 – 3.1	111.901725	–158.727040	89.657363
Zn _c -O _s	3.3 – 3.6	64102.354057	–93216.170229	54188.807700
		C ₃ (eV Å ³)	C ₄ (eV Å ⁴)	C ₅ (eV Å ⁵)
Zn _c -O _s (cont.)	2.2 – 3.1	–24.986350	3.399631	–0.177932
Zn _c -O _s (cont.)	3.3 – 3.6	–15741.070904	2284.873362	–132.581025
Spring		k ²	k ⁴	
O _c -O _s	0.0 – 0.6	55.518883	2625.567362	
L-J		A(eV Å ¹²)	C (eV Å ⁶)	
Zn _c -O _s	0.0 – 2.2	316.435204	0.000000	
Ion charges	charge (–e)			
Zn _c	2.000000			
O _c	1.754415			
O _s	–3.754415			

^a Table taken from Ref. 55. Zn_c, O_c and O_s represent Zn core, O core and O shell, respectively. All short-range potentials were cut off at 12 Å. The potential between Zn core and O shell is split into three regions, each of which deals with a specific coordination sphere of the opposed ions. The polynomial potentials are used to spline the regions together, and across the whole range, the ZnO potential function is continuous. The forms of the potentials described above are: $E(\text{Buckingham}) = A \exp(-R/\rho) - C/R^6$, $E(\text{Lennard-Jones}) = A/R^{12} - C/R^6$, $E(\text{Spring}) = (1/2)(k^2 r^2 + k^4 r^4)$, $E(\text{Polynomial}) = C_0 + C_1 R + C_2 R^2 + C_3 R^3 + C_4 R^4 + C_5 R^5$, $E(\text{Coulomb}) = q_1 q_2 / R$, where R represents the distance between the ions in question.

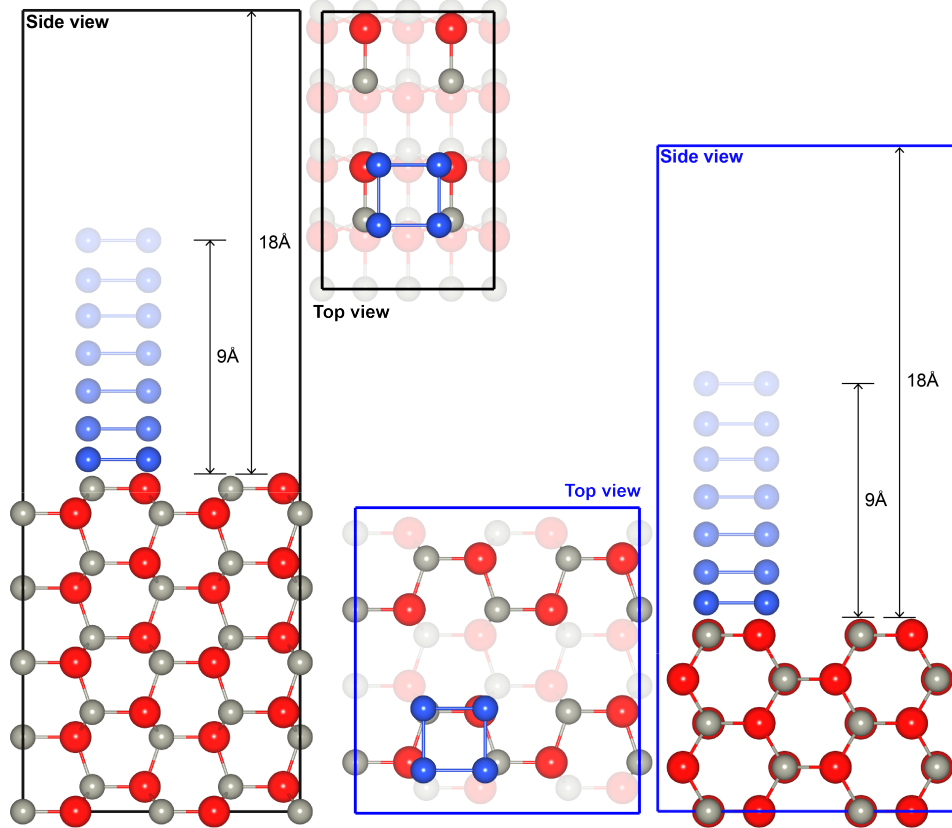


Figure 5.2 Top and side views of the $\text{Cu}_4\text{-ZnO}$ structural model employed in fitting parameters of interatomic potentials to DFT data. The $(10\bar{1}0)$ (black) and the $(11\bar{2}0)$ (blue) (2×2) supercell are shown. In the side views, different blue shades were used to represent the heights of the SP calculations. Blue circles are reserved for copper atoms.

Table 5.2 Parameters of the Interatomic Potentials Used for Copper. ^a

Buckingham	Range (Å)	A (eV)	ρ (Å)	C (eV Å ⁶)		
Cu-Cu	0.0-12.0	9837.021759	0.233229	0.0		
Embedded Atom Model						
Cu-Cu	0.0-12.0					
	EAM Functional	EAM Density				
	Type	A	Type	A	β	r_0
	Square root	1.0	Baskes	1.498176	4.556	2.556191

^a Potentials taken from [8]. The values presented in this table are a conversion from the Gupta potentials, where the repulsive part was adapted to the Buckingham potential and the many-body term to the embedded atom model.

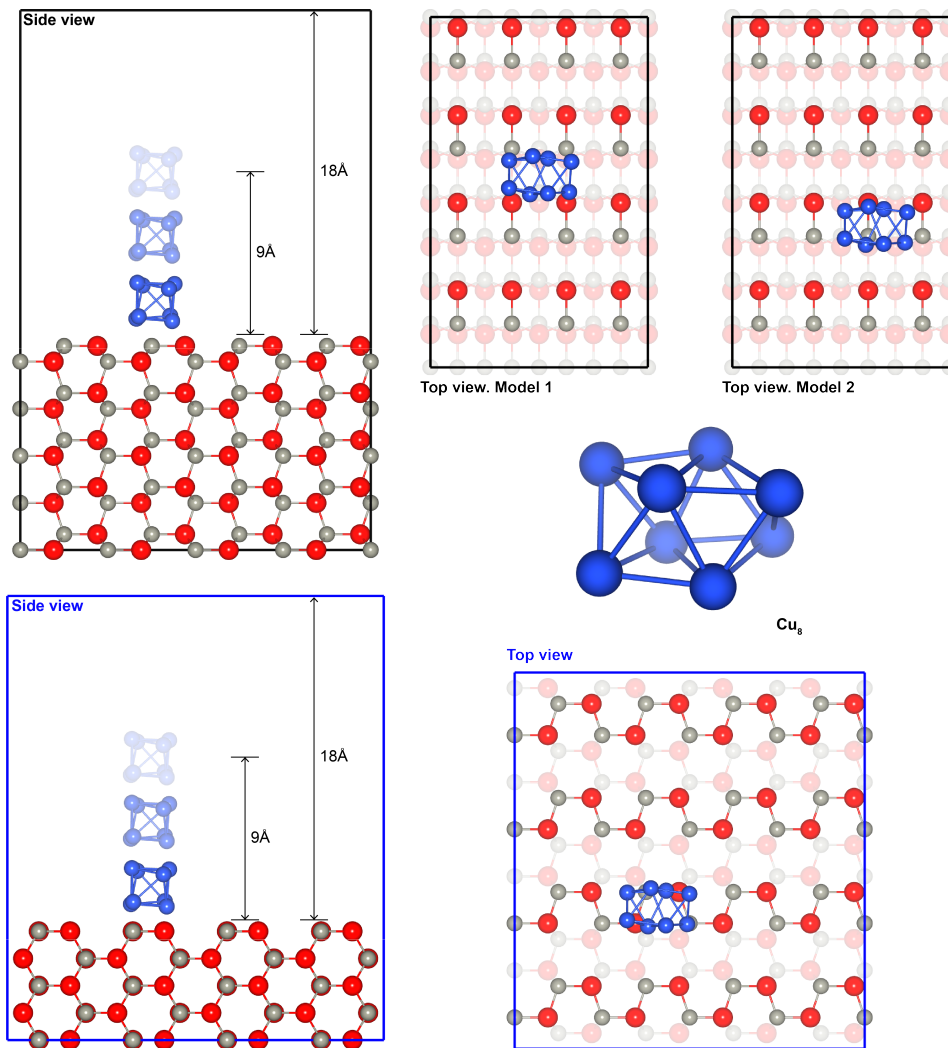


Figure 5.3 Top and side views of the Cu₈-ZnO structural model employed in fitting parameters of interatomic potentials to DFT data. The (10 $\bar{1}$ 0), in black, the (11 $\bar{2}$ 0), in blue, (4 × 4) supercell and the GM Cu₈ cluster are shown. In the side views, different blue shades were used to represent the heights of the SP calculations. Blue circles represent copper atoms.

Table 5.3 Interatomic Potentials Parameters for the Cu-ZnO System. A Radial Cut-off of 12 Å was Used for All Potentials. The Forms of the Potentials Described Below Are: $E(\text{Buckingham}) = A \exp(-R/\rho) - C/R^6$, $E(\text{Morse}) = D_e((1 - \exp(-a(R - r_0)))^2 - 1)$, Where R Represents the Distance Between the Ions in Question.

Morse	D_e (eV)	a_0 (Å ⁻¹)	r_0 (Å)
Cu-Zn	1.148402	1.7393	2.23494
Buckingham	A (eV)	ρ (Å)	C (eV Å ⁶)
Cu-O	46.34077	0.593419	0.0

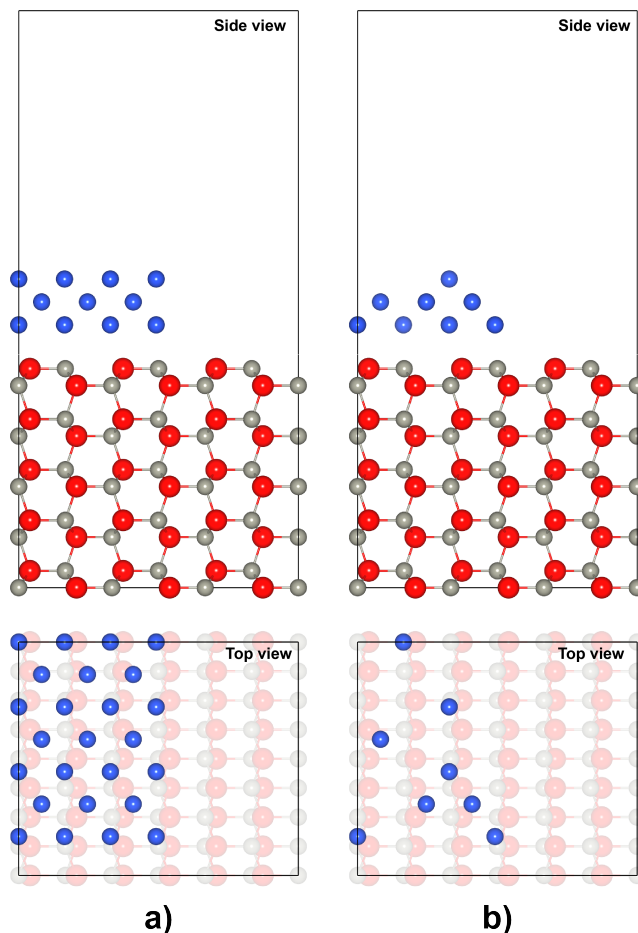


Figure 5.4 Graphical representation of the global optimisation process used within KLMC. (a) Shows the 5 *double-layer* (4×3) ZnO surface with 3 atomic layers of a (4×4) supercell of the (110) Cu surface on top of it. This picture shows 41 Cu lattice positions from which 8 will be occupied. (b) A structure example created by KLMC after the swapping process with 8 Cu occupied lattice positions.

5.3 Fitting of Interatomic Potentials

The number of atomic arrangements for small systems such as Cu_n/ZnO ($n \leq 9$) can be huge and unfeasible to study at the DFT level. On the other hand, good IP can provide a reasonably accurate atomic structure and energetic information at a much cheaper computational cost: for example, one single 200 atom structure can be optimised in *ca.* one hour using one computer core, whereas the same calculation at the DFT/GGA level can take up to one day (depending on how far the initial structure is from the local minimum) using hundreds of cores. Therefore, it is sensible to create interatomic potentials for the Cu/ZnO system, which will save computational resources.

Initially, the Cu/ZnO potentials were fitted using relaxed (10 $\bar{1}$ 0) and (11 $\bar{2}$ 0) ZnO surfaces and the three adsorption sites with a Cu₈ cluster, which are shown in Figure 5.3 (54 observables); however, it was noted that with this configuration the Cu-Zn potential parameters drop to zero. This behaviour is due to the termination of the surface slab: as discussed in Chapter 3, both nonpolar ZnO surfaces show an ionic termination with strong cationic relaxation towards the bulk, thus, increasing the Cu-Zn distance and showing a weak interaction. However, our DFT calculations using a Cu atom on top of a Zn ion showed high positive Cu-Zn adsorption energies at short distances e.g. *ca.* 1.5 Å. From the latter observation, it is concluded that the relaxed ZnO atomic surface structures are not optimum to compute the interactions between Cu and Zn atoms at the DFT level. Therefore, the Cu-Zn interactions were taken into account by using bulk-like nonpolar ZnO surface terminations.

Our potentials were initially fitted to Cu₈ clusters; however, they were tested and refitted using a combination of Cu₄ and Cu₈ clusters on different sites on the nonpolar ZnO surfaces. In a second phase, 36 observables were added in the fit using a planar Cu₄ cluster (Figure 5.2), with one adsorption site on each nonpolar ZnO surface. This refinement achieved a good balance between planar and non-planar clusters as well as accurately reproducing the atomic structures of Cu clusters of different sizes.

As discussed in Chapter 2, the Buckingham potential has an intrinsic problem at short interatomic distances: the Cr^{-6} term diverges when the interatomic distance r is close to zero. To avoid this problem and noting that the implementation of a C term in the Cu-O interatomic potential does not improve substantially our fit, the Cr^{-6} was excluded from the potential. In an attempt to improve the accuracy of our two-body Cu-ZnO potentials, Buckingham force field parameters were converted to Morse potentials followed by a further fit optimisation. Our results showed an improvement when a Morse force field described the Cu-Zn interactions. The Morse potential has an implicit attractive term, which is not present in the interaction of the electron rich Cu and O species. Therefore, Cu-Zn interactions were represented by a Buckingham potential. As mentioned in Chapter 2, the Morse potential is

appropriate when the interacting atoms are covalently bonded, e.g. interactions between an adsorbate and a surface.

Finally, Figure 5.5 shows the set of energies as calculated with DFT and those as calculated with the new Cu-ZnO potentials (Table 5.3). Clearly, good agreement between the interatomic potentials and DFT calculations is achieved. When compared with DFT, our IP match the equilibrium bond length in three of the five cases with a disagreement within 0.1 Å for the other two sites: $(10\bar{1}0) + \text{Cu}_8$ model 2 and $(11\bar{2}0) + \text{Cu}_4$. Moreover, a good representation of the energy depth is achieved in all cases.

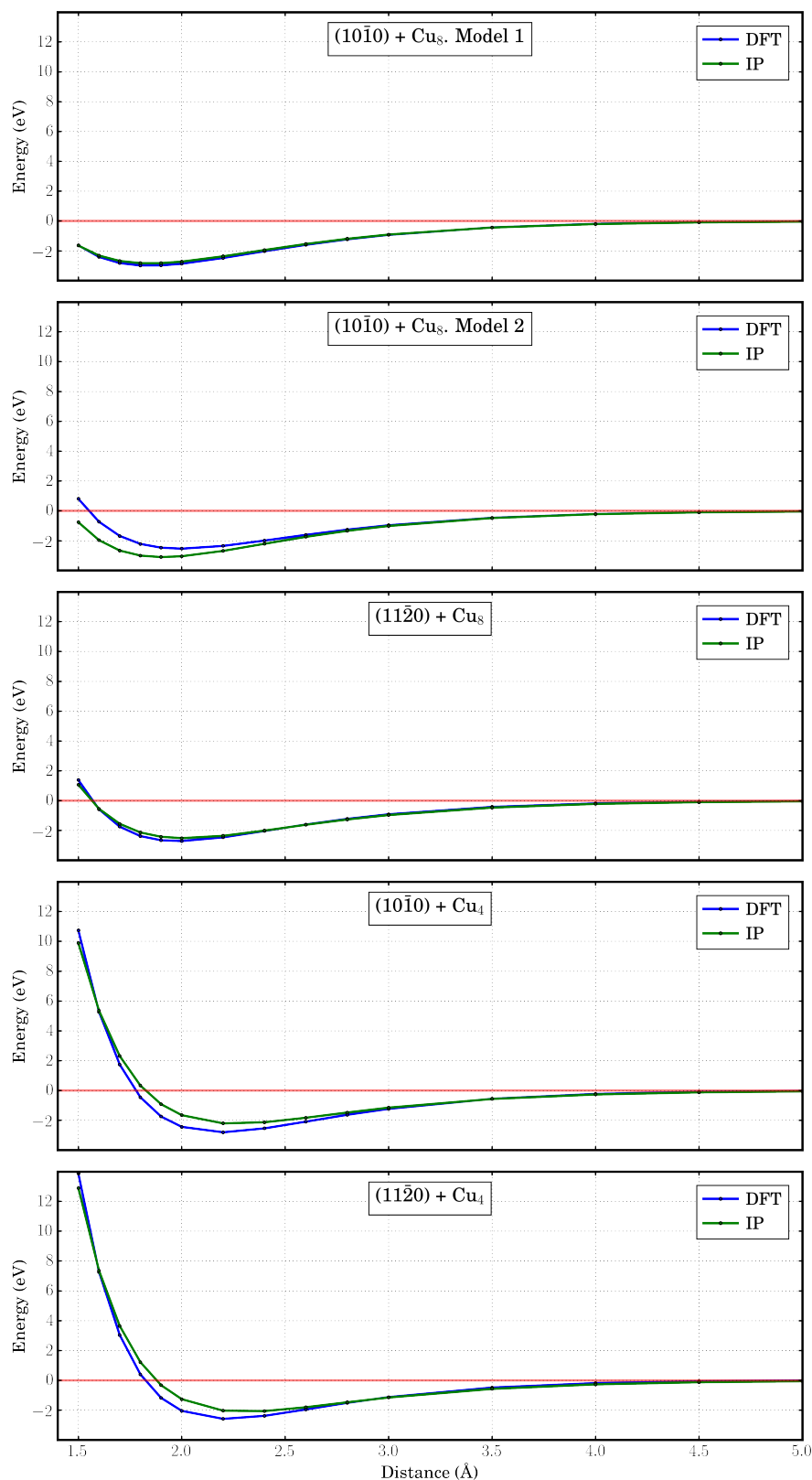


Figure 5.5 Potential fitting curves. Blue and green lines show the adsorption energy observables using DFT and IP, respectively. From 5 Å to 9 Å all the curves remain flat to the naked eye.

5.4 Further Optimisation

In order to speed-up the global optimisation calculations, we have studied different aspects that could modify the Cu/ZnO atomic structure: (i) the effect of the ZnO slab relaxation on the structure of the Cu cluster; (ii) the reduction of the ZnO supercell from (4×4) to (4×3) ; and (iii) the Cu/ZnO optimised structure when two different initial configurations are used.

Figure 5.6 shows the initial and two optimised atomic structures with the difference that the first was fully optimised, whereas in the second only the Cu_8 cluster was allowed to relax. The structural difference between the two optimised configurations is rather small with only noticeable changes in the ZnO slab where Zn ions undergo strong inwards relaxation as previously discussed in Chapter 3. The effect of the ZnO slab relaxation on the Cu_8 atomic structure is small, thus, allowing us to reduce substantially the computational cost in our calculations by keeping the ZnO fixed.

Figure 5.7 displays a reduced (4×3) supercell of the $(10\bar{1}0)$ ZnO surface model with a Cu_8 cluster sited on top of it in two different positions (see top views). In the initial configurations, the three Cartesian coordinates are different between the Cu_8 clusters. After optimisation, both structures find the same atomic structure. Since the $(10\bar{1}0)$ ZnO slab does not have many morphologically different sites, and the Cu_8 is big enough to cover most of them, we would expect that this optimised structure will be found if a different starting point is chosen (using a reasonable distance away from the slab, *e.g.* $3 - 4.5 \text{ \AA}$). We notice as well that this optimised structure is the same as the one shown in Figure 5.6. Therefore, neither the reduction of the ZnO supercell to (4×3) nor the use of different initial configurations affect the DFT results. In our global optimisation calculations, we use a (4×3) supercell with the ZnO slab fixed.

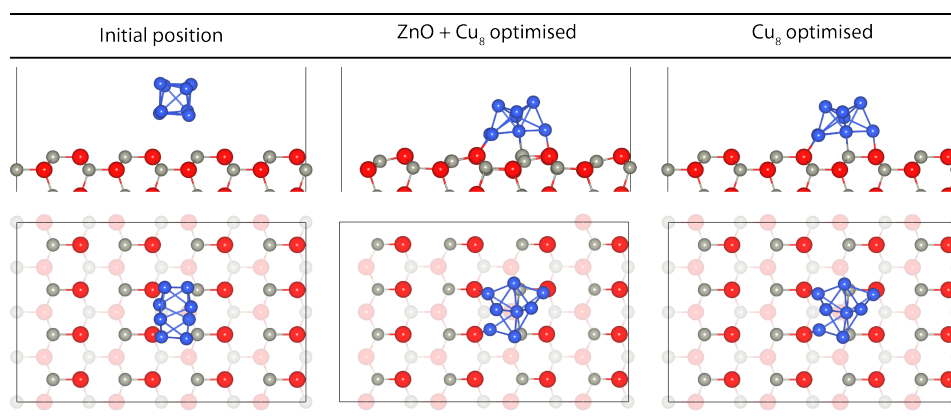


Figure 5.6 Top and side views of the initial and optimised Cu_8/ZnO structures. The black lines represent the (4×4) supercell. All ions were allowed to relax in the figures at the center, whereas in the figures on the right the ZnO atoms were held fixed.

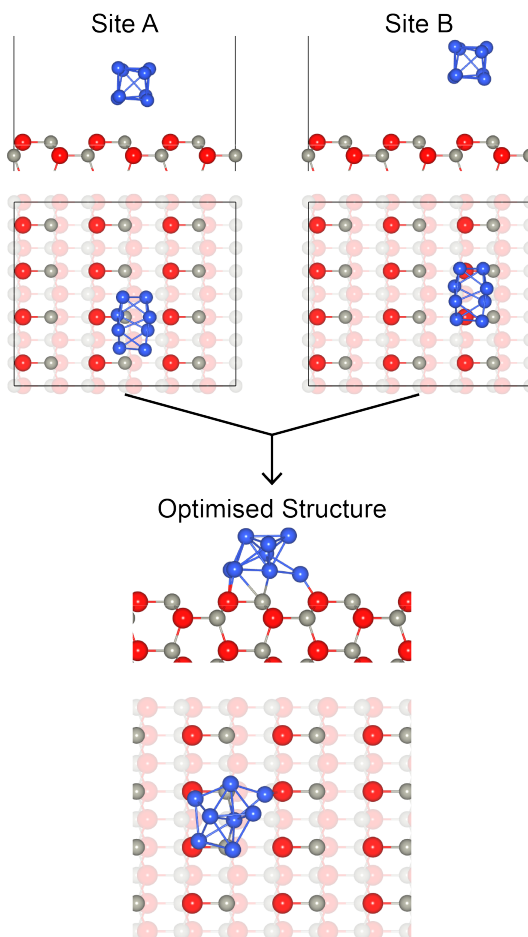


Figure 5.7 Top and side views of two different initial Cu_8/ZnO structures. The black lines represent the (4×3) supercell. Both structures optimised in the same final structure shown at the bottom of the Figure.

5.5 Global Optimisation

A set of 1,000 different Cu₈/ZnO structures was found to be enough to find the global minimum. These structures were optimised using the method described in Section 5.2 and IP presented in Tables 5.1, 5.2, and 5.3. The five lowest energy structures of the Cu-ZnO system, as calculated using IP and refined with DFT, are shown in Figure 5.8. We consider that, analysing those five structures is sufficient to test on our potentials. In general, when compared with DFT, the Cu/ZnO IP show a good agreement both structurally and energetically, although in some cases there are significantly different.

Structurally, similarities between IP and DFT calculations are clear and only few significant atomic displacements are observed. The lowest DFT energy structure was found with two different IP structures. We note a preference for *planar* Cu structures over *non-planar*. The optimised structures were found in less than 40 ionic steps in 60% of the cases, whereas placing a GM Cu₈ cluster at 3 Å can take over 200 ionic steps, thus reducing the computational cost by *ca.* 80%. Copper atoms supported on ZnO tend to form triangular configurations, like those in gas-phase copper clusters.

Energetically, when refined by DFT, the lowest energy structure is 0.32 eV lower in energy than the configuration obtained by relaxation of a gas-phase global minimum Cu₈ cluster placed on top of the ZnO surface at *ca.* 3 Å (Figure 5.7); the atomic structures are different as seen in Figures 5.7 and 5.8. At the DFT level, only the second structure shown in Figure 5.8 is higher in energy than the one in Figure 5.7. Here, structurally, there is no substantial difference between IP and DFT (suggesting that this structure is either situated close to a saddle point or it is very difficult to break its high symmetry); however, the energetic difference is 2.093 eV for DFT (when compared to the DFT GM); whereas for IP it is only 0.097 eV (Figure 5.8). The DFT optimised structures (Figure 5.8) reveal different atomic arrangements from those calculated with IP (not the case for the second structure), which makes direct comparison difficult between IP and DFT energies. The structural modification suggests that electrons play a significant role during the

DFT refinement. We suggest a direct comparison by taking the relative IP energies of the optimised structures and those calculated with DFT, where the DFT energies are taken from a SP calculation on the optimised IP structures. The shifted SP DFT energies are: 0.000 eV, -0.430 eV, 0.016 eV, -0.289 eV and -0.500 eV. The second structure results very stable in comparison with the others, which tell us that the large mismatch is related to its positioning on the DFT landscape: it is very close to the bottom of the saddle point, whereas the other four structures are farther, thus, allowing a further energetic decrease.

We also checked that the optimised DFT structures are not lower in energy (under the IP landscape) than their respective initial IP structures. When an optimised DFT structure is re-optimised with IP, it always finds a lower energy structure, going back to the optimised IP structure (Figure 5.8) in most of the cases.

Structural and energetic discrepancies can be expected not only from our Cu-ZnO fit but also to the ZnO and/or Cu-Cu IP. Since the ZnO slab is held fixed and the strong agreement of their IP and DFT has been proved earlier [55, 86, 92, 146, 147], any mismatch should be linked to either the Cu-Cu or Cu-ZnO potentials. To further rationalise the behaviour of the Cu/ZnO IP, we have calculated the five lowest energy IP structures shown in Figure 5.8, with the modification that the ZnO slab was removed. These periodic single point calculations were performed using both IP and DFT. IP (DFT) energies, with respect to the first structure, are as follows: 0.000 eV (0.000 eV), 0.062 eV (0.345 eV), -1.387 eV (-0.942 eV), -0.261 eV (0.049 eV) and 0.442 eV (0.725 eV). There is a preference for 3D clusters; whereas with the ZnO slab, the Cu clusters wet the surface. On average, there is an energetic difference of *ca.* 0.3 eV between IP and DFT calculations. Additionally, we repeated the previous IP and DFT calculations but using a gas-phase Cu_8 cluster. The results are slightly different from the periodic ones. IP (DFT) energies, with respect to the first structure, are as follows: 0.000 eV (0.000 eV), 0.534 eV (0.558 eV), -2.187 eV (-2.385 eV), -1.044 eV (-1.350 eV) and 0.506 eV (0.678 eV). When compared with the Cu_8 periodic calculations, the stability of 3D clusters is higher; whereas linear structures are more unstable: this may be related to the even further reduction

of coordination number. Again, there is a good agreement between IP and DFT energies with the biggest difference being *ca.* 0.3 eV (fourth structure, Figure 5.8) between the two approaches.

Another factor which could cause a mismatch between IP and DFT calculations is the shape of our Cu-ZnO potentials (Morse and Buckingham) and the curves presented in Figure 5.5. With respect to the Figure 5.5, there are small differences between the set of DFT data and our fit. As discussed in Chapter 2, Morse and Buckingham potentials are employed to model the short range interactions, and (in our case) are represented by three and two parameters, respectively. The small number of variables employed may be not enough to perfectly describe such a complex system.

Generally, our approach and potentials have proved to be very effective in describing the Cu/ZnO system (predicting low energy structures with high accuracy) and to perform global optimisation calculations, which are unfeasible to run at the DFT level. Our calculations suggest that a small IP-DFT mismatch (caused by the landscape difference and the combination of errors in the Cu-Cu and Cu-ZnO potentials) must be expected. However, our potentials can work as a filter to give sensible Cu/ZnO structures with a subsequent DFT refinement.

With the validation of our Cu/ZnO potentials, we proceed to calculate the lowest energy IP structures of Cu_n clusters ($1 \leq n \leq 7$) on the $(10\bar{1}0)$ surface. Figure 5.9 shows the GM structures and energies after global optimisation for Cu_n/ZnO . As copper and oxygen are electrons rich and zinc are poor, we expect a Cu-Zn attraction and a Cu-O repulsion. The latter behaviour is observed in our calculations: Cu configurations tend to avoid oxygen atoms. Moreover, Cu triangular based structures are predominant with a preference for planar Cu clusters. We calculated a decrease of the adsorption energy per Cu atom as the concentration increases, indicating a higher stability for bigger Cu clusters over the smaller ones. The higher stability for planar Cu clusters at low coverages is in agreement with STM studies by Dulub et al. [148], complemented by LEED, UPS and LEIS. In general, they observe a 2D copper growth at low coverages (0.001-0.05 equivalent ML); whereas

at coverages greater than 0.01 ML, 3D clusters start to appear. As suggested earlier by STM images and quantum and molecular mechanical (QM/MM) calculations [148–150], the ZnO substrate shows a strong influence in the Cu growth, as the 3D shape of the most stable “gas phase” Cu clusters disappears when in contact with the ZnO surface.

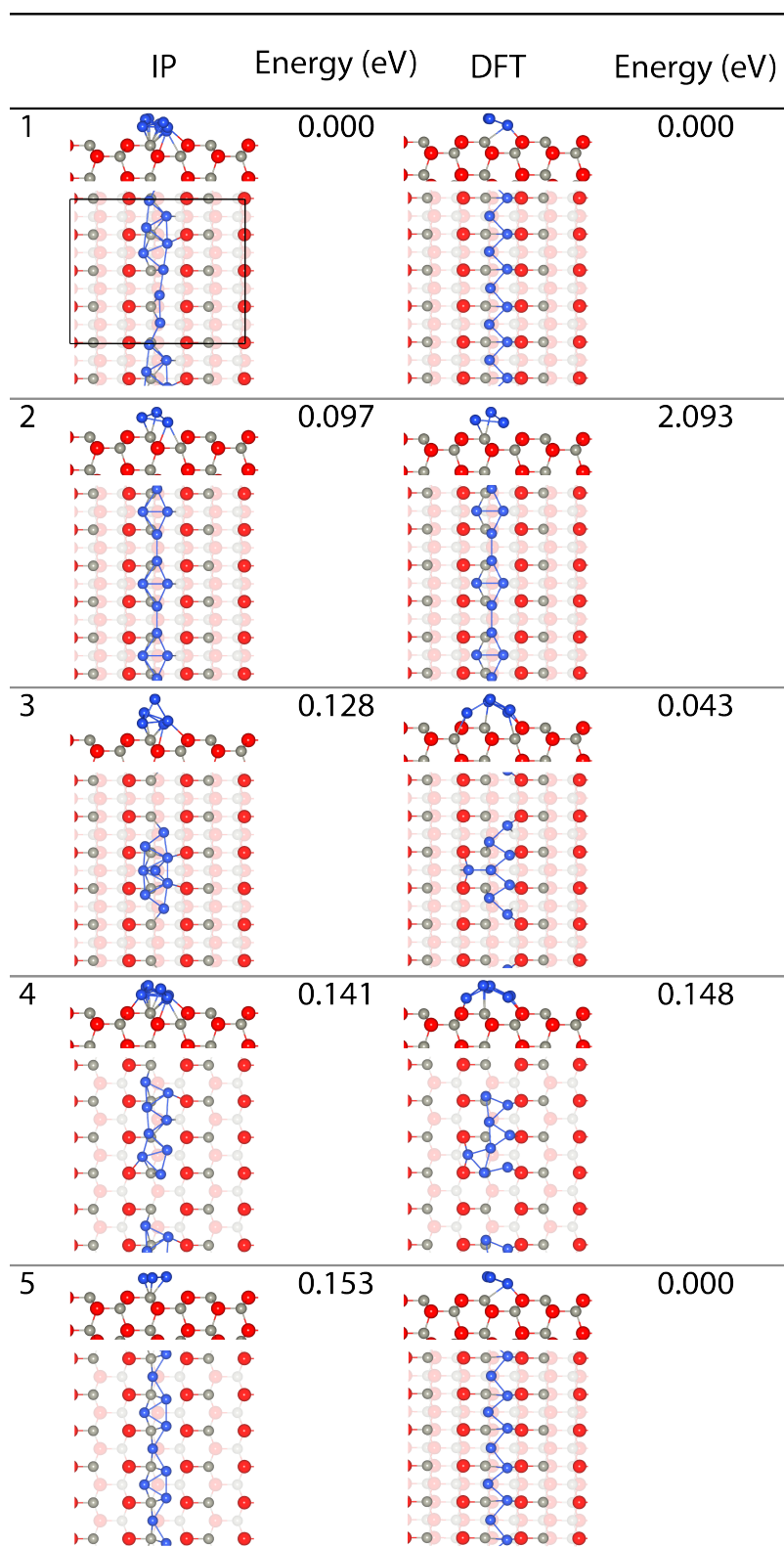


Figure 5.8 Top and side views of the five lowest energy structures from global optimisation. On the left, the structures predicted by our new Cu/ZnO set of potentials. On the right, the structures refined by DFT. Energies are with respect to the lowest energy structure on the respective energy landscapes. The (4×3) supercell is shown in the first structure.

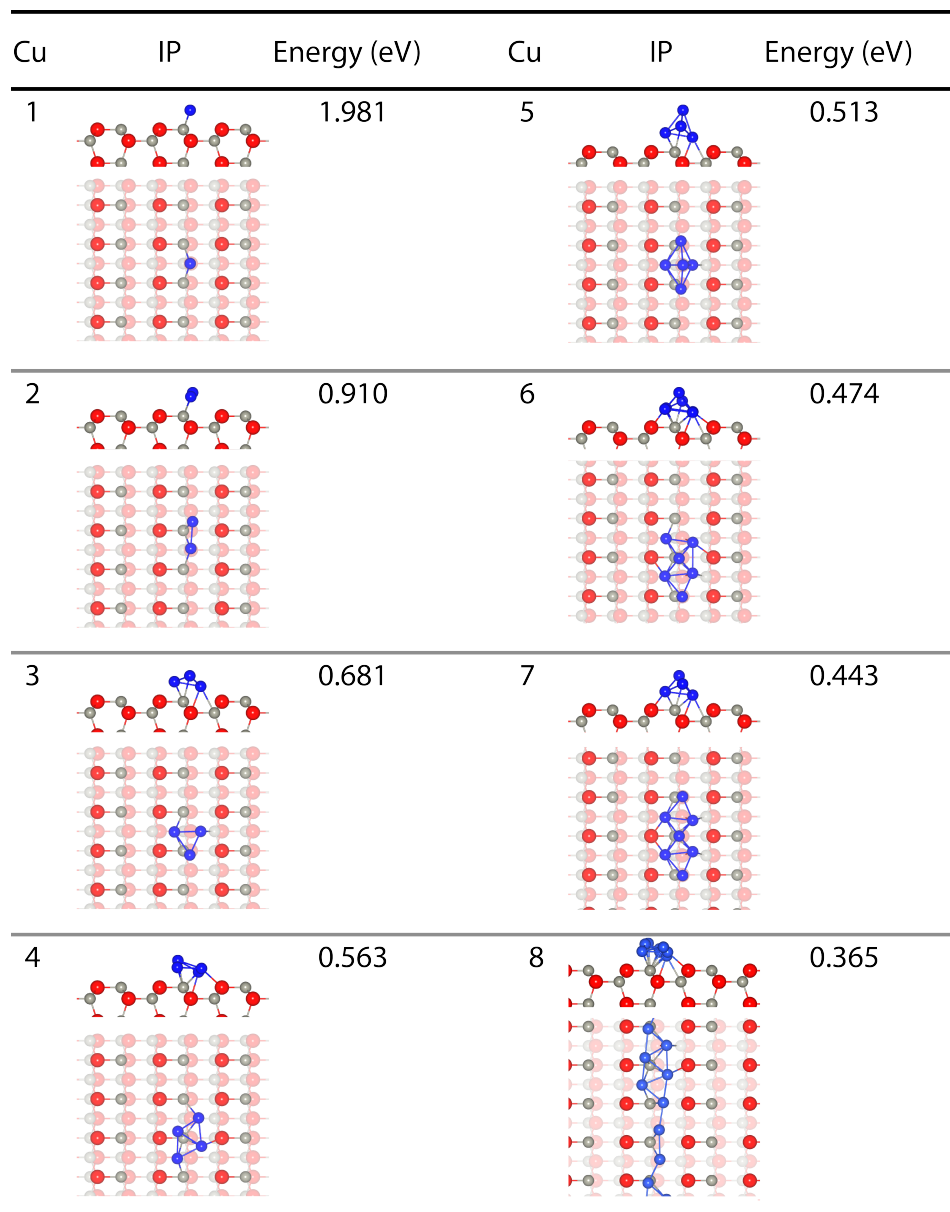


Figure 5.9 Top and side views of the global minima found of Cu_n clusters ($1 \leq n \leq 8$) deposited on the (4×3) $(10\bar{1}0)$ surface from global optimisation. The formation energy (using Cu_{metal} as a source of Cu) per Cu atom is displayed.

5.6 Summary and Conclusion

In this Chapter, we parameterised the force fields that describe the interactions between copper and zinc oxide. These IP were created with the aim of exploring the energy landscape of Cu clusters on ZnO surfaces. In order to obtain good Cu/ZnO IP, different aspects were taken into consideration such as: (i) bulk-like nonpolar ZnO surface terminations were used to allow a good description of the Cu-Zn interactions; (ii) planar Cu₄ clusters were employed to increase the accuracy and give a good balance between planar and non-planar clusters; (iii) Buckingham and Morse potentials gave a good description of the Cu-O and Cu-Zn interactions.

There is a strong agreement in the fit of the interatomic potentials to DFT SP calculations, which suggests that a good representation of the Cu/ZnO system is expected. We also show that the relaxation of the ZnO has no substantial effect on the optimised Cu₈ structures, which allow us to speed-up our calculations even further during the global optimisation.

Our global optimisation calculations found three structures lower in energy when compared to the optimised GM Cu₈ cluster on top of the (10 $\bar{1}$ 0) surface, with a difference of 0.32 eV with respect to the lowest (found twice) refined DFT Cu₈/ZnO energy structure.

In a structural comparison, a close similarity between IP and DFT calculations was achieved with a preference for *planar* Cu structures. In most of the cases, the DFT optimised structures were found in less than 40 ionic steps, whereas using the same computational resources and a GM Cu₈ cluster at 3 Å can take over 200 ionic steps. In conclusion, the new Cu/ZnO interatomic potentials proved to give a good structural agreement with DFT calculations.

Energetically, in general, a good agreement between IP and DFT structures was achieved. However, we observed a strong disagreement for the second lowest energy IP structure. This is related to the difference between energetic IP and DFT landscapes: the second structure is very close to a saddle point which is why its atomic arrangement does not change substantially, whereas the other four structures relax further. There is a small energetic IP-DFT mismatch, which is produced by

the combination of errors in the Cu-Cu and Cu-ZnO potentials. We note that the Cu-ZnO potentials were fit using only five parameters, which might produce a relatively simple IP, that is not sufficient to perfectly describe such a complex system.

In agreement with previous experimental and theoretical work, global optimizations of Cu_n clusters ($1 \leq n \leq 7$) deposited on the $(10\bar{1}0)$ surface show a preference for planar Cu clusters, with a strong interaction between the Cu and Zn species. Thus, exhibiting the strong influence of the ZnO substrate over the gas phase 3D Cu clusters.

5.7 Future Work

The work presented in this Chapter represents the first phase of this project. We have fitted and tested Cu/ZnO interatomic potentials, finding a good agreement between IP and DFT. In the next stage, we will be using the Cu/ZnO IP to study the Cu growth on the nonpolar ZnO surfaces. Firstly, we will address the stable structures of small Cu clusters on the nonpolar surfaces on terraces and steps (as seen in Chapter 3). Secondly, we will study bigger Cu clusters and investigate their stability on the steps edges as seen in STM images [148]. In the final stage, we will focus on the Cu crystal growth on the stable ZnO polar surfaces presented in Chapter 4.

Chapter 6

The MoO₃/Fe₂O₃ System

6.1 Introduction

In Chapters 3, 4 and 5, we have extensively described the structure and electronic properties of the four main low-index zinc oxide surfaces and their interaction with copper clusters. In this Chapter, we focus on the α -Fe₂O₃(0001) surface and its interaction with MoO₃ molecules.

The mineral form of iron (III) oxide, also known as hematite, has a corundum structure and is the most abundant and economically important source of iron in the world. Industrially, Fe₂O₃ is the main source of iron for the steel industry; it has a wide range of uses and applications including electronics (data storage disks), photocatalysis (water-splitting reaction), metallurgy (production of iron, steel and many alloys) and medicine (production of calamine). Moreover, one of the important uses of Fe₂O₃ is as a support in the MoO₃/Fe₂O₃ catalyst. The structure of the molybdate monolayer covered iron (III) oxide is of great importance due to its role in the synthesis of formaldehyde, which is an important industrial chemical produced by the catalytic oxidation of methanol. Among its applications, formaldehyde-based materials are the key in the production of resins, inks and wrinkle-free clothing. It is also used in drilling operations in petroleum industries and in 2012 the worldwide formaldehyde consumption exceeded 40.8 million tonnes [151]. There is a clear industrial need to understand the behaviour of the MoO₃/Fe₂O₃ catalyst which will be reflected in an improvement of the catalytic activity and a reduction of the pro-

duction cost.

In methanol oxidation, Fe_2O_3 is known to be completely unselective to formaldehyde [152, 153], whereas the $\text{MoO}_3/\text{Fe}_2\text{O}_3$ catalyst has been reported to have a very high selectivity to formaldehyde. Therefore, any formaldehyde selectivity in the $\text{MoO}_3/\text{Fe}_2\text{O}_3$ system can be attributed to the molybdenum at the material surface. This material is proposed to be present in commercial catalysts as an active Mo monolayer on top of ferric molybdate [154].

Usually, commercial iron molybdate catalysts are doped with an excess of Mo because the hot temperatures during reaction volatilizes it [155, 156]. The problem with this approach is that it creates multiple distinct phases including both MoO_3 and $\text{Fe}_2(\text{MoO}_4)_3$, which makes it difficult to assign the nature of the active site. Experimental XANES (X-ray absorption near edge structure) studies [154] have confirmed the presence of octahedral Mo units in 1 ML equivalents of Mo oxide onto the surface of Fe_2O_3 , whereas the EXAFS showed that these Mo units are bound to the Fe_2O_3 surfaces with clear Mo-Fe interaction. More information on the atomic structure of this material can be obtained with modelling techniques.

In this Chapter, we carried out *ab initio* calculations in the search for the most stable atomic structure for the clean Fe_2O_3 (0001) surface and MoO_3 supported (0001) Fe_2O_3 catalyst. All the calculations presented here were driven by experiments, our aim was to suggest a $\text{MoO}_3/\text{Fe}_2\text{O}_3$ atomic structure for the fitting of EXAFS parameters. Therefore, our analysis focuses mainly on MoO_3 adsorption energies and Mo-O and Mo-Fe bond lengths. Different adsorption sites were tested, with the lowest energy structure showing a good agreement with experiment.

6.2 Methods and Computational Details

6.2.1 Bulk Fe_2O_3

All the calculations presented in this Chapter were performed on the α - Fe_2O_3 corundum structure which has been shown to be the most thermodynamically stable form of iron oxide over a wide range of oxygen partial pressure including ambient conditions [157].

Calculations were carried out using spin-polarized DFT with the Vienna Ab initio Simulation Package (VASP) [47, 48], discussed in Chapter 2. The projector augmented wave (PAW) method [45, 49] was used to describe the core electrons together with the nuclei. In this formalism, eight valence electrons ($3d^7 4s^1$) for Fe atoms and six valence electrons ($2s^2 2p^4$) for O atoms were taken into account.

Due to the strongly localised Fe d electrons, the exchange-correlation energy was treated for on-site strong Coulombic interactions using the so-called DFT + U [158] approximation, which was introduced in Chapter 2. A value of $(U - J) = 4$ eV was applied to the Fe d states, which has been found to show optimal agreement between theory and experiment for a wide range of physical properties [159]. The GGA was chosen, which provides very good results for molecular geometries, binding energies, and ground-state energies. PBEsol functional [40] was used to deal with the gradient of the electron density. The PBEsol is an improvement of the Perdew-Burke-Ernzerhof (PBE) [39] functional as it achieves better results of equilibrium properties for densely-packed solids and their surfaces. Representative calculations have been strongly corroborated using higher-quality, smaller core pseudopotentials on metal ions.

The total energy was converged to 1 meV with respect to the k -mesh sampling and the plane wave cutoff. The Brillouin zone integration was described using Monkhorst-Pack grids [42]. Good convergence was achieved with a k -mesh of $16 \times 16 \times 16$ for the rhombohedral primitive cell and a plane wave cutoff of 500 eV. The iterative relaxation of the ions was carried out until the forces were below 0.01 eV \AA^{-1} .

6.2.2 Surface Models

All the calculations were done on the Fe-terminated $\text{Fe}_2\text{O}_3(0001)$ surface, which has been shown to be the most stable over a wide range of oxygen partial pressure [160]. The slab method was employed to describe surfaces within three-dimensional periodic boundary conditions.

The Fe_2O_3 polar surface (0001) was modelled by keeping fixed the three lattice parameters and middle slab atoms, whereas all other ions were allowed to relax. The

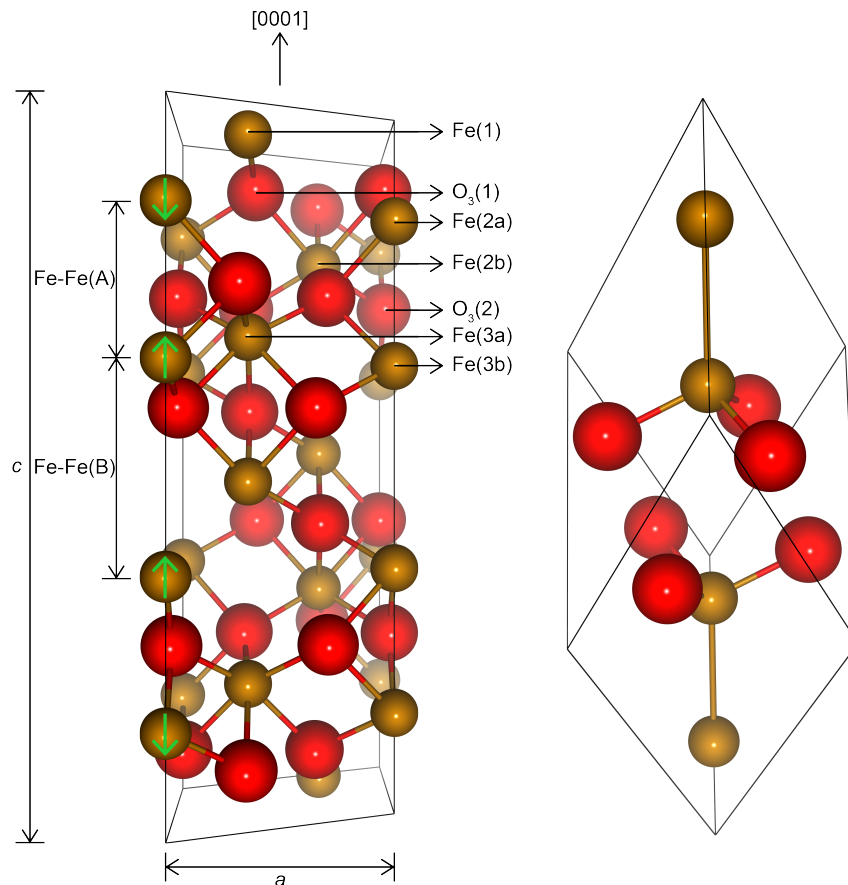


Figure 6.1 Hexagonal unit and primitive cells of α - Fe_2O_3 . Both lattice parameters and interplane distances Fe-Fe(A) and Fe-Fe(B) are shown. The anti-ferromagnetic arrangement is indicated with green arrows. Red and brown spheres represent oxygen and iron ions, respectively.

surface energy (E_{surf}) was converged to 1 mJ/m^2 with respect to the thickness of the slab and the k -mesh sampling. Convergence was achieved with a slab containing thirteen Fe_2O_3 layers (65 atoms) and a k -mesh of $6 \times 6 \times 1$. A denser grid of $10 \times 10 \times 1$ does not show substantial changes in the surface energy. The cutoff energy was kept as in the bulk and a vacuum space greater than 18 \AA was used. All the surfaces were built with symmetry to avoid dipole moments.

6.2.3 MoO_3 Adsorption

Five different initial MoO_3 adsorption sites were tested on the most stable (0001) surface of α - Fe_2O_3 , which are represented in a (1×1) cell in Figure 6.2. To aid experimental site characterisation, we have run a series of *ab initio* plane-wave cal-

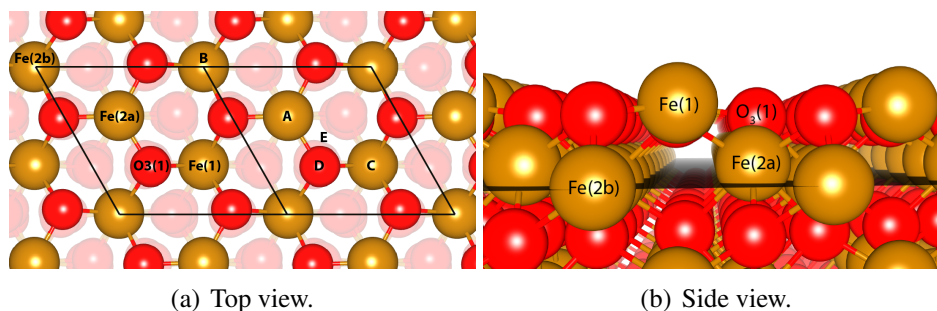


Figure 6.2 Top and side view of the α - $\text{Fe}_2\text{O}_3(0001)$ surface. Different initial adsorption sites (from A to E) for the MoO_3 molecule are shown; the rhomboids represent the surface unit cell. The drawn plane marks the position of the semi-transparent oxygen ions showed in the left picture.

culations using (1×1) and (2×2) surface models, with a MoO_3 neutral unit added to each of the candidate sites at *ca.* 3 \AA away from the surface, which would correspond to 0.5 and 0.25 ML MoO_3 surface coverage, respectively, considering only the uppermost cationic layer. Close-range MoO_3 - MoO_3 interactions have thus been avoided in agreement with EXAFS data, where the primary Mo octahedral environment is associated with the Mo-O scattering paths followed by Fe neighbours (after 2 \AA). We note that our approach to the problem of global optimisation of the MoO_3 overlayer does not aim to mimic the real experimental synthetic conditions, but proves to be useful in establishing the interface structure.

In order to evaluate the MoO_3 load and the MoO_3 - MoO_3 interaction, different cell sizes were evaluated: (2×2) , (2×1) and (1×1) . In the (2×2) and (2×1) surfaces, just one MoO_3 unit was adsorbed on the surface, whereas in the (1×1) till two MoO_3 units were adsorbed. Simulations of the formation of the MoO_3 overlayer on Fe_2O_3 were performed identically on both sides of the slab to ensure that the slab dipole moment perpendicular to the surface was zero. A $+U_{eff}$ correction of 6.3 eV was applied to the Mo d states, as proposed by Coquet and Willock [161].

The calculations presented here were driven by experimental findings and our aim was to get the lowest energy structure which matched EXAFS bond lengths and coordination numbers with respect to the adsorbed Mo atom.

6.3 Fe₂O₃ Bulk

Hematite has a rhombohedral, corundum structure with an octahedral coordination geometry and experimental lattice parameters $a = b = 5.035\text{\AA}$ and $c = 13.72\text{\AA}$ [13]. To reproduce the inherent antiferromagnetic character of the α -Fe₂O₃ material, we performed a set of calculations using different stacking spin-up and spin-down sequences in the primitive cell. We tested the three different possible antiferromagnetic sequences: $++--$, $+--+$ and $+-+-$. In agreement with previous reports [159, 160, 162], the magnetic ground state was found to be represented by $++--$ sequence. The latter means that along the c axis, there are two different types of Fe ions: type A ions (short distance) that have opposite magnetic moments, and type B ions (larger distance) that have equal magnetic moments (see Figure 6.1).

The corresponding structure and magnetic moments of the α -Fe₂O₃ magnetic ground state are represented in Table 6.1. The calculated lattice parameters a and c and the c/a ratio show a good agreement with previous calculations and experimental data [159, 160, 163–165]. When compared to experiment, the lattice parameters a and c are within *ca.* 0.48% and 0.24% deviation, respectively, whereas the c/a ratio is only 0.22% larger. Additionally, interplanar distances Fe-Fe(A) and Fe-Fe(B) are calculated to be *ca.* 1.30% smaller and *ca.* 0.52% greater than in experiment. The magnetic moment computed was *ca.* $4.13\mu_B$, which is *ca.* $0.77\mu_B$ below the experimental value ($4.6 - 4.9\mu_B$).

Table 6.1 Experimental and Theoretical Structural Parameters for the Hematite Bulk Structure. Distances Are Given in \AA .

	a	c	c/a	Fe-Fe(A)	Fe-Fe(B)	μ_B/atom
This study	5.008	13.705	2.736	2.852	4	4.13
GGA/PZ81[160]	5.007	13.829	2.772	2.929	3.998	3.45
GGA + U/PZ81[160]	5.067	13.882	2.739	2.896	4.044	4.11
GGA/FP-LAPW[166]	5.025	13.671	2.721			3.39
Exp.[165]	5.029	13.73	2.730	2.883	3.982	4.6-4.9
Exp.[163]	5.035	13.747	2.730	2.896	3.977	

6.4 Surface Structure

As mentioned in Section 6.2.2, the most stable surface for the α -Fe₂O₃ over a wide range of temperature and pressure is the (0001) termination, which has, however, different possible atomic terminations. The stability of these terminations has been studied previously by experiment and theory. Experimental scanning tunnelling microscope (STM) studies [166, 167] presented evidence of the coexistence of two different terminations (oxygen and iron) on the (0001) surface under oxygen pressures. Both studies show STM images with hexagonal lattices and a periodicity of *ca.* 5 Å, which is compatible with the interlayer distance between (0001) Fe layers in the corundum structure. However, the STM images by Chambers and Yi [168] show the surface to be purely iron terminated. Therefore, depending on the preparation method, the termination of the (0001) surface can be either a combination of iron and oxygen terminated surfaces or creates uniquely iron terminated surfaces. On the other side, Rohrbach et al. [160] conducted an *ab initio* computational study on five possible terminations of the α -Fe₂O₃ (0001) surface: three oxygen terminated and the two iron terminated: — Fe₂O₃, — FeO₃ - Fe₃O₃, — Fe₂O₃ - O, — Fe₂O₃ - Fe₂ and — Fe₂O₃ - Fe. They reported a — Fe₂O₃ - Fe termination (Figure 6.1) as the most stable at a wide range of oxygen partial pressures. The oxygen-terminated surfaces are strongly disfavoured because of the increased energetic cost of stabilising a higher oxidation state of the transition metal close to the surface [160]. Following these conclusions, we decided to focus our calculations on the —Fe₂O₃-Fe termination of the α -Fe₂O₃ (0001) surface.

Table 6.2 shows the relative Fe-O and Fe-Fe relaxations of the first three monolayers on the (0001) α -Fe₂O₃ surface. Generally, we calculated strong contraction of the slab size which is in agreement with previous theoretical works on corundum-type materials such as Cr₂O₃ and α -Al₂O₃ [160]. No atomic lateral displacements were observed in our models. Our results show a great relaxation of the first interlayer Fe-O distance of 73% while previous theoretical results show a relaxation of 53% [160] and 57% [160, 164, 166]. We attribute the larger relaxations to the PBEsol functional, which, as noted, is a revised version of the PBE functional and

provides better structural results for solids. We note that, in our calculations, the bulk interlayer Fe-O and Fe-Fe distances are 0.86 Å and 0.57 Å, whereas a recent STM study [167] found that these distances are 0.85 Å and 0.60 Å for the Fe-Fe and Fe-O, respectively. The other relaxations also show very good agreement with previous results. The large Fe-O relaxations in the first two layers is an electrostatic effect, characteristic of this polar surface [160].

Table 6.2 Relative Interlayer Distances on α -Fe₂O₃(0001) Surface. All the Values Below Are Given as a Percentage with Respect to Bulk Interlayer Fe-O (0.568 Å) and Fe-Fe (0.858 Å) Distances Along the *c* Axis. For the Nomenclature Used, See Figure 6.1.

	GGA + <i>U</i>	GGA[160]	GGA + <i>U</i> [160]	GGA[166]	GGA[164]
Fe(1)-O ₃ (1)	-72.8	-53.0	-57.0	-57	-57.8
O ₃ (1)-Fe(2a)	7.2	22.0	9.6	7	3.5
Fe(2a)-Fe(2b)	-37.5	-31.0	-40.0	-33	-74.0
Fe(2b)-O ₃ (2)	16.3	34.0	17.0	15	15.9
O ₃ (2)-Fe(3a)	4.7	2.5	3.5	5	4.0
Fe(3a)-Fe(3b)	-5.5	-9.8	-4.4	-3	30.0

6.5 MoO₃ Adsorption

Due to their importance in catalysis, the (0001) surface of α -Fe₂O₃ and its interaction with adsorbed molecules have been the subject of intensive experimental and theoretical studies [159, 160, 164, 169–171]. However, despite its importance, there are no previously reported computational studies of adsorbed MoO₃ molecules on Fe₂O₃ surfaces.

On geometry optimisation (see Figure 6.3), we observed that whenever the Mo ion was placed just above a surface oxygen (adsorption site D), it moved off this site and stabilised above the Fe ion of the second (subsurface) layer adopting either configuration A or B illustrated in the figure and described in greater detail described below. With a surface interstitial site E as a starting point, the Mo ion relaxed weakly towards the surface as one of the molybdate O ions is displaced towards the top Fe layer Fe forming a Mo-O-Fe bridge. The adsorption site C proved to be highly unfavourable; the Mo ions stayed above the uppermost Fe atom with no

strong Mo relaxation; the neutral MoO₃ monolayer remained nearly flat at a non-bonding distance above the surface. At sites A and B, we observed an especially strong Mo relaxation into the surface where it adopts an octahedral coordination (Figure 6.4): at the most stable site A, Mo has one neighbour Fe ion at 2.80 Å and three at 2.96 Å, whereas at site B it has three Fe neighbours at 2.94 Å and one at 3.05 Å (Table 6.3). Coordination numbers and bond lengths on site A were confirmed with the more accurate hybrid PBEsol0 functional using a computationally less expensive 7 layer slab (Table 6.3). Thus, we could identify the lowest energy adsorption site for the molybdenum. This site agrees with the coordination numbers in the EXAFS analysis and shows a good agreement with most of the bond distances. Moreover, this theoretical model agrees with the Fe exposure suggested at the surface for the 1 ML catalysis, see site A in Figures 6.2 and 6.3. Comparing the structural parameters of Mo from EXAFS and theory, the calculations using the (2 × 2) surface model predict the three short Mo-O bond distances to be 3.44% greater and the Fe-O distances 1.4% and 3.59% smaller. However, our calculations yield the three long Mo-O bond distances 14.87% greater than experiment; Table 6.3 gives a comparison of the bond distances and coordination number of the different adsorption sites and EXAFS results. This discrepancy could be expected due to the structural disorder in the position of Mo ions on the surface, where at the experimentally observed 0.14 ML coverage, Mo can occupy a number of alternative energetically most favourable A sites, but also less favourable but kinetically accessible B sites.

Table 6.3 Mo-O, Mo-Fe Distances (Å) and Adsorption Energies of the Relaxed MoO₃/Fe₂O₃ Structures. The Coordination Number is Shown in Parenthesis. DFT + *U* and EXAFS Experimental Data Are Displayed.

	(1 × 1) Surface			(2 × 2) Surface	Hybrid	EXAFS
	Site A	Site B	Site C	Site A	Site A	
Mo-O	1.77 (x3)	1.77 (x3)	1.74 (x3)	1.80 (x3)	1.75 (x3)	1.74 (x3)
	2.24 (x3)	2.21 (x3)		2.18 (x3)	2.23 (x3)	1.95 (x3)
Mo-Fe	2.80 (x1)	2.94 (x3)	2.70 (x1)	2.81 (x1)	2.81 (x3)	2.85 (x1)
	2.96 (x3)	3.05 (x1)		2.99 (x3)	2.95 (x3)	3.10 (x3)
<i>E_b</i> (eV)	-4.850	-4.553	-0.288	-6.316		

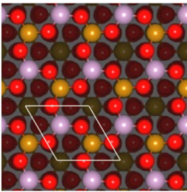
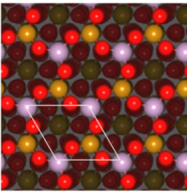
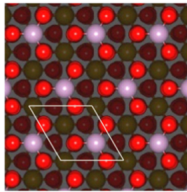
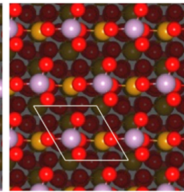
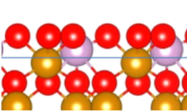
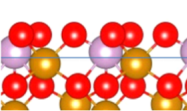
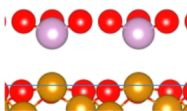
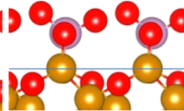
Adsorption site	A	B	C	E
View along the hexagonal axis				
Side view				
Energies (kJ/mol)	0	29	440	81

Figure 6.3 Relaxed structures for the different adsorption sites. Energies based on (1×1) surface calculations. The relaxed structure for the adsorption site D is not shown since it adopts either structure A or B. Red, brown, and violet spheres denote oxygen, iron, and molybdenum, respectively. The rhombohedron represents the surface unit cell. Energies are in kJ/mol.

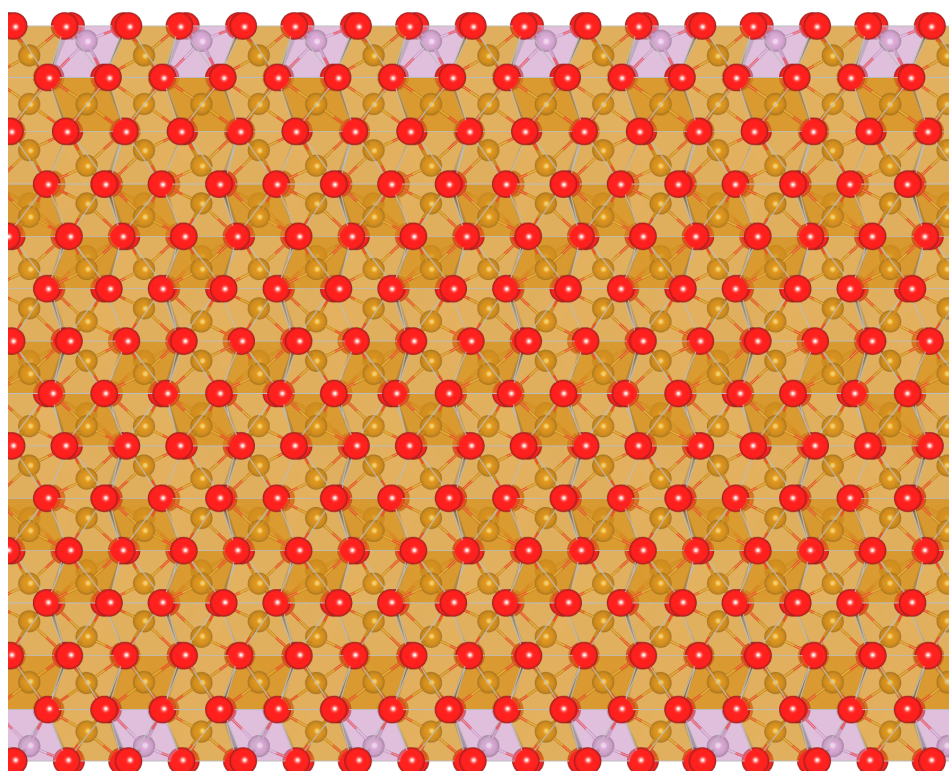


Figure 6.4 Side view of the polyhedral representation of the lowest energy MoO_3 adsorbed on a thirteen- Fe_2O_3 -(0001)-layer surface.

6.6 Further Refinement

In the search for better agreement with experiment with respect to the long-range Mo-O distance, we ran a series of calculations based on the most stable A and B sites. Different approaches were tested including bigger supercells, hydroxylated terminations, substitution of Fe ions for Mo and the use of higher-quality, smaller core pseudopotentials on metal ions. In all these calculations, the slab charge was kept neutral and the Fe_2O_3 stoichiometry was conserved. As described in Section 6.2.2, models were built by symmetry on both terminations of the slab, thus, avoiding the creation of a dipole moment.

Supercell and Hydroxylated Surfaces

We did not observe significant changes when the cell size is increased to (2×2) and (3×3) . Minor changes in the bond lengths were seen and the molybdenum kept its octahedral environment. With these observations, we can conclude that the Mo-Mo interaction between cell images is so small that it can be neglected.

As mentioned in Chapter 3 and 4, metal oxide surfaces are usually in contact with water and its dissociated molecules (H, O and OH). In this section, we analysed the effect of hydrogen and water molecules in the Mo-O and Mo-Fe bond lengths. Six H_2 molecules were added to the two lowest energy structures (sites A and B), e.g. 3 H atoms symmetrically equivalent on each side of the slab. These ions were placed on top of the topmost oxygens (oxygens from the MoO_3 molecule). Figure 6.5 shows the initial and optimised structures of the two lowest energy structures with hydroxylated surfaces. Results show a bigger discrepancy with EXAFS data (see Figure 6.5 and Table 6.4). In the hydroxylated surfaces, Mo atoms keep an octahedral environment, having, for site A, 6 oxygen atoms at *ca.* 2.02 Å and for site B, 3 oxygens at 1.95 Å and 3 at 2.03 Å. We also note a substantial shrinkage of the Mo-Fe bond lengths for both cases. The adsorption of a water molecule was tested as well, with no better agreement with the EXAFS data. We conclude that hydroxylated surfaces are not an answer to describe the Mo-Fe and Mo-O EXAFS bond lengths.

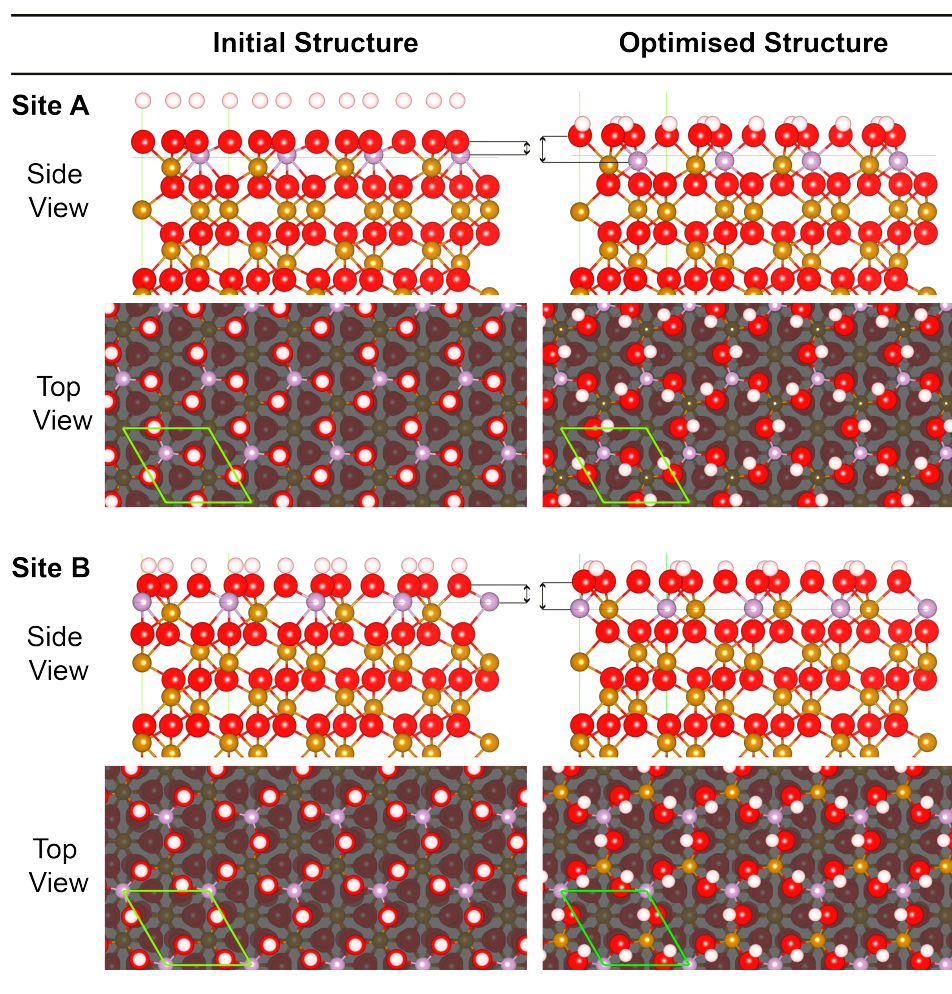


Figure 6.5 Side and top views of the two lowest energy $\text{MoO}_3/\text{Fe}_2\text{O}_3$ structures. Structures before and after hydroxylation are shown. White spheres represent hydrogen. The rhombohedron represents the surface unit cell.

Table 6.4 Mo-O, Mo-Fe Distances (\AA) of the Relaxed Hydroxylated $\text{MoO}_3/\text{Fe}_2\text{O}_3$ Structures. Coordination Number Is Shown in Parenthesis. For Comparison with Experiments See Table 6.3.

	Site A + 3H ₂	Site B + 3H ₂	Site A + 1H ₂₀
Mo-O	2.01 (x3)	1.95 (x3)	1.79 (x3)
	2.03 (x3)	2.03 (x3)	2.19 (x3)
Mo-Fe	2.41 (x1)	2.68 (x1)	2.80 (x1)
	2.90 (x3)	2.89 (x3)	2.93 (x1)
			3.03 (x2)

Extra MoO₃ and Ionic Substitution

As mentioned in Section 6.4, different atomic terminations are allowed for the (0001) α -Fe₂O₃ surface. Depending on synthesis conditions, the surface can be either oxygen or iron terminated [160, 166–168]. Based on this, we decided to build two surface models with modifications to the lowest energy site A structure: (i) adding an extra MoO₃ molecule on top of the Fe(2b) (see Figure 6.2); and (ii) exchange Mo and topmost Fe positions. Modifications were done on both sides of the slab. Figure 6.6 shows the initial and optimised structures of the two modified surfaces and Table 6.5 displays the Mo-O and Mo-Fe distances. When adding an extra MoO₃ molecule, the surface expands and the Mo-O short range bond length increases. There is also a decrease in the Mo-Fe and Mo-O long range distances. The second Mo atom also has an octahedral coordination, with no Fe atoms within 3 Å. In the model produced by an ionic Mo-Fe exchange, the structure does not show an improvement in fitting to the EXAFS parameters. In this case, the Mo-Fe coordination number changes, moving further from the EXAFS data. Despite all the efforts, a better agreement with the long-range Mo-O distance could not be achieved. We conclude that our original model is adequate with the remaining discrepancy due to structural and dynamic disorder.

Table 6.5 Mo-O, Mo-Fe Distances (Å) of the Relaxed MoO₃/Fe₂O₃ and 2MoO₃/Fe₂O₃ Structures. Coordination Number Is Shown in Parenthesis. For Comparison with Experiments See Table 6.3.

	Site A + MoO ₃	Ionic Mo-Fe exchange
Mo-O	2.02 (x3)	1.80 (x3)
	2.13 (x3)	2.16 (x3)
Mo-Fe	2.52 (x1)	2.89 (x3)
	2.91 (x3)	
Mo-O (2nd O)	2.03 (x3)	
	2.43 (x3)	

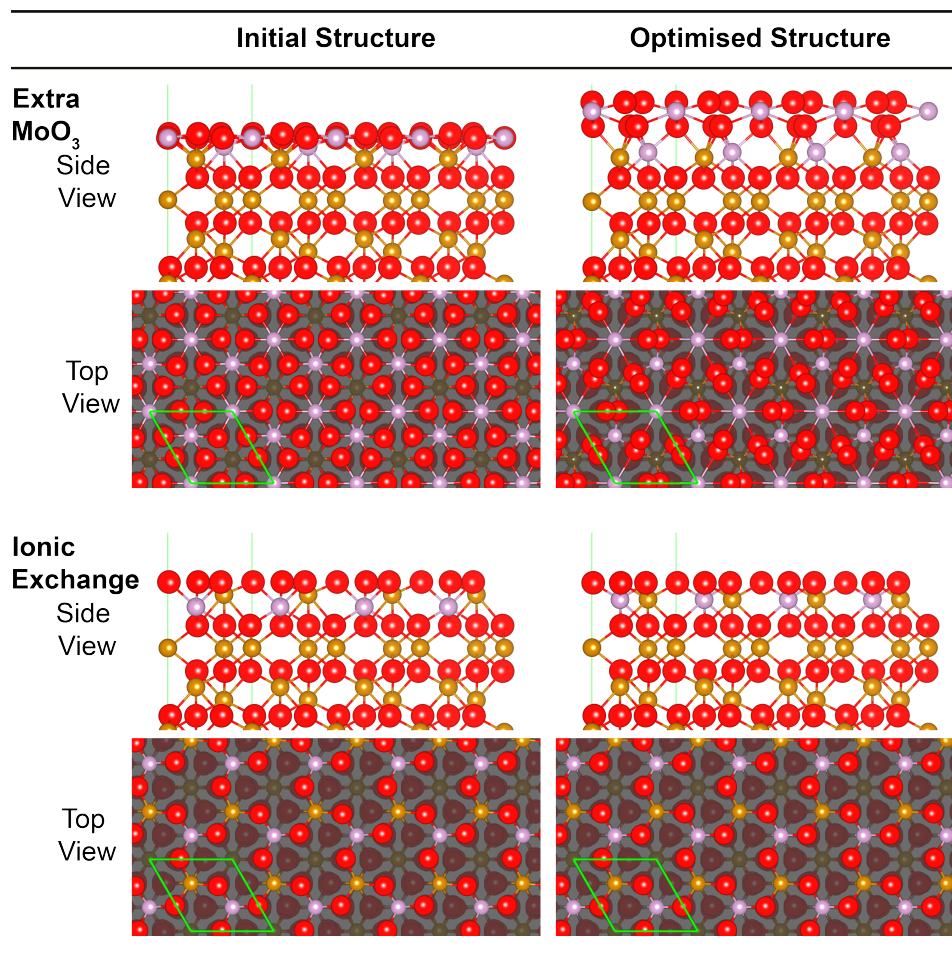


Figure 6.6 Side and top views of the two modifications to the lowest energy site A structure: (i) an extra MoO₃ on top of the Fe(2b) (see Figure 6.2) and (ii) exchange Mo and topmost Fe positions. The rhombohedron represents the surface unit cell.

6.7 Summary and Conclusions

We have presented a detailed analysis on the structural properties of different MoO₃ adsorption sites on the (0001) α -Fe₂O₃ surface as an alternative tool in the fitting of EXAFS parameters. We have shown that the GGA + U shows a good agreement with the experimental Fe₂O₃ structure, thus, giving us confidence on the results presented here.

From the five different starting points (sites A-E), we conclude that adsorption site D tends to stabilise adopting either the optimised configuration A or B. In the surface interstitial site E, the Mo ion relaxed weakly towards the surface as one of the molybdate O ions displaced towards the first layer Fe forming a Mo-O-Fe

bridge. The adsorption site C proved to be highly unfavourable. Sites A and B show a strong Mo relaxation towards the Fe_2O_3 surface adopting an octahedral coordination. The slightly more stable A site presents the best agreement in the fitting of EXAFS parameters and shows a good agreement with most of the bond distances. In this site, the Mo would have an octahedral coordination with 6 O neighbours: three short range at *ca.* 1.77 Å and three long range at *ca.* 2.24 Å. Fe atoms are also present at relatively short distances from the Mo atoms: three Fe neighbours at around 3 Å and one Fe neighbour at a shorter distance. The long range Mo-O distance discrepancy is probably due to the structural disorder in the position of Mo ions on the surface, where at the experimentally observed 0.14 ML coverage, Mo can occupy a number of alternative energetically most favourable A sites, but also less favourable but kinetically accessible B sites.

In an attempt to improve the larger discrepancy at the long range Mo-O distance, we ran a series of calculations based on the two most stable sites A and B. None of our attempts showed an improvement in the long range Mo-O distance. We only calculated very small improvements when a (2×2) or (3×3) supercell was used. Hydroxylated surfaces proved to elongate the short range Mo-O distance and shrink the long range Mo-O and Mo-Fe distances. Neither the addition of a MoO_3 molecule nor the ionic Mo-Fe exchange provided an improvement. We conclude that our original model provides a good basis for describing the surface structure of the Fe_2O_3 .

Chapter 7

Summary and Conclusions

In this Chapter, the results of this Thesis are summarised and suggestions for future work are presented. We have shown that computer modelling techniques are a powerful tool in studying the surface sciences of oxides. They provide an insight into the materials investigated on an atomic-scale, helping to clarify the materials' structure and the findings observed in experiment. In the work presented, we have used interatomic potential and *ab initio* methods to provide a better understanding of both the atomic structure and electronic properties of metal oxide surfaces. Our focus has been on the four main low-index surfaces of the wurtzite phase of ZnO, while one Chapter has been dedicated to iron oxide.

In the first section of results (Chapter 3) we provided a detailed report on the atomic structure and electronic properties of nonpolar ZnO surfaces: $(10\bar{1}0)$ and $(11\bar{2}0)$, with the goal of providing a conclusive statement about the atomic structure of such surfaces. These ZnO terminations show higher emission efficiency for blue and ultra-violet LEDs. In addition, they represent the biggest surface area of ZnO crystals. Three levels of theory were used in the first section of this dissertation: IP, DFT and hybrid DFT. Our calculations confirm earlier GGA and experimental reports on the cationic termination for both nonpolar surfaces, with lateral displacements for both species on the $(11\bar{2}0)$ surface. A slightly higher stability of the $(10\bar{1}0)$ surface was calculated, indicating an almost equal prominence for both surfaces under thermodynamical equilibrium. The larger surface area of the $(10\bar{1}0)$ surface observed in experiment suggests the importance of thermal vibrational con-

tributions to the free energy, which could determine the crystal morphology, or of the kinetic crystal growth factors.

According to experimental observations, steps are an unavoidable feature in the nonpolar surfaces of ZnO. We calculated the energy required to create a step along the [010] direction on the $(10\bar{1}0)$ surface as $0.029 \text{ eV}/\text{\AA}$ (at the DFT level), thus, suggesting the existence of this feature even at room temperature (kT is 0.025 eV). Our IP calculations also agree with this high stability.

Electronically, we calculated a ZnO bulk ionisation potential as *ca.* 7.6 eV using hybrids, in agreement with the experimental value of 7.82 eV . The method used in this Thesis showed an improvement of about 1 eV when compared with the widely used “slab alignment” method. We found that the effect of surface features (steps and grooves) is not strong on the ionisation potential (a decrease of *ca.* 0.04 eV when compared to bulk). However, a 25% dimer vacancy formation reduces the ionisation potential by 0.13 eV . We observed that the band gap as a function of the slab model thickness converges much slower than both the atomic structure and surface energies. The slow convergence could be attributed to quantum confinement effects. The electronic band edges of the nonpolar surfaces are seen to behave markedly differently, with a local rise of the VBM and CBM for $(10\bar{1}0)$ and $(11\bar{2}0)$, respectively. The rest of the bands remained flat.

After the detailed description provided for the nonpolar ZnO surfaces in the third Chapter, we continued with the other two characteristic terminations: the polar zinc and oxygen terminated faces. These polar surfaces are required to explain the stability of ZnO crystals. In addition, these terminations are linked strongly to profitable chemical processes, such as methanol synthesis, photocatalysis, and hydrogen gas sensitivity. For the polar surfaces of ZnO, we engaged in a detailed study of their stabilisation mechanism, using interatomic potential methods. Our results can explain why experimental findings reported have been varied and even contradictory at times. The results presented here demonstrate the importance of completely cancelling the inherent dipole moment present in these surfaces. The calculated surface energies indicate on average a slightly higher stability of the

oxygen terminated surface over the zinc termination, which implies that under thermodynamic equilibrium the $(000\bar{1})$ surface will be more expressed. The change of surface energy as a function of the stoichiometry among the stoichiometries on the Zn terminated side is stronger than in the O side. Thus, it is expected that, on the $(000\bar{1})$ -O surface there will be a higher number of stoichiometries that are equally stable than on the (0001) surface, which is in agreement with experiment, in which it has been easier to identify reconstruction patterns in the Zn termination. Our calculations suggest that the common (1×1) periodicity seen in experiment is a result of the degree of disorder. We also demonstrated that the stoichiometries would be represented mainly by their GM and that for the cases where more structures are thermally accessible, a similar pattern is expected.

Our structural analysis shows that the (0001) and $(000\bar{1})$ surfaces also behave differently. In the zinc termination, there are strong movements across with some Zn ions from the second layer jumping to the first layer; whereas in the O terminated side an ionic transfer across layers only happens at high stoichiometries ($m_O > 19$). Triangular reconstructions are seen on both surfaces; however, stripes and random vacancies are also stable. Hexagonal patterns are also observed in the oxygen terminated face. Our calculated triangular and hexagonal patterns agree with experiment. Based on our findings, we conclude that triangular and hexagonal patterns are not the only stable ones; we predicted a high level of disorder, with reconstruction patterns as a function of the synthesis procedure and conditions.

In the third section of results in Chapter 5, we studied the Cu/ZnO system using interatomic potential methods. Cu particles over ZnO surfaces are of great interest in the chemical industry, in which they are used for the production of methanol (estimated to be 65 million tonnes per year in 2013). New IP were created to explore the energy landscape of Cu clusters on ZnO surfaces with the use of global optimisation techniques. A combination of Buckingham (Cu-O) and Morse (Cu-Zn) potentials were fitted to DFT SP calculations. Our atomistic model shows a good agreement with DFT SP calculations, suggesting a good description of the Cu/ZnO system.

The new Cu/ZnO potentials were used in global optimisation calculations of eight copper atoms on the (10 $\bar{1}$ 0) surface. After the DFT refinement of the lowest five IP atomic structures, three DFT structures were found lower in energy than an optimised GM Cu₈ cluster on top of the (10 $\bar{1}$ 0) surface. The highest difference of 0.32 eV was found between the GM Cu₈/ZnO and the global optimised Cu₈/ZnO, showing that our approach and IP can find lower energy structures successfully. Thus, our new IP can work as a fast and reliable method to filter sensible Cu/ZnO structures, which could be refined by DFT methods afterwards.

Structurally, the new Cu/ZnO interatomic potentials agree with DFT calculations. We calculated a preference for *planar* over 3D Cu structures. Moreover, using the same computational resources, our technique proved to be efficient and produced IP structures close to the optimised DFT structures: The DFT ionic steps were reduced by 80% (in most of the cases) when compared with a GM Cu₈ cluster at 3 Å.

Energetically, new IP and DFT calculations produce similar results, with the exception of one structure. One of the IP structures shows a strong disagreement with DFT. The second lowest IP energy structure is close to the DFT saddle point, relaxing by only 0.6 eV with no substantial changes in the atomic arrangement, whereas the remaining four IP structures change their structures slightly, with energetic changes of the order of 2 – 3 eV after the DFT refinement. Moreover, small discrepancies between IP and DFT are expected from the combination of errors in the Cu-Cu and Cu-ZnO potentials. We should note that our Cu/ZnO potentials are relatively simple and might not be expected to perfectly describe the DFT landscape.

The new Cu/ZnO potentials created were used to run global optimisations of Cu_{*n*} clusters ($1 \leq n \leq 7$) deposited on the (10 $\bar{1}$ 0) surface. Results show a preference for planar Cu clusters, with a strong interaction between the Cu and Zn species, thus, exhibiting the strong influence of the ZnO substrate over the gas phase 3D Cu clusters.

The last section of results, Chapter 6, was dedicated to the MoO₃/Fe₂O₃ cat-

alytic system. This material is industrially used in the production of formaldehyde through the oxidation of methanol. In this reaction, the formaldehyde selectivity is attributed to the molybdenum at the material's surface. Therefore, we investigated the MoO₃ adsorption on the (0001) α -Fe₂O₃ surface using DFT + *U*. This study was suggested following experimental findings and was realised with the aim of helping in the fitting of EXAFS parameters by suggesting a MoO₃/Fe₂O₃ atomic structure. The most stable configuration found shows a strong Mo relaxation towards the Fe₂O₃ surface adopting an octahedral coordination. This structure presents the best agreement in the fitting of EXAFS parameters and a good agreement with most of the bond distances: The Mo atom would have an octahedral coordination with six O neighbours. Four Fe neighbours would also be present at larger distances. The latter model presents a variation in the Mo-O long-range distance of about 0.23 Å. The discrepancy can be expected due to the structural disorder in the position of Mo ions on the surface, where at the experimentally observed 0.14 ML coverage, Mo can occupy a number of kinetically accessible sites. Further possibilities were tested such as larger supercell sizes, hydroxylated surfaces and extra MoO₃ molecules. However, only the larger (2 × 2) supercell size showed a very small improvement in the long-range Mo-O distance.

In summary, we have provided a detailed structural and electronic description of the nonpolar ZnO surfaces. Morphological features on the most stable ZnO termination were also studied. Regarding the polar surfaces, we have explained their stability and provided an explanation for the divergent experimental findings reported in the literature. Moreover, we have created a new set of interatomic potentials to describe the Cu/ZnO system, with which we analysed the Cu growth on the (10 $\bar{1}$ 0) ZnO surface. In addition to the ZnO surfaces, we studied the MoO₃/Fe₂O₃ system to help with the fitting of experimental data.

This Thesis has only considered Cu cluster growth on the most stable (10 $\bar{1}$ 0) ZnO surface. However, the way in which copper grows on the nonpolar (11 $\bar{2}$ 0) and polar (0001) and (000 $\bar{1}$) surfaces is poorly understood. Therefore, studying the Cu crystal growth on the (11 $\bar{2}$ 0), (0001) and (000 $\bar{1}$) surfaces would be of particu-

lar interest in the future. Our new Cu/ZnO potentials represent a first step in this direction. In the future, we will address the stable structures of small Cu clusters on the other three ZnO surfaces, as well as on terraces and steps (as presented in Chapter 3). Our aim is to corroborate experimental STM findings of big Cu clusters decorating the step edges on the $(10\bar{1}0)$ surface. In addition, we would like to study the further stabilisation of the polar ZnO surfaces by using bigger supercell size models.

In this Thesis, we presented high-quality calculations and efficient methods to study the surface science of metal oxides, providing answers to poorly understood surface features and giving new tools for the study of adsorbate-surface interactions. There is a clear industrial need to improve and understand the behaviour of metal oxide surfaces due to their wide range of profitable uses and applications. A small contribution to their understanding will have a major impact on industrial processes and on the relevant surface science.

Bibliography

- [1] R. Swank, "Surface properties of II-VI compounds," *Phys. Rev.*, vol. 153, no. 3, pp. 844–849, 1967.
- [2] A. Mang, K. Reimann, and S. Rübénacke, "Band gaps, crystal-field splitting, spin-orbit coupling, and exciton binding energies in ZnO under hydrostatic pressure," *Solid State Commun.*, vol. 94, no. 4, pp. 251–254, 1995.
- [3] D. C. Reynolds, D. C. Look, B. Jogai, C. W. Litton, G. Cantwell, and W. C. Harsch, "Valence-band ordering in ZnO," *Phys. Rev. B*, vol. 60, no. 4, pp. 2340–2344, 1999.
- [4] K. Jacobi, G. Zwicker, and A. Gutmann, "Work function, electron affinity and band bending of zinc oxide surfaces," *Surf. Sci.*, vol. 141, no. 1, pp. 109–125, 1984.
- [5] J. J. Uhlrich, D. C. Olson, J. W. P. Hsu, and T. F. Kuech, "Surface chemistry and surface electronic properties of ZnO single crystals and nanorods," *J. Vac. Sci. Technol. A Vacuum, Surfaces, Film.*, vol. 27, no. 2, pp. 328–335, 2009.
- [6] A. J. Logsdail, D. O. Scanlon, C. R. A. Catlow, and A. A. Sokol, "Bulk ionization potentials and band alignments from three-dimensional periodic calculations as demonstrated on rocksalt oxides," *Phys. Rev. B*, vol. 90, no. 15, pp. 155106 1–8, 2014.
- [7] J. Jaffe, J. Snyder, Z. Lin, and A. Hess, "LDA and GGA calculations for

- high-pressure phase transitions in ZnO and MgO,” *Phys. Rev. B*, vol. 62, no. 3, pp. 1660–1665, 2000.
- [8] F. Cleri and V. Rosato, “Tight-binding potentials for transition metals and alloys,” *Phys. Rev. B*, vol. 48, no. 1, pp. 22–33, 1993.
- [9] S. T. Bromley, S. A. French, A. A. Sokol, C. R. A. Catlow, and P. Sherwood, “Metal cluster support interactions in the Cu/ZnO system: A QM/MM study,” *J. Phys. Chem. B*, vol. 107, no. 29, pp. 7045–7057, 2003.
- [10] S. A. French, A. A. Sokol, S. T. Bromley, C. R. A. Catlow, S. C. Rogers, F. King, and P. Sherwood, “From CO₂ to methanol by hybrid QM/MM embedding,” *Angew. Chemie Int. Ed.*, vol. 40, no. 23, pp. 4437–4440, 2001.
- [11] S. French, A. Sokol, S. Bromley, C. Catlow, and P. Sherwood, “Identification and characterization of active sites and their catalytic processes—the Cu/ZnO methanol catalyst,” *Top. Catal.*, vol. 24, no. 1-4, pp. 161–172, 2003.
- [12] “<http://www.essentialchemicalindustry.org/chemicals/methanol.html>” Accessed 2014.
- [13] V. E. Henrich and P. A. Cox, *The surface science of metal oxides*. Cambridge University Press, 1996.
- [14] V. A. Coleman and C. Jagadish, “Basic properties and applications of ZnO,” in *Zinc Oxide Bulk, Thin Film. Nanostructures*, pp. 1–20, Elsevier, 2006.
- [15] D. C. Look and B. Claflin, “P-type doping and devices based on ZnO,” *Phys. status solidi*, vol. 241, no. 3, pp. 624–630, 2004.
- [16] Ü. Özgür, Y. I. Alivov, C. Liu, A. Teke, M. A. Reshchikov, S. Dogan, V. Avrutin, S.-J. Cho, and H. Morkoc, “A comprehensive review of ZnO materials and devices,” *J. Appl. Phys.*, vol. 98, no. 4, pp. 041301 1–103, 2005.

- [17] S. Pearton, "Recent progress in processing and properties of ZnO," *Prog. Mater. Sci.*, vol. 50, no. 3, pp. 293–340, 2005.
- [18] Y. Kashiwaba, T. Abe, S. Onodera, F. Masuoka, A. Nakagawa, H. Endo, and I. Niikura, "Comparison of non-polar ZnO films deposited on single crystal ZnO and sapphire substrates," *J. Cryst. Growth*, vol. 298, pp. 477–480, 2007.
- [19] S. Han, S. Hong, J. Lee, J. Lee, J. Song, Y. Nam, S. Chang, T. Minegishi, and T. Yao, "Structural and optical properties of non-polar A-plane ZnO films grown on R-plane sapphire substrates by plasma-assisted molecular-beam epitaxy," *J. Cryst. Growth*, vol. 309, no. 2, pp. 121–127, 2007.
- [20] J.-H. Kim, S. Kyu Han, S.-K. Hong, J. Wook Lee, J. Yong Lee, J.-H. Song, S. Ig Hong, and T. Yao, "Growth of epitaxial ZnO films on Si (111) substrates with Cr compound buffer layer by plasma-assisted molecular beam epitaxy," *J. Cryst. Growth*, vol. 312, no. 15, pp. 2190–2195, 2010.
- [21] A. Ishii, Y. Oda, and K. Fujiwara, "DFT study for the anisotropic epitaxial growth of a-face ZnO(11 $\bar{2}$ 0)," *Phys. status solidi*, vol. 5, no. 9, pp. 2726–2728, 2008.
- [22] C. R. A. Catlow, S. A. French, A. A. Sokol, A. A. Al-Sunaidi, and S. M. Woodley, "Zinc oxide: A case study in contemporary computational solid state chemistry.," *J. Comput. Chem.*, vol. 29, no. 13, pp. 2234–49, 2008.
- [23] J. Albertsson, S. C. Abrahams, and Á. Kvik, "Atomic displacement, anharmonic thermal vibration, expansivity and pyroelectric coefficient thermal dependences in ZnO," *Acta Crystallogr. Sect. B Struct. Sci.*, vol. 45, no. 1, pp. 34–40, 1989.
- [24] F. Jensen, *Introduction to computational chemistry*. John Wiley & Sons, second ed., 2007.
- [25] C. R. A. Catlow, "Point defect and electronic properties of uranium dioxide," *Proc. R. Soc. A Math. Phys. Eng. Sci.*, vol. 353, no. 1675, pp. 533–561, 1977.

- [26] G. V. Lewis and C. R. A. Catlow, "Potential models for ionic oxides," *J. Phys. C Solid State Phys.*, vol. 18, no. 6, p. 1149, 1985.
- [27] S. M. Woodley, P. D. Battle, C. R. A. Catlow, and J. D. Gale, "Development of a new interatomic potential for the modeling of ligand field effects," *J. Phys. Chem. B*, vol. 105, no. 29, pp. 6824–6830, 2001.
- [28] E. Flikkema and S. Bromley, "A new interatomic potential for nanoscale silica," *Chem. Phys. Lett.*, vol. 378, no. 5-6, pp. 622–629, 2003.
- [29] A. Walsh, S. M. Woodley, C. R. A. Catlow, and A. A. Sokol, "Potential energy landscapes for anion Frenkel-pair formation in ceria and india," *Solid State Ionics*, vol. 184, no. 1, pp. 52–56, 2011.
- [30] J. D. Gale, "GULP: A computer program for the symmetry-adapted simulation of solids," *J. Chem. Soc., Faraday Trans.*, vol. 93, no. 4, pp. 629–637, 1997.
- [31] J. D. Gale and A. L. Rohl, "The General Utility Lattice Program (GULP)," *Mol. Simul.*, vol. 29, no. 5, pp. 291–341, 2003.
- [32] P. P. Ewald, "Die Berechnung optischer und elektrostatischer Gitterpotentiale," *Ann. Phys.*, vol. 369, no. 3, pp. 253–287, 1921.
- [33] J. E. Jones, "On the determination of molecular fields. II. From the equation of state of a gas," in *Proc. R. Soc. London A Math. Phys. Eng. Sci.*, vol. 106, pp. 463–477, The Royal Society, 1924.
- [34] R. A. Buckingham, "The classical equation of state of gaseous helium, neon and argon," *Proc. R. Soc. A Math. Phys. Eng. Sci.*, vol. 168, no. 933, pp. 264–283, 1938.
- [35] B. G. Dick Jr and A. W. Overhauser, "Theory of the dielectric constants of alkali halide crystals," *Phys. Rev.*, vol. 112, no. 1, p. 90, 1958.

- [36] P. W. Atkins and R. S. Friedman, *Molecular quantum mechanics*. Oxford university press, 2011.
- [37] I. N. Levine and P. H. I. Learning, *Quantum chemistry*, vol. 6. Pearson Prentice Hall Upper Saddle River, NJ, 2009.
- [38] W. Kohn and L. J. Sham, “Self-consistent equations including exchange and correlation effects,” *Phys. Rev.*, vol. 140, no. 4A, pp. A1133—A1138, 1965.
- [39] J. Perdew, K. Burke, and M. Ernzerhof, “Generalized gradient approximation made simple,” *Phys. Rev. Lett.*, vol. 77, no. 18, pp. 3865–3868, 1996.
- [40] J. Perdew, A. Ruzsinszky, G. Csonka, O. Vydrov, G. Scuseria, L. Constantin, X. Zhou, and K. Burke, “Restoring the density-gradient expansion for exchange in solids and surfaces,” *Phys. Rev. Lett.*, vol. 100, no. 13, pp. 136406 1–4, 2008.
- [41] J. Hubbard, “Electron correlations in narrow energy bands,” *Proc. R. Soc. A Math. Phys. Eng. Sci.*, vol. 276, no. 1365, pp. 238–257, 1963.
- [42] H. J. Monkhorst and J. D. Pack, “Special points for Brillouin-zone integrations,” *Phys. Rev. B*, vol. 13, no. 12, pp. 5188–5192, 1976.
- [43] G. Bachelet, D. Hamann, and M. Schlüter, “Pseudopotentials that work: From H to Pu,” *Phys. Rev. B*, vol. 26, no. 8, pp. 4199–4228, 1982.
- [44] D. Vanderbilt, “Soft self-consistent pseudopotentials in a generalized eigenvalue formalism,” *Phys. Rev. B*, vol. 41, no. 11, pp. 7892–7895, 1990.
- [45] P. E. Blöchl, “Projector augmented-wave method,” *Phys. Rev. B*, vol. 50, no. 24, pp. 17953–17979, 1994.
- [46] P. W. Tasker, “The stability of ionic crystal surfaces,” *J. Phys. C Solid State Phys.*, vol. 12, no. 22, p. 4977, 1979.

- [47] G. Kresse and J. Hafner, "Ab initio molecular-dynamics simulation of the liquid-metal-amorphous-semiconductor transition in germanium," *Phys. Rev. B*, vol. 49, no. 20, pp. 14251–14269, 1994.
- [48] G. Kresse and J. Furthmüller, "Efficiency of ab-initio total energy calculations for metals and semiconductors using a plane-wave basis set," *Comput. Mater. Sci.*, vol. 6, no. 1, pp. 15–50, 1996.
- [49] G. Kresse, "From ultrasoft pseudopotentials to the projector augmented-wave method," *Phys. Rev. B*, vol. 59, no. 3, pp. 1758–1775, 1999.
- [50] S. M. Woodley, "Knowledge Led Master Code search for atomic and electronic structures of LaF₃ nanoclusters on hybrid rigid ion-shell model-DFT landscapes," *J. Phys. Chem. C*, vol. 117, no. 45, pp. 24003–24014, 2013.
- [51] M. R. Farrow, Y. Chow, and S. M. Woodley, "Structure prediction of nanoclusters; a direct or a pre-screened search on the DFT energy landscape?," *Phys. Chem. Chem. Phys.*, vol. 16, no. 39, pp. 21119–21134, 2014.
- [52] "<http://www.archer.ac.uk/about-archer/>" Accessed 02/2016.
- [53] "<https://wiki.rc.ucl.ac.uk/wiki/Legion>" Accessed 02/2016.
- [54] "<http://www.southampton.ac.uk/isolutions/computing/hpc/iridis/>" Accessed 02/2016.
- [55] L. Whitmore, A. A. Sokol, and C. R. A. Catlow, "Surface structure of zinc oxide (10 $\bar{1}$ 0), using an atomistic, semi-infinite treatment," *Surf. Sci.*, vol. 498, no. 1-2, pp. 135–146, 2002.
- [56] D. R. Lide, *Handbook of chemistry and physics*. 89 ed., 2008.
- [57] O. Dulub, L. A. Boatner, and U. Diebold, "STM study of the geometric and electronic structure of ZnO(0001)-Zn, (000 $\bar{1}$)-O, (10 $\bar{1}$ 0), and (11 $\bar{2}$ 0) surfaces," *Surf. Sci.*, vol. 519, no. 3, pp. 201–217, 2002.

- [58] N. Jedrecy, S. Gallini, M. Sauvage-Simkin, and R. Pinchaux, "The ZnO non-polar (10 $\bar{1}$ 0) surface: an X-ray structural investigation," *Surf. Sci.*, vol. 460, no. 1-3, pp. 136–143, 2000.
- [59] K. Haga, T. Chiba, H. Onodera, T. Kadota, and C. Hasegawa, "Epitaxial growth of ZnO films prepared by using MO-CVD with Zn(C₉H₁₅O₃)₂," *J. Korean Phys. Soc.*, vol. 53, no. 1, pp. 55–58, 2008.
- [60] S. K. Han, S.-K. Hong, J. W. Lee, J. G. Kim, M. Jeong, J. Y. Lee, S. I. Hong, J. S. Park, Y. E. Ihm, J.-S. Ha, and T. Yao, "Properties of (11 $\bar{2}$ 0) a-plane ZnO films on sapphire substrates grown at different temperatures by plasma-assisted molecular beam epitaxy," *Thin Solid Films*, vol. 519, no. 19, pp. 6394–6398, 2011.
- [61] Y. Chen, D. M. Bagnall, H.-j. Koh, K.-t. Park, K. Hiraga, Z. Zhu, and T. Yao, "Plasma assisted molecular beam epitaxy of ZnO on c-plane sapphire: Growth and characterization," *J. Appl. Phys.*, vol. 84, no. 7, pp. 3912–3918, 1998.
- [62] J. Chen, H. Deng, N. Li, Y. Tian, and H. Ji, "Realization of nonpolar a-plane ZnO films on r-plane sapphire substrates using a simple single-source chemical vapor deposition," *Mater. Lett.*, vol. 65, no. 4, pp. 716–718, 2011.
- [63] K.-P. Liu, K.-Y. Yen, P.-Y. Lin, J.-R. Gong, K.-D. Wu, and W.-L. Chen, "Structural characteristics of ZnO films grown on (0001) or (11 $\bar{2}$ 0) sapphire substrates by atomic layer deposition," *J. Vac. Sci. Technol. A Vacuum, Surfaces, Film.*, vol. 29, no. 3, pp. 03A101 1–5, 2011.
- [64] M. Miyauchi, A. Shimai, and Y. Tsuru, "Photoinduced hydrophilicity of heteroepitaxially grown ZnO thin films," *J. Phys. Chem. B*, vol. 109, no. 27, pp. 13307–11, 2005.
- [65] S. K. Han, J. G. Kim, J.-H. Kim, S.-K. Hong, J. W. Lee, J. Y. Lee, J.-H. Song, Y. S. Nam, S.-K. Chang, and T. Yao, "Effects of two-step growth by

- employing Zn-rich and O-rich growth conditions on properties of (11 $\bar{2}$ 0) ZnO films grown by plasma-assisted molecular beam epitaxy on sapphire,” *J. Vac. Sci. Technol. B Microelectron. Nanom. Struct.*, vol. 27, no. 3, pp. 1635–1640, 2009.
- [66] C. Jia, Y. Chen, X. Liu, S. Yang, W. Zhang, and Z. Wang, “Control of epitaxial relationships of ZnO/SrTiO₃ heterointerfaces by etching the substrate surface,” *Nanoscale Res. Lett.*, vol. 8, no. 1, pp. 23 1–8, 2013.
- [67] A. Beltrán, J. Andrés, M. Calatayud, and J. Martins, “Theoretical study of ZnO (10 $\bar{1}$ 0) and Cu/ZnO (10 $\bar{1}$ 0) surfaces,” *Chem. Phys. Lett.*, vol. 338, no. 4–6, pp. 224–230, 2001.
- [68] D. J. Cooke, A. Marmier, and S. C. Parker, “Surface structure of (10 $\bar{1}$ 0) and (11 $\bar{2}$ 0) surfaces of ZnO with density functional theory and atomistic simulation,” *J. Phys. Chem. B*, vol. 110, no. 15, pp. 7985–7991, 2006.
- [69] A. Filippetti, V. Fiorentini, G. Cappellini, and A. Bosin, “Anomalous relaxations and chemical trends at III-V semiconductor nitride nonpolar surfaces,” *Phys. Rev. B*, vol. 59, no. 12, pp. 8026–8031, 1999.
- [70] J. E. Jaffe, N. M. Harrison, and A. C. Hess, “Ab initio study of ZnO (10 $\bar{1}$ 0) surface relaxation,” *Phys. Rev. B*, vol. 49, no. 16, pp. 11153–11158, 1994.
- [71] N. L. Marana, V. M. Longo, E. Longo, J. B. L. Martins, and J. R. Sambrano, “Electronic and structural properties of the (10 $\bar{1}$ 0) and (11 $\bar{2}$ 0) ZnO surfaces,” *J. Phys. Chem. A*, vol. 112, no. 38, pp. 8958–8963, 2008.
- [72] B. Meyer and D. Marx, “Density-functional study of the structure and stability of ZnO surfaces,” *Phys. Rev. B*, vol. 67, no. 3, pp. 035403 1–11, 2003.
- [73] A. Wander and N. Harrison, “An ab initio study of ZnO(10 $\bar{1}$ 0),” *Surf. Sci.*, vol. 457, no. 1-2, pp. L342–L346, 2000.
- [74] Y. Wang and C. Duke, “Surface reconstructions of ZnO cleavage faces,” *Surf. Sci.*, vol. 192, no. 2-3, pp. 309–322, 1987.

- [75] M. J. Spencer, K. W. Wong, and I. Yarovsky, "Density functional theory modelling of ZnO(10 $\bar{1}$ 0) and ZnO(2 $\bar{1}$ $\bar{1}$ 0) surfaces: Structure, properties and adsorption of N₂O," 2010.
- [76] W. Göpel, J. Pollmann, I. Ivanov, and B. Reihl, "Angle-resolved photoemission from polar and nonpolar zinc oxide surfaces," *Phys. Rev. B*, vol. 26, no. 6, pp. 3144–3150, 1982.
- [77] C. B. Duke, R. J. Meyer, A. Paton, and P. Mark, "Calculation of low-energy-electron-diffraction intensities from ZnO (10 $\bar{1}$ 0). II. Influence of calculational procedure, model potential, and second-layer structural distortions," *Phys. Rev. B*, vol. 18, no. 8, pp. 4225–4240, 1978.
- [78] Y. Ding and Z. L. Wang, "Profile imaging of reconstructed polar and non-polar surfaces of ZnO," *Surf. Sci.*, vol. 601, no. 2, pp. 425–433, 2007.
- [79] I. Ivanov and J. Pollmann, "Effects of surface relaxation on the electronic structure of ZnO (10 $\bar{1}$ 0)," *J. Vac. Sci. Technol.*, vol. 19, no. 3, pp. 344–346, 1981.
- [80] M. Nyberg, M. A. Nygren, L. G. M. Pettersson, D. H. Gay, and A. L. Rohl, "Hydrogen dissociation on reconstructed ZnO surfaces," *J. Phys. Chem.*, vol. 100, no. 21, pp. 9054–9063, 1996.
- [81] P. Schröer, P. Krüger, and J. Pollmann, "Self-consistent electronic-structure calculations of the (10 $\bar{1}$ 0) surfaces of the wurtzite compounds ZnO and CdS," *Phys. Rev. B*, vol. 49, no. 24, pp. 17092–17101, 1994.
- [82] T. Parker, N. Condon, R. Lindsay, F. Leibsle, and G. Thornton, "Imaging the polar (000 $\bar{1}$) and non-polar (10 $\bar{1}$ 0) surfaces of ZnO with STM," *Surf. Sci.*, vol. 415, no. 3, pp. L1046–L1050, 1998.
- [83] M. Chung and H. Farnsworth, "Investigations of surface stability of II-VI wurtzite compounds by LEED," *Surf. Sci.*, vol. 22, no. 1, pp. 93–110, 1970.

- [84] A. Wander and N. M. Harrison, "An ab-initio study of ZnO(11 $\bar{2}$ 0)," *Surf. Sci.*, vol. 468, no. 13, pp. L851–L855, 2000.
- [85] I. Ivanov and J. Pollmann, "Electronic structure of ideal and relaxed surfaces of ZnO: A prototype ionic wurtzite semiconductor and its surface properties," *Phys. Rev. B*, vol. 24, no. 12, pp. 7275–7296, 1981.
- [86] D. Mora-Fonz, J. Buckeridge, A. J. Logsdail, D. O. Scanlon, A. A. Sokol, S. Woodley, and C. R. A. Catlow, "Morphological features and band bending at non-polar surfaces of ZnO," *J. Phys. Chem. C*, vol. 119, no. 21, pp. 11598–11611, 2015.
- [87] D. J. Binks and R. W. Grimes, "Incorporation of monovalent ions in ZnO and their influence on varistor degradation," *J. Am. Ceram. Soc.*, vol. 76, no. 9, pp. 2370–2372, 1993.
- [88] A. Klein, C. Körber, A. Wachau, F. Säuberlich, Y. Gassenbauer, S. P. Harvey, D. E. Proffit, and T. O. Mason, "Transparent conducting oxides for photovoltaics: manipulation of Fermi level, work function and energy band alignment," *Materials (Basel)*, vol. 3, no. 11, pp. 4892–4914, 2010.
- [89] C. G. Granqvist, "Transparent conductors as solar energy materials: A panoramic review," *Sol. Energy Mater. Sol. Cells*, vol. 91, no. 17, pp. 1529–1598, 2007.
- [90] D. S. Ginley and C. Bright, "Transparent conducting oxides," *MRS Bull.*, vol. 25, no. 08, pp. 15–18, 2011.
- [91] B. G. Lewis and D. C. Paine, "Applications and processing of transparent conducting oxides," *MRS Bull.*, vol. 25, no. 08, pp. 22–27, 2011.
- [92] A. A. Sokol, S. A. French, S. T. Bromley, C. R. A. Catlow, H. J. J. van Dam, and P. Sherwood, "Point defects in ZnO," *Faraday Discuss.*, vol. 134, pp. 267–282, 2007.

- [93] Y. Hinuma, A. Grüneis, G. Kresse, and F. Oba, “Band alignment of semiconductors from density-functional theory and many-body perturbation theory,” *Phys. Rev. B*, vol. 90, no. 15, pp. 155405 1–16, 2014.
- [94] A. Walsh and K. T. Butler, “Prediction of electron energies in metal oxides,” *Acc. Chem. Res.*, vol. 47, no. 2, pp. 364–72, 2014.
- [95] V. Stevanović, S. Lany, D. S. Ginley, W. Tumas, and A. Zunger, “Assessing capability of semiconductors to split water using ionization potentials and electron affinities only,” *Phys. Chem. Chem. Phys.*, vol. 16, no. 8, pp. 3706–3714, 2014.
- [96] J. Klimeš, M. Kaltak, and G. Kresse, “Predictive GW calculations using plane waves and pseudopotentials,” *Phys. Rev. B*, vol. 90, no. 7, pp. 075125 1–15, 2014.
- [97] P. D. C. King, T. D. Veal, C. F. McConville, J. Zúñiga-Pérez, V. Muñoz-Sanjosé, M. Hopkinson, E. D. L. Rienks, M. F. Jensen, and P. Hofmann, “Surface band-gap narrowing in quantized electron accumulation layers,” *Phys. Rev. Lett.*, vol. 104, no. 25, pp. 256803 1–4, 2010.
- [98] J. Xiao, X. Zhang, and G. Zhang, “Field emission from zinc oxide nanotowers: the role of the top morphology,” *Nanotechnology*, vol. 19, no. 29, pp. 295706 1–6, 2008.
- [99] W. Wang, G. Zhang, L. Yu, X. Bai, Z. Zhang, and X. Zhao, “Field emission properties of zinc oxide nanowires fabricated by thermal evaporation,” *Phys. E Low-dimensional Syst. Nanostructures*, vol. 36, no. 1, pp. 86–91, 2007.
- [100] H. Moormann, D. Kohl, and G. Heiland, “Work function and band bending on clean cleaved zinc oxide surfaces,” *Surf. Sci.*, vol. 80, pp. 261–264, 1979.
- [101] H. Moormann, D. Kohl, and G. Heiland, “Variations of work function and surface conductivity on clean cleaved zinc oxide surfaces by annealing and by hydrogen adsorption,” *Surf. Sci.*, vol. 100, no. 2, pp. 302–314, 1980.

- [102] H. Li, P. Winget, and J.-L. Brédas, “Transparent Conducting oxides of relevance to organic electronics: Electronic structures of their interfaces with organic layers,” *Chem. Mater.*, vol. 26, no. 1, pp. 631–646, 2014.
- [103] W. Göpel, “Surface point defects and Schottky barrier formation on ZnO(10 $\bar{1}$ 0),” *J. Vac. Sci. Technol.*, vol. 17, no. 5, pp. 894–898, 1980.
- [104] S. V. Didziulis, K. D. Butcher, S. L. Cohen, and E. I. Solomon, “Chemistry of copper overlayers on zinc oxide single-crystal surfaces: model active sites for copper/zinc oxide methanol synthesis catalysts,” *J. Am. Chem. Soc.*, vol. 111, no. 18, pp. 7110–7123, 1989.
- [105] F.-L. Kuo, Y. Li, M. Solomon, J. Du, and N. D. Shepherd, “Workfunction tuning of zinc oxide films by argon sputtering and oxygen plasma: an experimental and computational study,” *J. Phys. D. Appl. Phys.*, vol. 45, no. 6, pp. 065301 1–7, 2012.
- [106] A. Gutmann, G. Zwicker, D. Schmeisser, and K. Jacobi, “Interaction of xenon with zinc oxide surfaces,” *Surf. Sci.*, vol. 137, no. 1, pp. 211–241, 1984.
- [107] J. Vohs and M. Barteau, “Conversion of methanol, formaldehyde and formic acid on the polar faces of zinc oxide,” *Surf. Sci.*, vol. 176, no. 1-2, pp. 91–114, 1986.
- [108] K. Sun, H.-Y. Su, and W.-X. Li, “Stability of polar ZnO surfaces studied by pair potential method and local energy density method,” *Theor. Chem. Acc.*, vol. 133, no. 1, p. 1427, 2013.
- [109] A. R. Lubinsky, “Atomic geometry of the low-index surfaces of ZnO: LEED analysis,” *J. Vac. Sci. Technol.*, vol. 13, no. 1, p. 189, 1976.
- [110] C. Duke and A. Lubinsky, “Calculations of low-energy electron diffraction intensities from the polar faces of ZnO,” *Surf. Sci.*, vol. 50, no. 2, pp. 605–614, 1975.

- [111] S.-C. Chang and P. Mark, "The crystallography of the polar (0001) Zn and (000 $\bar{1}$) O surfaces of zinc oxide," *Surf. Sci.*, vol. 46, no. 1, pp. 293–300, 1974.
- [112] T. Becker, S. Hövel, M. Kunat, C. Boas, U. Burghaus, and C. Wöll, "Interaction of hydrogen with metal oxides: the case of the polar ZnO(0001) surface," *Surf. Sci.*, vol. 486, no. 3, pp. L502–L506, 2001.
- [113] R. Nosker, P. Mark, and J. Levine, "Polar surfaces of wurtzite and zincblende lattices," *Surf. Sci.*, vol. 19, no. 2, pp. 291–317, 1970.
- [114] N. Jedrecy, S. Gallini, M. Sauvage-Simkin, and R. Pinchaux, "Copper growth on the O-terminated ZnO(000 $\bar{1}$) surface: Structure and morphology," *Phys. Rev. B*, vol. 64, no. 8, p. 85424, 2001.
- [115] H. van Hove and R. Leysen, "LEED study on the polar surfaces of ZnO," *Phys. Status Solidi*, vol. 9, no. 1, pp. 361–367, 1972.
- [116] S. Overbury, P. Radulovic, S. Thevuthasan, G. Herman, M. Henderson, and C. Peden, "Ion scattering study of the Zn and oxygen-terminated basal plane surfaces of ZnO," *Surf. Sci.*, vol. 410, no. 1, pp. 106–122, 1998.
- [117] A. Wander, F. Schedin, P. Steadman, A. Norris, R. McGrath, T. Turner, G. Thornton, and N. Harrison, "Stability of polar oxide surfaces," *Phys. Rev. Lett.*, vol. 86, no. 17, pp. 3811–3814, 2001.
- [118] C. Wöll, "The chemistry and physics of zinc oxide surfaces," *Prog. Surf. Sci.*, vol. 82, no. 2-3, pp. 55–120, 2007.
- [119] M. Kunat, S. G. Girol, U. Burghaus, and C. Wöll, "The interaction of water with the oxygen-terminated, polar surface of ZnO," *J. Phys. Chem. B*, vol. 107, no. 51, pp. 14350–14356, 2003.
- [120] J. V. Lauritsen, S. Porsgaard, M. K. Rasmussen, M. C. R. Jensen, R. Bechstein, K. Meinander, B. S. Clausen, S. Helveg, R. Wahl, G. Kresse, and F. Besenbacher, "Stabilization principles for polar surfaces of ZnO.," *ACS Nano*, vol. 5, no. 7, pp. 5987–94, 2011.

- [121] C. Noguera, "Polar oxide surfaces," *J. Phys. Condens. Matter*, vol. 12, no. 31, pp. R367–R410, 2000.
- [122] G. Kresse, O. Dulub, and U. Diebold, "Competing stabilization mechanism for the polar ZnO(0001)-Zn surface," *Phys. Rev. B*, vol. 68, no. 24, p. 245409, 2003.
- [123] O. Dulub, U. Diebold, and G. Kresse, "Novel stabilization mechanism on polar surfaces: ZnO(0001)-Zn," *Phys. Rev. Lett.*, vol. 90, no. 1, p. 16102, 2003.
- [124] R. Wahl, J. V. Lauritsen, F. Besenbacher, and G. Kresse, "Stabilization mechanism for the polar ZnO(000 $\bar{1}$)-O surface," *Phys. Rev. B*, vol. 87, no. 8, p. 085313, 2013.
- [125] H. Zheng, J. Kröger, and R. Berndt, "Spectroscopy of single donors at ZnO(0001) surfaces," *Phys. Rev. Lett.*, vol. 108, no. 7, p. 76801, 2012.
- [126] H. Meskine and P. A. Mulheran, "Simulation of reconstructions of the polar ZnO(0001) surfaces," *Phys. Rev. B*, vol. 84, no. 16, p. 165430, 2011.
- [127] A. Calzolari, M. Bazzani, and A. Catellani, "Dipolar and charge transfer effects on the atomic stabilization of ZnO polar surfaces," *Surf. Sci.*, vol. 607, no. 0, pp. 181–186, 2013.
- [128] R. Girard, O. Tjernberg, G. Chiaia, S. Söderholm, U. Karlsson, C. Wigren, H. Nylén, and I. Lindau, "Electronic structure of ZnO(0001) studied by angle-resolved photoelectron spectroscopy," *Surf. Sci.*, vol. 373, no. 2-3, pp. 409–417, 1997.
- [129] A. Wander and N. M. Harrison, "The stability of polar oxide surfaces: The interaction of H₂O with ZnO(0001) and ZnO(000 $\bar{1}$)," *J. Chem. Phys.*, vol. 115, no. 5, p. 2312, 2001.

- [130] N. Jedrecy, M. Sauvage-Simkin, and R. Pinchaux, "The hexagonal polar ZnO(0001)-(1 × 1) surfaces: structural features as stemming from X-ray diffraction," *Appl. Surf. Sci.*, vol. 162-163, pp. 69–73, 2000.
- [131] H. Zheng, M. Gruyters, E. Pehlke, and R. Berndt, "'Magic' vicinal zinc oxide surfaces," *Phys. Rev. Lett.*, vol. 111, no. 8, p. 86101, 2013.
- [132] P. Chul-Hong, "First-principles study of the surface energy and atom cohesion of wurtzite ZnO and ZnS - Implications for nanostructure formation," *J. Korean Phys. Soc.*, vol. 56, no. 12, p. 498, 2010.
- [133] M. S. Spencer, "The role of zinc oxide in Cu/ZnO catalysts for methanol synthesis and the water–gas shift reaction," *Top. Catal.*, vol. 8, no. 3-4, pp. 259–266, 1999.
- [134] J. P. Breen and J. R. Ross, "Methanol reforming for fuel-cell applications: Development of zirconia-containing Cu-Zn-Al catalysts," *Catal. Today*, vol. 51, no. 3-4, pp. 521–533, 1999.
- [135] K. C. Waugh, "Methanol synthesis," *Catal. Today*, vol. 15, no. 1, pp. 51–75, 1992.
- [136] D. Scarano, G. Spoto, S. Bordiga, A. Zecchina, and C. Lamberti, "Lateral interactions in CO adlayers on prismatic ZnO faces: a FTIR and HRTEM study," *Surf. Sci.*, vol. 276, no. 1-3, pp. 281–298, 1992.
- [137] S. Darby, T. V. Mortimer-Jones, R. L. Johnston, and C. Roberts, "Theoretical study of Cu-Au nanoalloy clusters using a genetic algorithm," *J. Chem. Phys.*, vol. 116, no. 4, p. 1536, 2002.
- [138] G. G. Rusina, S. D. Borisova, and E. V. Chulkov, "Structure and analysis of atomic vibrations in clusters of Cu_n ($n \leq 20$)," *Russ. J. Phys. Chem. A*, vol. 87, no. 2, pp. 233–239, 2013.
- [139] Y. Y. Gafner, S. L. Gafner, I. S. Zamulin, L. V. Redel, and V. S. Baidyshev, "Analysis of the heat capacity of nanoclusters of FCC metals on the example

- of Al, Ni, Cu, Pd, and Au,” *Phys. Met. Metallogr.*, vol. 116, no. 6, pp. 568–575, 2015.
- [140] I. V. Chepkasov and L. V. Redel, “Calculations of the heat capacity of Cu clusters synthesized by condensation from the gas phase,” *IOP Conf. Ser. Mater. Sci. Eng.*, vol. 81, no. 1, p. 012014, 2015.
- [141] N. T. Wilson, *Ph. D. thesis*. PhD thesis, University of Birmingham, 2000.
- [142] G. D’Agostino, “Copper clusters simulated by a many-body tight-binding potential,” *Philos. Mag. Part B*, vol. 68, no. 6, pp. 903–911, 1993.
- [143] a. Erkoç and R. Shaltaf, “Monte Carlo computer simulation of copper clusters,” *Phys. Rev. A*, vol. 60, no. 4, pp. 3053–3057, 1999.
- [144] O. Dulub, L. A. Boatner, and U. Diebold, “STM study of Cu growth on the ZnO(10 $\bar{1}$ 0) surface,” *Surf. Sci.*, vol. 504, pp. 271–281, 2002.
- [145] K. Ozawa, T. Sato, Y. Oba, and K. Edamoto, “Electronic structure of Cu on ZnO(1010): Angle-resolved photoemission spectroscopy study,” *J. Phys. Chem. C*, vol. 111, no. 11, pp. 4256–4263, 2007.
- [146] I. Demiroglu, S. M. Woodley, A. A. Sokol, and S. T. Bromley, “From monomer to monolayer: a global optimisation study of (ZnO)_n nanoclusters on the Ag surface.,” *Nanoscale*, vol. 6, no. 24, pp. 14754–65, 2014.
- [147] A. A. Al-Sunaidi, A. A. Sokol, C. R. A. Catlow, and S. M. Woodley, “Structures of zinc oxide nanoclusters: As found by revolutionary algorithm techniques,” *J. Phys. Chem. C*, vol. 112, no. 48, pp. 18860–18875, 2008.
- [148] O. Dulub, M. Batzill, and U. Diebold, “Growth of copper on single crystalline ZnO: Surface study of a model catalyst,” *Top. Catal.*, vol. 36, no. 1-4, pp. 65–76, 2005.
- [149] S. A. French, A. A. Sokol, C. R. A. Catlow, and P. Sherwood, “The growth of copper clusters over ZnO: The competition between planar and polyhedral clusters,” *J. Phys. Chem. C*, vol. 112, no. 19, pp. 7420–7430, 2008.

- [150] C. R. A. Catlow, S. A. French, A. A. Sokol, M. Alfredsson, and S. T. Bromley, "Understanding the interface between oxides and metals," *Faraday Discuss.*, vol. 124, p. 185, 2003.
- [151] "<http://mcgroup.co.uk/news/20140627/formaldehyde-production-exceed-52-mln-tonnes.html>" Accessed 02/2016.
- [152] M. House, A. Carley, and M. Bowker, "Selective oxidation of methanol on iron molybdate catalysts and the effects of surface reduction," *J. Catal.*, vol. 252, no. 1, pp. 88–96, 2007.
- [153] E. Söderhjelm, M. P. House, N. Cruise, J. Holmberg, M. Bowker, J.-O. Bovin, and A. Andersson, "On the synergy effect in $\text{MoO}_3\text{-Fe}_2(\text{MoO}_4)_3$ catalysts for methanol oxidation to formaldehyde," *Top. Catal.*, vol. 50, no. 1-4, pp. 145–155, 2008.
- [154] C. Brookes, P. P. Wells, N. Dimitratos, W. Jones, E. K. Gibson, D. J. Morgan, G. Cibir, C. Nicklin, D. Mora-Fonz, D. O. Scanlon, C. R. A. Catlow, and M. Bowker, "The nature of the molybdenum surface in iron molybdate. The active phase in selective methanol oxidation," *J. Phys. Chem. C*, vol. 118, no. 45, pp. 26155–26161, 2014.
- [155] K. I. Ivanov and D. Y. Dimitrov, "Deactivation of an industrial iron-molybdate catalyst for methanol oxidation," *Catal. Today*, vol. 154, no. 3-4, pp. 250–255, 2010.
- [156] A. Andersson, M. Hernelind, and O. Augustsson, "A study of the ageing and deactivation phenomena occurring during operation of an iron molybdate catalyst in formaldehyde production," *Catal. Today*, vol. 112, no. 1-4, pp. 40–44, 2006.
- [157] J. Chen, L. Xu, W. Li, and X. Gou, " $\alpha\text{-Fe}_2\text{O}_3$ Nanotubes in gas sensor and lithium-ion battery applications," *Adv. Mater.*, vol. 17, no. 5, pp. 582–586, 2005.

- [158] S. L. Dudarev, G. A. Botton, S. Y. Savrasov, C. J. Humphreys, and A. P. Sutton, “Electron-energy-loss spectra and the structural stability of nickel oxide: An LSDA+ U study,” *Phys. Rev. B*, vol. 57, no. 3, pp. 1505–1509, 1998.
- [159] G. Rollmann, A. Rohrbach, P. Entel, and J. Hafner, “First-principles calculation of the structure and magnetic phases of hematite,” *Phys. Rev. B*, vol. 69, no. 16, p. 165107, 2004.
- [160] A. Rohrbach, J. Hafner, and G. Kresse, “Ab initio study of the (0001) surfaces of hematite and chromia: Influence of strong electronic correlations,” *Phys. Rev. B*, vol. 70, no. 12, p. 125426, 2004.
- [161] R. Coquet and D. J. Willock, “The (010) surface of α - MoO_3 , a DFT + U study,” *Phys. Chem. Chem. Phys.*, vol. 7, no. 22, pp. 3819–28, 2005.
- [162] L. M. Sandratskii, M. Uhl, and J. Kübler, “Band theory for electronic and magnetic properties of α - Fe_2O_3 ,” *J. Phys. Condens. Matter*, vol. 8, no. 8, pp. 983–989, 1996.
- [163] L. W. Finger and R. M. Hazen, “Crystal structure and isothermal compression of Fe_2O_3 , Cr_2O_3 , and V_2O_3 to 50 kbars,” *J. Appl. Phys.*, vol. 51, no. 10, p. 5362, 1980.
- [164] F. Alvarez-Ramírez, J. Martínez-Magadán, J. Gomes, and F. Illas, “On the geometric structure of the (0001) hematite surface,” *Surf. Sci.*, vol. 558, no. 1-3, pp. 4–14, 2004.
- [165] L. Pauling and S. B. Hendricks, “The crystal structures of hematite and corundum,” *J. Am. Chem. Soc.*, vol. 47, no. 3, pp. 781–790, 1925.
- [166] X.-G. Wang, W. Weiss, S. Shaikhutdinov, M. Ritter, M. Petersen, F. Wagner, R. Schlögl, and M. Scheffler, “The hematite (α - Fe_2O_3) (0001) surface: Evidence for domains of distinct chemistry,” *Phys. Rev. Lett.*, vol. 81, no. 5, pp. 1038–1041, 1998.

- [167] Y. Tang, H. Qin, K. Wu, Q. Guo, and J. Guo, "The reduction and oxidation of $\text{Fe}_2\text{O}_3(0001)$ surface investigated by scanning tunneling microscopy," *Surf. Sci.*, vol. 609, pp. 67–72, 2013.
- [168] S. A. Chambers and S. I. Yi, "Fe termination for $\alpha\text{-Fe}_2\text{O}_3(0001)$ as grown by oxygen-plasma-assisted molecular beam epitaxy," *Surf. Sci.*, vol. 439, no. 1–3, pp. L785–L791, 1999.
- [169] C. Dong, S. Sheng, W. Qin, Q. Lu, Y. Zhao, X. Wang, and J. Zhang, "Density functional theory study on activity of $\alpha\text{-Fe}_2\text{O}_3$ in chemical-looping combustion system," *Appl. Surf. Sci.*, vol. 257, no. 20, pp. 8647–8652, 2011.
- [170] A. Kiejna and T. Pabisiak, "Surface properties of clean and Au or Pd covered hematite ($\alpha\text{-Fe}_2\text{O}_3$) (0001)," *J. Phys. Condens. Matter*, vol. 24, no. 9, p. 095003, 2012.
- [171] S. M. Souvi, M. Badawi, J.-F. Paul, S. Cristol, and L. Cantrel, "A DFT study of the hematite surface state in the presence of H_2 , H_2O and O_2 ," *Surf. Sci.*, vol. 610, pp. 7–15, 2013.